# COLD SEASON INVERSION FOG IN SALT LAKE CITY:

# CONNECTIONS TO VALLEY VARIABLES

# AND NUMERICAL SIMULATIONS

by

Catherine N. Chachere

A thesis submitted to the faculty of
The University of Utah
in partial fulfillment of the requirements for the degree of

Master of Science

Department of Atmospheric Sciences

The University of Utah

December 2016

**The University of Utah Graduate School**

# STATEMENT OF THESIS APPROVAL

The thesis of **Catherine N. Chachere**

has been approved by the following supervisory committee members:

| | | |
|---|---|---|
| **Zhaoxia Pu** | , Chair | **05/16/16** Date Approved |
| **Sebastian Wilhelm Hoch** | , Member | **05/16/16** Date Approved |
| **Eric R. Pardyjak** | , Member | **05/16/16** Date Approved |

and by **Kevin D. Perry** , Chair/Dean of

the Department/College/School of **Atmospheric Sciences**

and by David B. Kieda, Dean of The Graduate School.

# ABSTRACT

A comprehensive study on cold season inversion fog at Salt Lake City, Utah, has been performed. First, the connection between stable valley airmasses and fog events was investigated using soundings and reported automated surface observing system (ASOS) data from Salt Lake International Airport (KSLC) for eighteen cold seasons (October to March, during 1997-2015). A chi-square test of independence was performed on identified stable valley airmasses and fog events to determine whether the two are correlated. Conditional probabilities were then computed to investigate the occurrence of fog, given the presence of a stable valley airmass. These probabilities are compared against that of random fog generation in mid-winter. It was concluded that the dependence between stable valley airmasses and fog events is statistically significant and that the presence of such airmasses makes the formation of fog more likely in mid-winter.

The Weather Research and Forecasting (WRF) model was then employed to simulate a wintertime inversion fog event in the Salt Lake Valley during IOP 2 of the Mountain Terrain Atmospheric Modeling and Observations Program (MATERHORN) Fog field campaign during January 2015. Simulation results were compared to observations obtained from the field program. Sensitivity to available cloud microphysical (CM), planetary boundary layer (PBL), radiation, and land surface schemes are examined. Results indicate that the numerical simulation of the fog events were not only sensitive to CM, PBL, radiation, and land surface schemes, but also to the lead time chosen before the

phenomenon is manifested. This study finds through the majority of experiments conducted that the synoptic setup in which fog forms can be accurately captured by numerical simulation. Errors found in most experiments occur in the boundary layer, specifically modeled temperatures are up to three degrees higher than the observed temperatures. Accurate representation of surface and boundary layer variables are vital in correctly predicting fog in a numerical model.

TABLE OF CONTENTS

# ACKNOWLEDGEMENTS

I would first like to thank my advisor, Dr. Zhaoxia Pu, for the opportunity to move across the country to study a subject for which I am impassioned. Her guidance and direction are greatly appreciated. I would also like to thank my committee members, Drs. Sebastian Hoch and Eric Pardyjak, for their valuable comments.

I am grateful for the family of scientists that is the Department of Atmospheric Sciences, especially my close friends Ali, Ansley, McKenna, Wyndam, and Prabhat. Their friendship, guidance, and willingness to listen was never taken for granted. To my family in Louisiana, thanks for encouraging me to pursue my dreams.

I am appreciative of the National Center for Atmospheric Research (NCAR) Weather Research and Forecasting (WRF) model development group, whose efforts made this model available to the atmospheric sciences community. Support from the Center for High Performance Computing (CHPC) at the University of Utah made the intensive computational work possible.

I would like to thank the University of Wyoming Weather Lab for archived sounding data, and the University of Utah MesoWest group for quality controlled Automated Surface Observing System (ASOS) data, and the MATERHORN-Fog team for observations collected during the field program.

This study is supported by the Office of Naval Research Award N00014-11-1-0709.

# CHAPTER 1

# INTRODUCTION AND BACKGROUND

## 1.1 Stable Valley Airmasses

Stable airmasses are typically found in areas of complex terrain as the mountain barriers prevent movement of near-surface air. The mountains can act to prevent the movement of very stable air from the valley in which it is confined. However, it can also act to keep a very cold, stable airmass from moving into a mountainous region. The stability of mountain valley airmasses is important to recognize as the meteorological conditions within these columns are conducive to persistent fog and poor air quality episodes (Wolyn and McKee 1989). In this study, we examine two phenomena in particular: deep stable layers and valley cold pools.

A deep stable layer is a deep layer of at least moderate stability that is deeper than typical nocturnal inversions (Wolyn and McKee 1989). The rigid mathematical definition for a deep stable layer in the intermountain United States is: 65% of the lowest 1.5 km of the 1200 UTC sounding (Mountain Standard Time or MST) has a lapse rate of 2.5 K/km or less. This was determined using a study of four cities with sounding release sites located in a mountain basin: Grand Junction, Salt Lake City, Winnemucca, and Boise. The study was the earliest to describe and define this event in the intermountain western United States. This definition will be used in Chapter 2 as the criteria for identifying deep stable

layers.

A valley cold pool is a layer of cold, stagnant air that is confined by a topographic boundary (Whiteman, et al. 2001). The airmass contained by the mountain valley can effectively be considered independent from its surroundings. A temperature inversion or elevated statically stable layer acts as the boundary between the cold pool and the free atmosphere. This boundary allows the atmospheric variables found in the valley to be decoupled from the upper air. Compared to above-mountain conditions, the valley has colder temperature, higher stability, and weaker winds independent of the mean flow aloft in both speed and direction.

Cold pools can be classified in two types: diurnal and persistent (Lareau et al. 2013). Diurnal cold pools form during the evening under clear air conditions. Emission of longwave radiation from the surface at night cools the surface and near-surface air. This cooling is sufficient to create a temperature inversion at the surface, the air within and under the inversion being the cold pool. Upon sunrise, the heating of the boundary layer near the ground and lowering of the upper boundary of the inversion creates a convective boundary layer and destroys the cold pool (Machalek 1974).

Persistent cold pool events occur in the winter when these turbulent processes are not sufficient to mix out the column. The creation of persistent cold pool events is complex and arise from a multitude of atmospheric processes. Synoptically, differential temperature advection and subsidence modulate cold air pool strength and duration, a result of persistent ridging across the intermountain states (Wolyn and McKee 1989). On the mesoscale, radiative, turbulent, and cloud processes affect their evolution (Lareau et al. 2013).

Climatological studies of persistent valley cold pools show that the events most commonly occur in the winter months (Wolyn and McKee 1989; Whiteman et al. 1999, 2001). The average duration of a persistent valley cold pool event is typical of the synoptic scale, one or two days, but they can persist for eight days or more (Wolyn and McKee 1989). The strength can vary, however, as noted in Wolyn and McKee (1989) and Whiteman (1999). These fluctuations can cause partial mix outs, or periods between cold air pool events (Holmes et al. 2015), of the valleys that contain the cold air pools.

In addition, Whiteman et al. (1999) compiled a thorough analysis of the large-scale environment for these events. Their paper states that the mechanisms that keep cold air pools in place, namely temperature inversions and elevated stable layers, are formed by warm air advection in tropospheric midlevels. This makes the air above the terrain barrier much warmer than the air within it. A setup like this is typically formed in environments downstream of synoptic-scale ridging and is usually broken up by a strong trough passage. Climatologically, these events are most common in the Northern Hemisphere winter months, as inversions and stable layers in warmer seasons are broken up daily by the growth of the daytime convective boundary layer (CBL). Solar radiation is the driving force of these breakup events as a fraction of the solar radiation received on the valley floor and sidewalls is converted to sensible heat flux and provides energy to the valley atmosphere (Whiteman 1982) and causes the CBL to form. This argument makes light of the fact that aspect, shadows, and snow cover are all important mechanisms in the effectiveness of CBL growth and cold air pool breakup.

Cold air pool events have also been closely tied to high concentrations of pollutants. An investigation of the connections between meteorological variables in these cold air pool

environments and particulate air pollution was conducted in the Salt Lake Valley by Whiteman et al. (2014). The aim of this study was to clarify the critical factors that control episodes of high particulate concentrations in the Salt Lake Valley and other similar basins and valleys which experience poor wintertime air quality. Through an in-depth analysis, a bulk measure of stability in the valley was created and called the valley heat deficit. It is the heat required to warm an atmospheric column with a 1 $m^2$ base to the potential temperature at height *h*, bringing the underlying atmosphere to a dry adiabatic lapse rate. For the Salt Lake Valley, this height is 2200 m MSL, the average height of the surrounding topography. The equation for this variable in the Salt Lake Valley is as follows:

$$H_{22} = c_p \int_{1288\,m}^{2200\,m} \rho(z)[\theta_{2200\,m} - \theta_z]dz \tag{1.1}$$

where 1288 m represents the height above sea level at the Salt Lake International Airport. It is found through climatology that a series of 3 or more twice-daily soundings each having $H_{22} > 4.04$ MJ $m^{-2}$ is classified as a persistent cold air pool.

## 1.2 Inversion Fog

Fog is defined by the American Meteorological Society (AMS) glossary as water droplets suspended in the atmosphere in the vicinity of the earth's surface that affects visibility. It further states that such fog must reduce visibilities to less than one kilometer. The processes required to form fog occur on the mesoscale, meaning they have an expanse from a few to several hundred kilometers and can form and dissipate in less than a pendulum day (AMS Glossary). Due to large impacts fog can cause on social, economic, and aviation activities, accurate prediction is very important.

Inversion fog is a wintertime radiation fog that forms when polar air stagnates in a valley under the dominance of a persistent high pressure system (Taylor, 1941). It is different from typical valley radiation fog as warm air advection associated with the high pressure system creates a subsidence inversion that acts as a lid to keep the fog in a limited vertical expanse. This type of fog is common in the western United States and central Europe during the winter (Byers, 1959). The topography of a region is important in the development and persistence of this phenomenon. A basin with limited drainage creates the ideal situation for the formation of inversion fog, as the cold air mass near the surface can remain in place.

A subsidence inversion or elevated statically stable layer prevents vertical mixing from occurring. This forms a lid over the basin which traps the cool air within the valley (Holets and Swanson 1981). The air then becomes cooler and more saturated over time as longwave radiation is released from the valley floor and brings the temperature closer to the dew point. Simultaneously, the inversion will lower throughout the prevailing high pressure system's lifetime, concentrating the moisture in the airmass in a limited vertical expanse. Lastly, anthropogenic injections of moisture and particulate matter aid in the moistening of the layer and provide sufficient cloud condensation nuclei for fog formation (Chachere and Pu 2016). After the fog has formed, a major synoptic change such as a frontal system or pressure trough passage is required for vertical mixing and total dissipation of the inversion fog (Holets and Swanson 1981).

## 1.3 Numerical Simulations of Cold Air Pools

Numerical studies have examined cold air pools for both idealized (Zängl 2005a; Lareau 2014) and actual topographic basins (Whiteman et al. 2001; Zängl 2005b, Billings et al. 2006, Neemann et al. 2015). It was found that snow cover makes an incredible contribution to the final solution produced by the model (Billings et al. 2006), as snow-free simulations were incapable of producing a cold pool. Cloud cover is another important mechanism in the formation and maintenance of a cold air pool, as cloud longwave radiation can inhibit the low-level cooling necessary for a strong cold air pool (Zängl 2005a). Finally, fog is known to form in cold air pools. This creates an interesting problem if the environment of the cold air pool is near freezing, as numerical models struggle to accurately represent ice fog (Gultepe et al. 2014).

In the Uintah Basin of Utah, Neemann et al. (2015) found that the Weather Research and Forecasting model (WRF) was able to simulate a strong capping inversion regardless of present snow or cloud cover characteristics. However, the near surface variables were much more influenced by the presence of snow cover and cloud microphysics. The microphysics used to present a realistic vertical profile of temperature and low clouds were heavily modified, suggesting that further understanding of microphysical processes in these valley cold pools are necessary in order to produce accurate simulations.

## 1.4 Numerical Simulations of Fog

Challenges of fog forecasting with the aid of numerical models have been documented for over forty years (Zdunkowski and Neilsen 1969; Zdunkowski and Barr

1972; Brown and Roach 1976; Turton and Brown 1987; Duynkerke 1990; Van der Velde et al. 2010; Steeneveld et al. 2014). Fog forecasting requires an adequate representation of the boundary layer. This involves being able to represent radiative cooling, turbulence, stratified layers, soil-vegetation-atmosphere exchanges, and advection (Bergot and Guédalia, 1994). Unlike most meteorological processes, fog is classified as a "threshold phenomenon." This means that a certain threshold, in this case condensation, has to be accurately predicted in order for the phenomenon to be accurately represented. Condensation time is dependent on temperature and humidity of the lowest layers of the atmosphere, both of which must be predicted with great detail.

At these low layers, however, turbulence is a factor. Welch and Wielicki (1986) support that turbulence aids in the formation of fog, but other authors such as Roach et al. (1976) state that turbulence favors fog dissipation. There is yet another school of thought contending that a better understanding of fog microphysics and its effect on formation is needed to develop an accurate fog forecasting model (Pagowski et al. 2004; Tardif 2007; Gultepe and Milbrandt 2007). However, these near-surface atmospheric variables have notoriously been incorrectly forecast by numerical weather prediction (Liu et al. 2008; Zhang et al. 2013; Massey et al. 2014). Due to a lack of intensive observations in the boundary layer, few studies have examined how these errors in near-surface temperature, relative humidity, etc., can affect fog prediction (Pu et al. 2016).

The majority of studies made with mesoscale models have been concerned with advection fog over sea or coastal regions of the world (Ballard et al. 1991, Pagowski et al. 2004; Nakanishi and Niino 2006). Van der Velde et al. (2010) assessed the strengths and weaknesses of mesoscale modeling for radiation fog at temperatures near freezing,

noting that two state-of-the-art models had problems simulating important aspects of the fog problem. The Weather Research and Forecasting model (WRF) forecasts fog for very few permutations of available parameterization schemes and the High-Resolution Limited-Area Model (HIRLAM) is unable to model fog layer growth beyond the lowest model level. In both models, fog does not persist.

Terrain is another aspect of fog forecasting using NWP. Models used in the forecasting of fog over complex terrain usually do not have sufficiently fine grid spacing to be able to capture local topographic variations (Price et al. 2011). This can cause significant problems in capturing temperature variations created by valley cold air pools and warmer air above terrain height. The errors caused by this lack of detail are directly proportional to the size of the topography being studied. Bigger valleys, such as those studied in Persistent Cold-Air Pool Study (PCAPS; Lareau et al. 2013) are affected less than those studied in the Cold-Air Pooling Experiment (COLPEX; Price et al. 2011) and Meteor Crater Experiment (METCRAX; Whiteman et al. 2008). The presence of mountain-induced flows can also complicate producing a correct model solution as channeled and katabatic winds can influence valley characteristics (Kalverla et al. 2016).

## 1.5 Scope of This Study

This study is a two-fold analysis, the first examining a connection between valley variables and inversion fog events in Salt Lake City, Utah. As alluded to above, inversion fog mechanisms can occur within a deeper topographic inversion caused by valley stable layer processes. Due to relatively calm winds and strong stratification, moisture introduced into a stable valley airmass has limited dispersion (Whiteman et al.

2001). Thus, when confined to a valley or basin, moisture has no channel for vertical or lateral displacement during the cold pool event. Within a stable valley, calm winds, clear skies, maximum radiative cooling, and trapping of moisture are observed. These are also ingredients to a conducive fog environment. However, so far, the relationship between stable valley boundary layers and fog has not been investigated. In light of this fact, Chapter 2 describes a study which runs a statistical analysis on the frequencies of stable valley features and inversion fog events. The aim of this analysis is to determine a statistically significant relation between the two phenomena. Additionally, an analysis of the probability of occurrence of inversion fog given a valley stable layer is performed.

The second part of this study focuses on the predictability of an inversion fog event using numerical simulations. With an advanced research version of the Weather Research and Forecasting (WRF) model (Skamarock et al. 2008), numerical simulations are performed for an inversion fog event over the Salt Lake Valley during the Mountain Terrain Atmospheric Modeling and Observations Program (MATERHORN) (Fernando et al. 2015). As part of the MATERHORN program, the MATERHORN-Fog field project was conducted from 07 January to 1 February 2015 (Pu et al. 2016). Specifically, intensive observation periods (IOPs) 1 and 2 from MATERHORN-Fog were chosen for the numerical studies.

Chapter 3 describes results from a series of WRF simulations of fog events during IOP 2 with sensitivity experiments of various WRF model physical parameterizations. The ultimate goal is to explore and understand factors and processes that could contribute to an accurate numerical simulation of inversion fog.

Chapter 4 includes conclusions from Chapters 2 and 3 and also several concluding remarks.

# CHAPTER 2

# CONNECTIONS BETWEEN COLD AIR POOLS AND INVERSION FOG EVENTS IN SALT LAKE CITY[1]

## 2.1 Introduction

Salt Lake City is located in the Salt Lake Valley and surrounded by mountains except on the northwestern side where the Great Salt Lake sits (Figure 2.1). Under the dominance of a high pressure system, the prevailing wind direction is from the northwest, channeling polar air over the Great Salt Lake and into the Salt Lake Valley. The Great Salt Lake provides a source of moisture (Hill 1988), leading to the trapping of cold and moist airmasses in the valley. During the cold season, cold pools and persistent inversions are often observed in Salt Lake City and its surrounding areas (Lareau et al. 2013, Whiteman et al. 2014) and are mentioned as one of the mechanisms that may have an effect on fog formation during this time of year. In addition, Hodges and Pu (2015) found that the highest frequency of fog observations in Salt Lake City is in December and January. This makes Salt Lake City an ideal site to study the correlations between cold pools and fog events.

Section 2.2 describes the data and methods used in this study. Climatology of the

[1] This chapter has been adapted from an accepted article in *Pure and Applied Geophysics* (2016). doi:10.1007/s00024-016-1316-x

identified diurnal and persistent cold pools as well as their connection with fog events are presented in Section 2.3. Section 2.4 presents the statistical test results and Section 2.5 offers a discussion of these results.

## 2.2 Data and Methods

Sounding and automated surface observing system (ASOS) data were gathered for eighteen winters from the Salt Lake City International Airport (KSLC). Consistent with Whiteman et al. (1999) and Hodges and Pu (2015), the cold season is considered to run from October to March, making the bounds of the dataset between October 1997 – March 2015. Before October 1997, the ASOS station was not operational at KSLC and visibility measurements were not consistent. The University of Wyoming Weather Lab archived the sounding data. The University of Utah MesoWest database (Horel et al. 2002) provided the quality controlled ASOS data. Throughout the duration of the study (October to March over eighteen years), soundings were unavailable for 87 days.[2]

Fog events were identified using the ASOS observations such as visibility, relative humidity, current weather, etc. The definition of fog from the AMS glossary states that the visibility must drop below 1 km, or 0.62 miles. However, ASOS stations report visibility

[2] Dates with unavailable sounding data: 6 October 1997, 29 October 1997, 3 November 1997, 25 December 1997, 29 December 1997, 23 January 1998, 3 February 1998, 27 February 1998, 11-12 March 1998, 23 October 1998, 30 October 1998, 10 November 1998, 15 November 1998, 30 December 1998, 5 January 1999, 22 January 1999, 28 January 1999, 30 January 1999, 3 February 1999, 6 February 1999, 11 February 1999, 19-20 February 1999, 26 February 1999, 28 February 1999, 1-4 October 1999, 14 October 1999, 18-24 October 1999, 27 October 1999, 11 November 1999, 12 December 1999, 15 February 2000, 9-10 March 2000, 4 October 2000, 22 October 2000, 19 November 2000, 6 December 2000, 25 December 2000, 31 December 2000, 4 March 2001, 8-9 March 2001, 18 March 2001, 24 October 2001, 11 November 2001, 13-14 November 2001, 18 November 2001, 17 March 2002, 2 October 2003, 12 January 2004, 20 January 2004, 4 February 2004, 12-13 March 2005, 12-13 February 2006, 20 March 2006, 10 February 2007, 2 February 2008, 15 March 2008, 25 October 2008, 11 October 2009, 7 December 2009, 6 November 2011, 7 December 2012, 27 March 2013, 23-24 December 2013, 10 January 2014, 20 March 2014, 1 February 2015, 19 February 2015, and 6 March 2015.

in increments of 0.25 miles; thus, the visibility is reported as 0.5 miles and/or 0.75 miles instead of exactly 0.62 miles. Therefore, in this study, we choose to use a visibility requirement of less than 0.75 miles in order to meet the fog definition as closely as possible. The criteria used to determine fog is: visibility of 0.75 miles or less and a relative humidity of at least 90%. Fog that was coincident with precipitation is not included in this study because precipitation can interfere with the transmissometer used to measure visibility. A transmissometer is a forward scatter visibility sensor which can consistently report visibility within 10-20% RMSE of observations. Precipitation can also raise the relative humidity, causing erroneous "fog" to be reported by the ASOS station. It is important to note that the definition of fog in this study may be different from the ASOS reported weather observations, as the instrumentation can occasionally report fog at visibilities above the set thresholds. A fog event was counted if fog criteria were met for two or more consecutive, continuous hours from midnight to midnight local time. Namely, fog events are defined on a daily basis in this study, therefore, there are not multiple fog events in any single day.

A "near fog" condition was also defined by Hodges and Pu (2015) and was used to capture the borderline cases of fog and also to increase the size of total sample. "Near fog" is defined as visibility of 3.0 miles or less and a relative humidity of at least 70%. This is consistent with the definition of "near fog" provided by Bergot et al. (2007), as it describes an environment in which fog has the potential to form, but there is some force counteracting its development. As with fog events, "near fog" conditions were considered if they were present for two consecutive hours or more on a given day. It can be argued that haze can be a classification of "near fog" criteria, therefore, if the ASOS station reported haze as

current weather, it was included in this study.

Figure 2.2 presents a sample of a fog event and its subsequent breakup on December 17, 2013. Fog is found in the local morning time (about 00:00 to 10:00 AM MST) with low visibilities, near constant temperature, and high surface pressure under the dominance of a ridge. As a low pressure trough moved through the area, there was enough turbulence to mix out the Salt Lake Valley and raise visibility. These mix-out events are often seen accompanying pressure troughs, regardless if they are associated with frontal systems.

In order to study the connection between valley stable layers and fog events, we examine the correspondence between the frequency of these stable phenomena and occurrence of fog events throughout each cold season and also the monthly means over the eighteen years. Since the soundings are mostly available at 00 UTC and 12 UTC, the statistics on diurnal variation of stable valley boundary layers is not possible, although the diurnal characteristics can still be identified. A chi-square test for independence is employed to check whether the connection between cold pools and fog events is significant (Wilks 2011). The first step in completing a chi-square test of independence is determining the degrees of freedom (*DF*) using the following formula:

$$DF = (r-1)\times(c-1) \tag{2.1}$$

where $r$ is the number of rows in the contingency table, and $c$ is the number of columns (Table 2.1). Then, the expected frequency of each cell in the contingency table is calculated using the following formula:

$$E_{r,c} = \frac{(n_r \times n_c)}{n} \tag{2.2}$$

where $E_{r,c}$ is the expected frequency count of a cell at a certain row $r$ and column $c$, $n_r$ is the total observed frequency of referred columns, and $n$ is the total sample size. These

values appear as the italicized numbers in Table 2.1. The test statistic is a chi-square random variable defined as:

$$\chi^2 = \sum \frac{\left(O_{r,c} - E_{r,c}\right)^2}{E_{r,c}} \tag{2.3}$$

where $O_{r,c}$ is the observed frequency count of a cell in a certain row $r$ and column $c$. As is standard for chi-square tests of independence, two hypotheses are created: a null hypothesis and an alternative hypothesis. The null hypothesis states that the two phenomena in question are independent variables, and the alternative that they are not independent. By comparing the test statistic to a chi-square distribution, we can calculate a p-value and evaluate the significance level to determine if these two variables have an association.

These contingency tables were made for the two different types of stable valley phenomena described in the introduction. The first uses the Wolyn and McKee (1989) definition of a deep stable layer: 65% of the lowest 1.5 km of the 1200 UTC sounding has a lapse rate of 2.5 K/km or less. Persistence was analyzed by looking at consecutive days meeting this criterion. If it was met for one sounding, it is classified as diurnal or less than 24 h. If the necessary conditions were met for four or more consecutive soundings, it was classified as persistent, or lasting longer than 48 h. Anything in between was classified as a short persistent deep stable layer, lasting between 24-48 h.

The second type of contingency table was created using the Whiteman et al. (2014) definition of cold pools, using the valley heat deficit definition. Valley heat deficit ($H_{22}$, Equation 1.1) values were calculated for the entire eighteen-year period. If three or more consecutive soundings exhibited $H_{22} > 4.04$ MJ m$^{-2}$, it was classified as a persistent cold air pool (Whiteman et al. 2014). If a nocturnal sounding (0500 LST) had $H_{22} > 4.04$ MJ

$m^{-2}$, but neither sounding before or after reached this threshold, it was considered a strong diurnal cold pool. After neglecting all values higher than 4.04 MJ $m^{-2}$, the average was calculated across the eighteen years, making $H_{22\_mean}$ = 2.27 MJ $m^{-2}$. If a nocturnal sounding had 4.04 MJ $m^{-2} > H_{22} >$ 2.27 MJ $m^{-2}$, but neither sounding before or after reached this threshold, it was considered a weak diurnal cold pool. A criteria was created for a weak persistent cold pool, 4.04 MJ $m^{-2} > H_{22} >$ 2.27 MJ $m^{-2}$ for three or more consecutive soundings, but there were zero events fitting this definition.

## 2.3 Climatology: Frequency of Deep Stable Layer, Cold Pool, and Fog Events

Figure 2.3 shows the frequency of diurnal and persistent deep stable layers, diurnal and persistent cold pools, fog and "near fog" events for each cold season over the eighteen years. Overall, a total of 92 deep stable layer events occurred over the cold seasons during 1997-2015 period. Of these, 66 are classified as diurnal and 26 are classified as persistent deep stable layers, with durations between 18 h and 120 h (mean duration 38.9 h). There were 1247 identified cold pool dates. Weak diurnal cold pools accounted for 384 days, strong diurnal cold pools accounted for 244 days, and persistent cold pools accounted for 618 days. There were 374 dates identified with fog over the 1997-2015 cold seasons. Of these, 151 met the true fog definition set by the AMS, and 223 met the "near fog." Recall that two continuous hours of fog have to be present in a midnight-to-midnight period in order to be counted as a fog date.

Persistent deep stable layer events are more common than diurnal events. Of the eighteen winters studied, only three years show a higher frequency of a diurnal deep stable

layer. There is wide interannual variability of these events, as some winters can have up to fifteen days identified with a deep stable layer, and some as little as one day per winter. The results from the diurnal cold pools are much more consistent. On average, every winter has about forty-eight days in which a diurnal cold pool is identified. There exists variability in the persistent cold pool data, with frequencies as low as eleven and as high as thirty-three for a given winter. Finally, fog shows the most variability of all, with some winters having as many as fifty days which experience some type of fog, and some having as few as ten.

The mean number of each type of event is by month is presented as Figure 2.4. For the majority of these events, the highest frequencies are seen in the deep winter months, December and January. Each event resembles a normal distribution around these two months, save for diurnal cold pools. The highest frequency of diurnal cold pools is seen in October. This is likely the result of the deep winter months being biased toward persistent cold air pools. By looking at the fog distribution, it is easy to see why connecting the two phenomena can have an important impact on the residents of Salt Lake City. January has the highest frequency of fog, nearly 10 days, one third of the month. Based on Figure 2.4, a qualitative assessment can be made that these three phenomena appear to be well correlated, lending to the notion that deep stable layers, cold pools, and fog could have a statistical dependence upon one another.

## 2.4 Connection Between Cold Pools and Fog Occurrences

### 2.4.1 Chi-square Test of Independence

To determine if there is a significant association between fog events and cold pools, a test of independence is performed on the samples shown in Figure 2.3. Specifically, a chi-square test is applied to determine whether we can achieve the distribution of two events using a normal fit, otherwise, they are assumed to have a statistical dependence. In order to do the test, a contingency table (Table 2.1) is established to show the correspondence between fog events and cold pools. The chi-square test for independence is appropriate for our study because the dataset meets the four criteria for which this test is applicable: (1) it is a simple random sample (a set of observations drawn from a population), (2) the population (the total set of observations that can be made) is at least ten times the size of the sample, (3) the variables under study are categorical, and (4) in a contingency table, as shown in Table 2.1, the frequency for each cell is higher than five (Wilks 2011). Note that because two variables can have a statistically significant association does not mean that the relationship is causal. As a test standard the following hypotheses are stated:

$H_0$: Valley stable airmasses and mountain valley fog events in Salt Lake City are independent.

$H_a$: Valley stable airmasses and mountain valley fog events in Salt Lake City are not independent.

The significance level for which the data is tested is 0.05 for all tests.

We performed the chi-square test four times. The first tests the statistical association between deep stable layers and true fog events (Case A). The second iteration

tests the statistical association between deep stable layer events and "near fog" events (Case B). The third tests the statistical association between cold air pool events and true fog events (Case C). The fourth and lasts tests the statistical association between cold air pool events and "near fog" events (Case D). The wording for each of the hypotheses were changed in accordance to which valley stable airmass was being tested at the time.

Table 2.1 shows the distribution of events identified in which the criteria for each case were met. It was created by considering every stable valley airmass identified over the eighteen-year period and was then divided into whether fog conditions occurred at the same time or not. Using Equation (2.1), the dataset has two degrees of freedom. For Case A, the highest number of coincident fog and deep stable layer events occurred in the diurnal and short persistent categories, both having a frequency of 14. The frequency of long persistent deep stable layers associated with fog is not far behind, at 11. In Case B, the highest frequency is seen in the short persistent deep stable layer category, 53, followed by diurnal, 26. Case C shows the highest frequency of fog events occurred with strong persistent cold pools, 77, followed by strong diurnal cold pools, 13. In Case C, the number of events associated with weak diurnal cold pools is an order of magnitude less, 3. Finally, Case D echoes the distribution seen in Case C.

The chi-square test statistic calculated for Case A is 7.50, for Case B is 8.14, for Case C is 133.29, and for Case D is 302.76. A graph of each chi-square distribution for the deep stable layer cases is displayed in Figure 2.5, with the results from the cold air pool cases in Figure 2.6. The p-values calculated in this test represent the percentage of data that is to the right of the test statistic in a chi-square distribution. Specifically, it is the area to the right of the chi-square test statistic value under a chi-square distribution with the

appropriate degrees of freedom compared to the area of the entire chi-square distribution. This is the basis for accepting or rejecting our null hypothesis, for only if the p-value is below our test threshold can the null hypothesis be rejected, which is our goal. For Case A, the p-value is 0.0275, much lower than the significance level of 0.05. As a result, we can reject the null hypothesis. The p-value is 0.0171 for Case B, which allows a rejection of the null hypothesis once again. For Case C and Case D, the p-values are 0, more than sufficient to reject the null hypothesis for the final two tests. This means that all tests have the ability to reject the null hypothesis. This evidence provides confidence that deep stable layer events are fog events are not independent variables, and neither are deep stable layer and "near fog" events. Using the significance level of 0.05, we can say that these results are correct with 95% confidence. There is also evidence showing that cold air pool events and fog events are not independent variables, and neither are cold air pool and "near fog" events. Since the p-value for both of these tests is zero, we can say these events are not independent with 100% confidence.

### 2.4.2 Probabilities of Occurrence

Joint probabilities of fog with a preexisting stable valley airmass are calculated for deep stable layers and persistent cold pools using the definitions set by Wolyn and McKee (1989) and Whiteman et al. (2014), respectively. This probability was compared to the probability of fog occurring randomly. For this test, the following hypotheses are used:

$H_0$: The probability of a random occurrence of fog is higher than the probability of a fog event with a preexisting stable valley airmass.

$H_a$: The probability of a random occurrence of fog is lower than the probability of a fog event with a preexisting stable valley airmass.

Each hypothesis was tested for the fog and "near fog" cases used in this study.

The relative probabilities for each case is shown in Figure 2.7. In order to determine if the cold pool is a precursor for predicting a fog event, it should be compared to the probability of random occurrence of fog. This can be computed by dividing the number of days that fog or "near fog" criteria was met over the total number of days included in the study. The probability of random occurrence, over all samples in eighteen years is 4.603% for fog, and 11.402% for "near fog." Comparing these results to the probabilities for fog and "near fog" given a deep stable layer, 15.038% and 34.586%, respectively, we see that in every case we can reject the null hypothesis. Therefore, the chance of fog is higher with an existing deep stable layer than a random fog occurrence. When compared to persistent cold air pools, there is a 20.052% chance of developing fog and a 46.615% chance of developing "near fog."

An important caveat to this analysis is that it was performed on a daily basis, meaning that the frequencies are skewed. It should be noted that there are persistent episodes in which fog manifested later in the duration of the event. Therefore, these percentages in the event-wise case can be accounting for days during an event in which fog had not developed, but will develop as the event persists instead of an event in which fog did not develop at all.

This above result confirms that: the stable valley airmass can be an important precursor for predicting fog. For all cases, by having an existing stable valley airmass, the chance of fog generation is higher than that of random occurrence. The relationship to

"near fog" can also be useful for forecasters as these conditions can be preferential for a true fog event to form. This can aid in the issuing of fog advisories during the cold season. It can also be used to predict IMC (instrument meteorological conditions), in which planes must fly without the guidance of visible landmarks. This is especially useful in the Salt Lake Valley, home of Salt Lake International Airport.

## 2.5 Discussion

Relative humidity is the most stringent regiment that can be assessed in concert with low visibility to assess fog formation. In order to test the robustness of the conclusion from this study, the analysis for Case A was performed twice, once with the above fog criteria (90% relative humidity coincident with visibilities less than 1 km) and again with fog criteria having a threshold of 80% relative humidity. The latter test concluded a chi-square test statistic of 9.2803 and a p-value of 0.0097. By this loose criterion, the test remains valid, proving the null hypothesis can be rejected.

Visibility criteria used for this study are consistent with those set by the AMS glossary, but these terms are developed for use in aviation meteorology, in which different types of flight rules are used depending on the visibility (Gultepe et al. 2014). This can add a certain skew to our dataset because an event with sufficiently low visibility and high relative humidity does not mean fog is necessarily present. An inherent uncertainty is therefore present in this dataset as fog events may be identified as "near fog" and some events that meet sufficient criteria may not accurately reflect fog conditions.

## 2.6 Conclusions

Data from eighteen winters were compiled and analyzed to make the first study of the connection between cold air pools and fog occurrence in a mountain valley. Salt Lake City was chosen as a test site because extensive cold pool and fog studies have been performed at this location (Hill 1988; Lareau et al. 2013; Whiteman et al. 2014; Hodges and Pu 2015). The main conclusions from this study can be summarized as:

1. Cold pools are important in the formation of fog events and "near fog" conditions in the Salt Lake Valley, as neither is statistically independent from another.
2. The cold pool definition captures the most important aspects of the vertical profile associated with fog conditions.
3. Fog is more likely to form in environments with a preexisting cold pool.
4. Given a persistent cold pool, there is over a 45% chance of creation of a fog conducive environment.

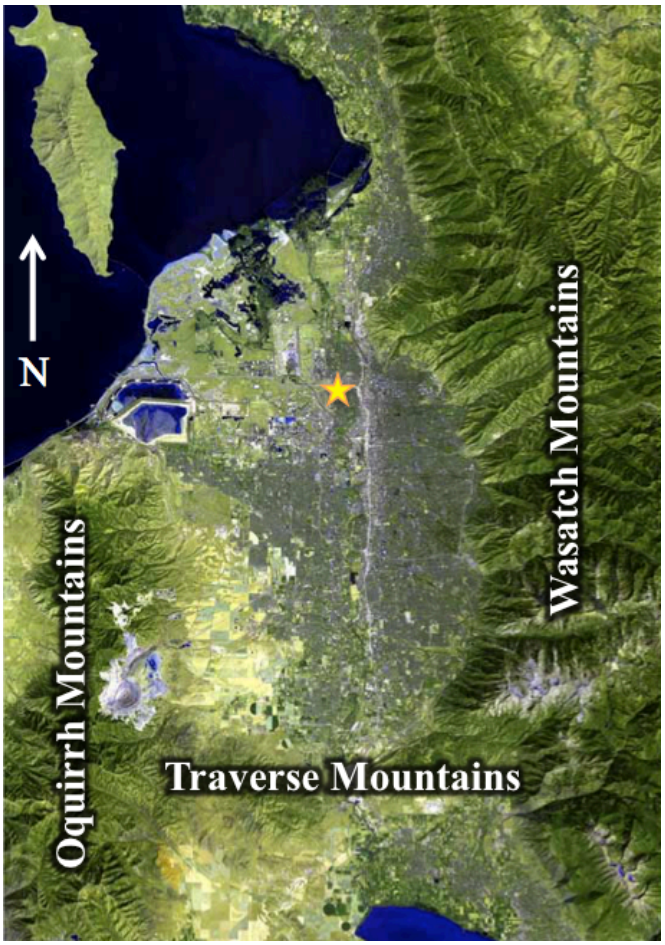


Figure 2.1. A satellite image of the Salt Lake Valley taken 21 October 2006. The Great Salt Lake is visible in the upper left, the Wasatch range along the right, Oquirrh range along the left, and the Traverse are seen separating the Salt Lake Valley in the center from the Utah Valley at the very bottom. The yellow start indicates the center of Salt Lake City.

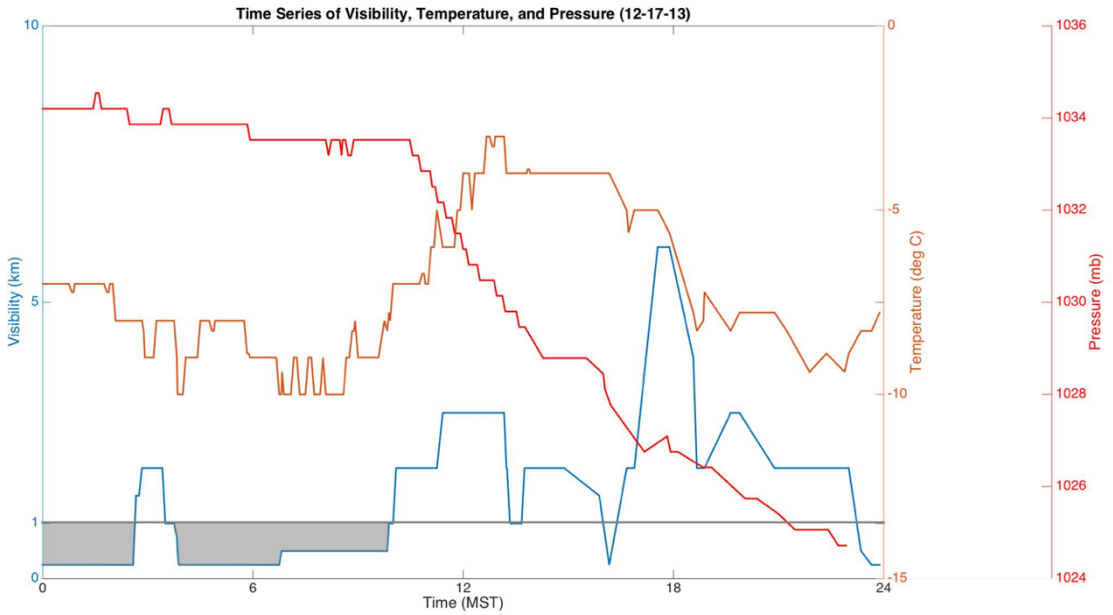


Figure 2.2. Time series of visibility (blue), temperature (orange), and pressure (red) at Salt Lake International Airport (KSLC) on December 17, 2013. Gray line shows the visibility criteria for which fog is defined. Gray shaded areas show where fog criteria persists for more than two hours.

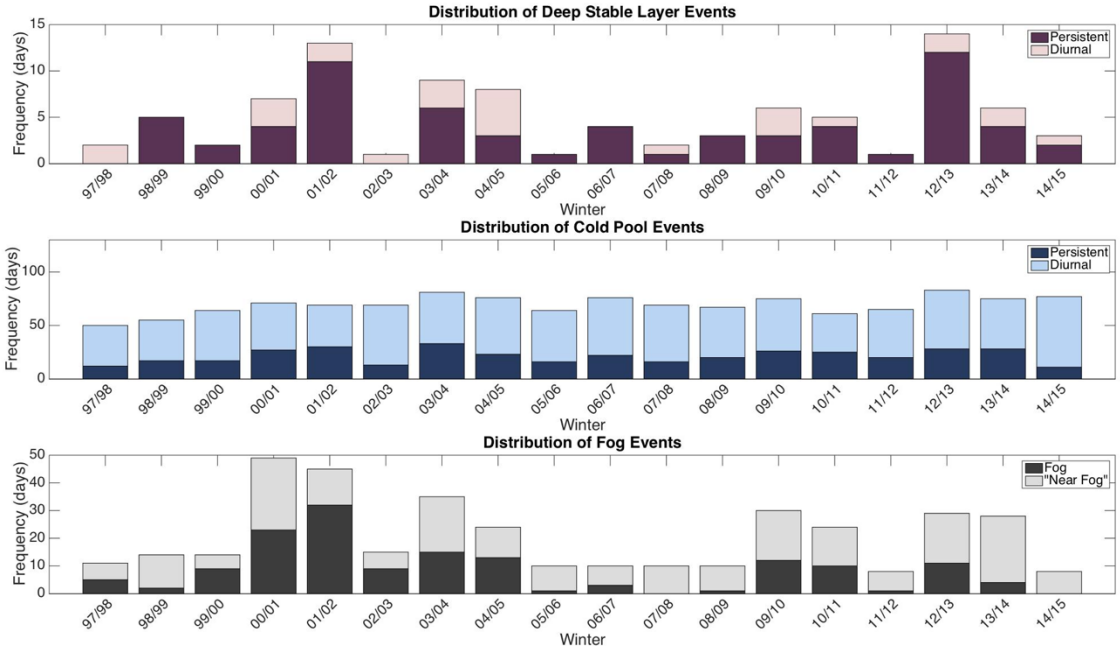


Figure 2.3. The distribution, identified by winter, of the six types of events detailed. Top) Details persistent deep stable layer events (deep purple, meets Wolyn and McKee (1989) criteria for more than 24 h), and diurnal deep stable layer events (light purple, meets Wolyn and McKee (1989) for less than 24 h. Middle) Details persistent cold pool events (deep blue, meets Whiteman et al. 2014 criteria for three consecutive soundings), and diurnal cold pool events (light blue, meets Whiteman et al. 2014 criteria for one 0500 MST sounding and neither adjacent 1700 MST soundings). Bottom) Details true fog events by AMS definition (dark gray), and "near fog" events by Hodges and Pu (2015) definition (light gray).

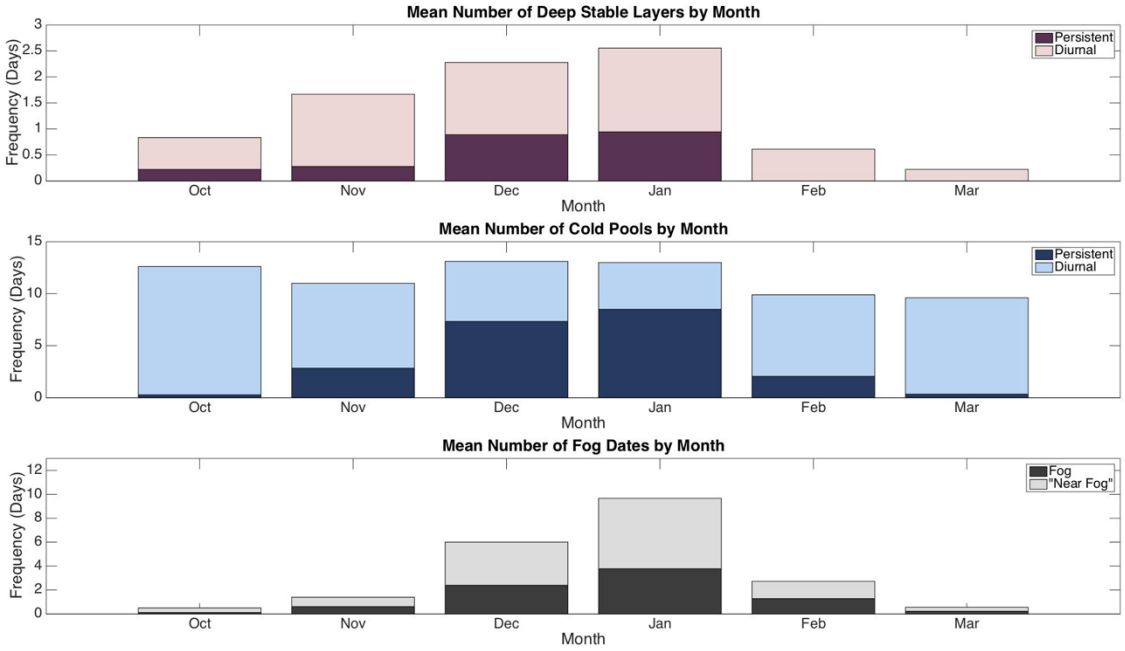


Figure 2.4. Distribution of the mean number of cold pools and fog dates by month. Top) Details persistent deep stable layer events (deep purple, meets Wolyn and McKee (1989) criteria for more than 24 h), and diurnal deep stable layer events (light purple, meets Wolyn and McKee (1989) for less than 24 h. Middle) Details persistent cold pool events (deep blue, meets Whiteman et al. 2014 criteria for three consecutive soundings), and diurnal cold pool events (light blue, meets Whiteman et al. 2014 criteria for one 0500 MST sounding and neither adjacent 1700 MST soundings). Bottom) Details true fog events by AMS definition (dark gray), and "near fog" events by Hodges and Pu (2015) definition (light gray).

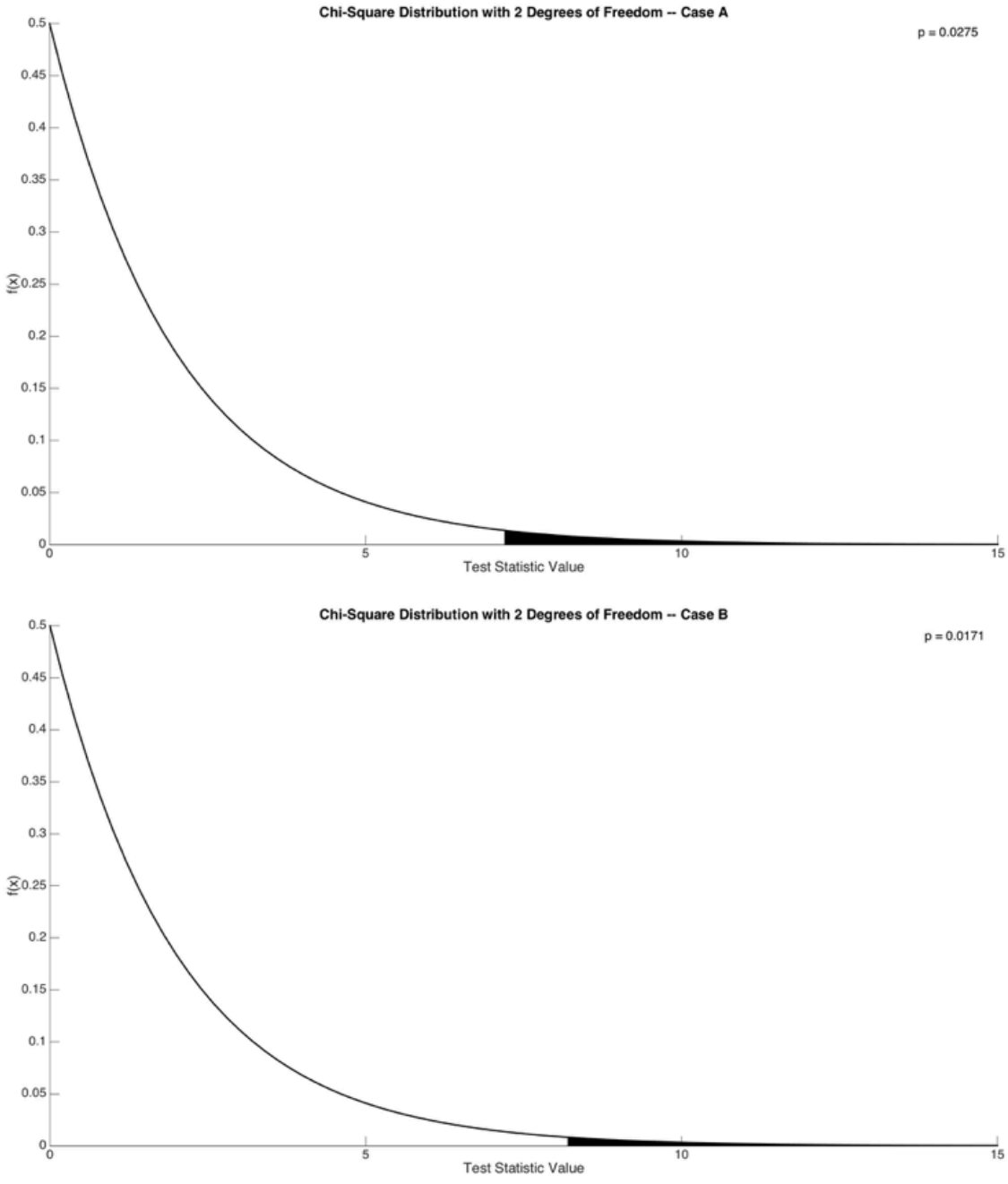


Figure 2.5. Chi-square distributions for the two deep stable layer cases. Chi-square test statistic values plotted on the x-axis. Color fill represents the area above the test statistic values, indicating the p-value of the statistical test, which is also printed above each curve.

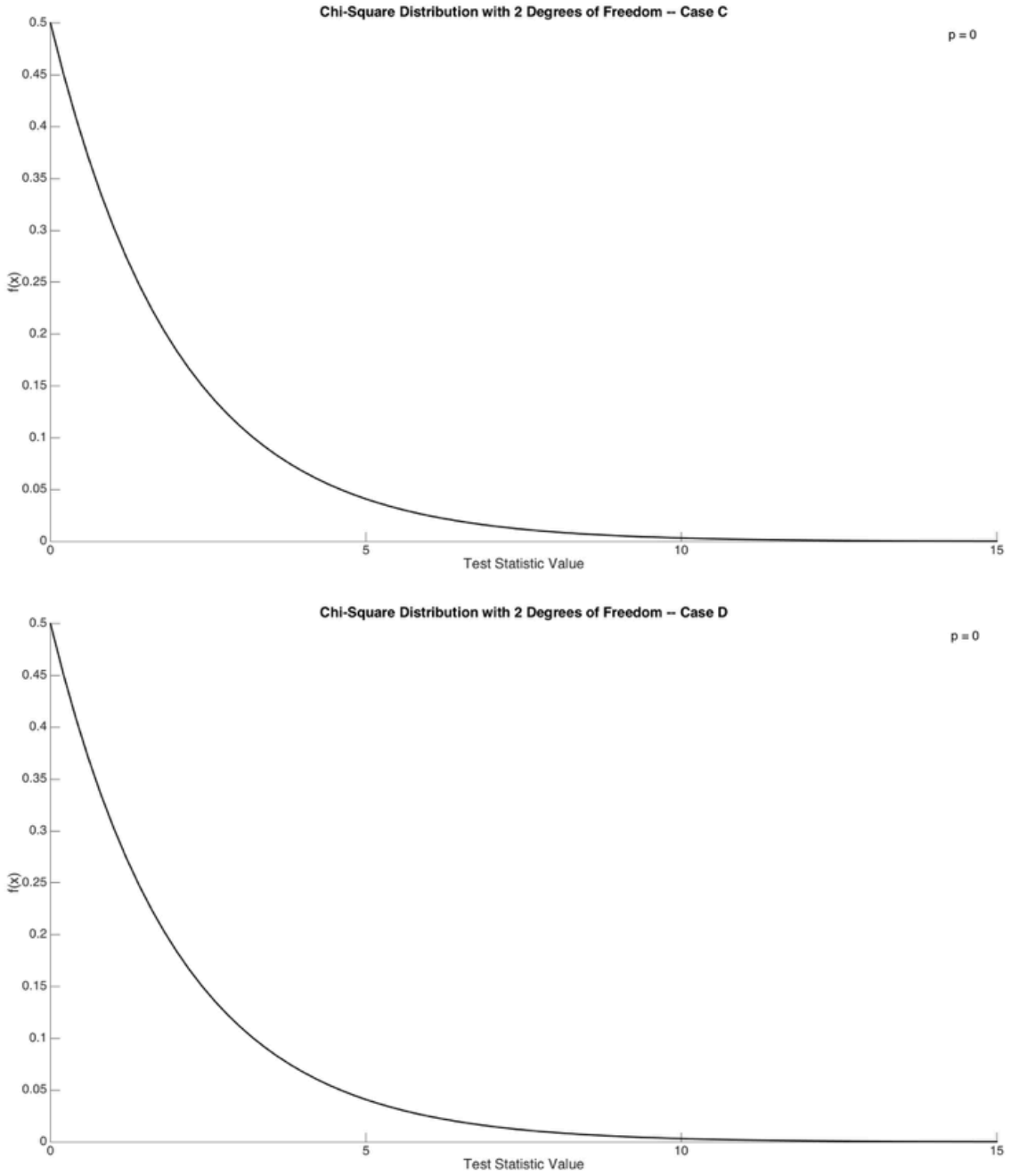


Figure 2.6. Chi-square distributions for the two cold air pool cases. Chi-square test statistic values plotted on the x-axis. Color fill represents the area above the test statistic values, indicating the p-value of the statistical test, which is also printed above each curve.

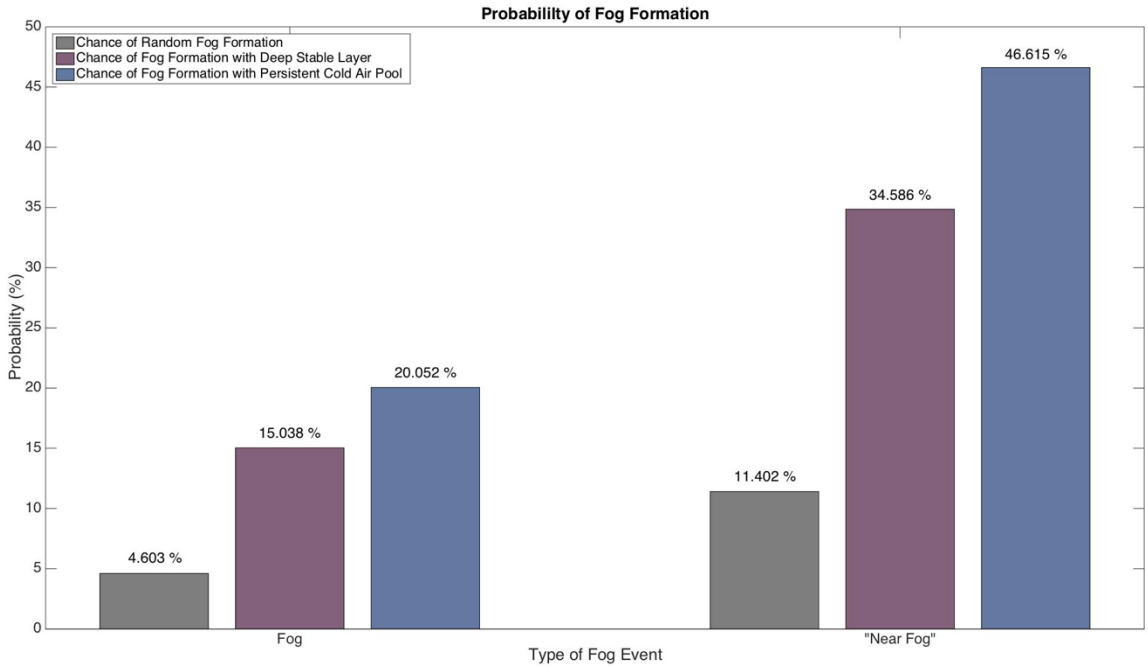


Figure 2.7. Probability of fog or "near fog" generation randomly (gray) against the probability of the same events with a preexisting deep stable layer (purple) and a persistent cold air pool (blue).

Table 2.1. Contingency tables for Case A (deep stable layer vs. fog), Case B (deep stable layer vs. "near fog"), Case C (cold air pool vs. fog), and Case D (cold air pool vs. "near fog"). Bold values indicate frequency of observation and italicized values in parentheses indicate expected values given a normal distribution.

| | Duration of Deep Stable Layer | | |
|---|---|---|---|
| | Less than 24 h | 24 – 48 h | Over 48 h |
| Case A – Deep Stable Layer vs. Fog | | | |
| Fog reported | **14** (*15.34*) | **14** (*18.11*) | **11** (*5.55*) |
| No fog reported | **91** (*89.66*) | **110** (*105.89*) | **27** (*32.45*) |
| Case B – Deep Stable Layer vs. "Near Fog" | | | |
| "Near fog" reported | **26** (*36.18*) | **53** (*42.73*) | **13** (*13.09*) |
| No "near fog" reported | **79** (*67.64*) | **71** (*81.27*) | **25** (*24.91*) |

| | Type of Cold Air Pool | | |
|---|---|---|---|
| | Weak Diurnal | Strong Diurnal | Strong Persistent |
| Case C – Cold Air Pool vs. Fog | | | |
| Fog reported | **3** (*46.13*) | **13** (*18.21*) | **77** (*28.66*) |
| No fog reported | **615** (*571.87*) | **231** (*225.79*) | **307** (*355.34*) |
| Case D – Cold Air Pool vs. "Near Fog" | | | |
| "Near fog" reported | **20** (*114.07*) | **31** (*45.04*) | **179** (*70.88*) |
| No "near fog" reported | **598** (*503.92*) | **213** (*198.96*) | **205** (*313.12*) |

# CHAPTER 3

# NUMERICAL SIMULATIONS OF AN INVERSION FOG EVENT IN THESALT LAKE VALLEY DURING MATERHORN-FOG IOPS 1 AND 2

## 3.1 Introduction

Due to large impacts fog can cause, accurate prediction of a fog event is very important. It is especially essential for Salt Lake City because it is home to the Salt Lake City International Airport as well as a populous of over one million residents. However, thus far, there have not been many studies to evaluate whether numerical weather prediction can accurately predict fog events (Zhou et al. 2012). Very few studies emphasize inversion fog events. As mentioned in the introduction, fog forecasting requires adequate representation of the boundary layer and near-surface atmospheric conditions. Due to a lack of intensive observations in the boundary layer, few studies have examined how these errors in near-surface temperature, relative humidity, etc., can affect fog predictions (Pu et al. 2016).

In order to improve the understanding of complex-terrain meteorology over a wide range of scales and topographic features, the Mountain Terrain Atmospheric Modeling and Observations Program (MATERHORN) (Fernando et al. 2015) has been conducted in

northern Utah. As part of the MATERHORN program, the MATERHORN-Fog field project was conducted from 07 January to 1 February 2015 (Gultepe et al. 2016). The overall objective of this campaign is to improve the understanding of mechanisms associated with the formation, evolution, and dissipation of fog over complex terrain (Gultepe et al. 2016). Over the course of the campaign, eleven intensive observational periods (IOPs) were performed, ten in January and one in February of 2015 over four major fog events.

During the MATERHORN-Fog field observations, real-time forecasts were conducted with the WRF model (Pu et al. 2016). The real-time forecasts were useful for planning operations during the field project, as well as the evaluation of the performance of the WRF model with observations after the field program. Early evaluation shows the inability of the WRF model to reproduce correct forecasts of near-surface atmospheric variables. The model was able to capture the elevated subsidence inversion commonly seen in valley cold pools associated with inversion fog events, but large errors in temperature, dew point, and wind speed were seen in the boundary layer.

In light of the lack of understanding and studies of inversion fog events as well as the problems with the real-time WRF forecasts during the MATERHORN-Fog field program, in this chapter, we describe a series of numerical simulations of an inversion fog case over Salt Lake City during the MATERHORN-Fog field project. Leveraged by the intense observations obtained during the field program, it is our purpose to further pinpoint the main problems with WRF in simulating the fog events. Through different model configurations and a series of sensitivity studies, we will explore the factors and processes that could contribute to an accurate numerical simulation of inversion fog.

Section 3.2 describes MATERHORN-Fog IOPs 1 and 2. The numerical model and experiment design are discussed in Section 3.3. Results from the examination of sensitivity to CM, PBL, radiation, land surface schemes, and lead time are presented in Section 3.4. Finally, a discussion of the results follows in Section 3.5.

## 3.2 Synoptic Overview of the Inversion Fogs During IOP 2

The first and second IOP (IOP 1 and 2) from the MATERHORN-Fog campaign (Fernando et al. 2015) took place between 1500 MST 08 January 2015 and 1200 MST 09 January, and 1400 MST 9 January 2015 and 1200 MST 10 January 2015, respectively. The field campaign implemented radiosondes, sodar, and lidar instruments at the Salt Lake site, which is close enough (15 km) to the Salt Lake International Airport (KSLC) for METAR observations and NWS soundings to be sufficient proxy for current conditions in addition to MATERHORN specific observations. The authors made use of the University of Utah's MesoWest network (Horel et al. 2002) during this campaign and provided data real-time from surface observation stations. Figure 3.1 illustrates a time series of visibility, temperature, and pressure at KSLC for the entirety of IOPs 1 and 2. Two periods of near fog occur during these IOPs, with Near Fog Period 1 from 0000 MST to 1800 MST 09 January and Near Fog Period 2 from 2200 MST 09 January to 1200 UTC 10 January 2015. IOPs 1 and 2 were conducted in a two-day fog event, beginning on January 8, 2015.

Prior to fog formation, the prominent feature of the synoptic conditions at 0000 UTC 8 January 2015 was the longwave ridge at 500 hPa (Figure 3.2). It was oriented from NW-SE with the axis extending from the Pacific northwestern coast and curving down into western Texas. It is important to mention this ridge, as it is a significant factor in the

development of the decoupled vertical profile needed for inversion fog formation in this region (Taylor 1941, Hodges and Pu 2015). The orientation of the ridge is conducive for a favorable fog environment as warmer air was being advected in from the south at this level. However, at 850 hPa (Figure 3.3) the axis of the ridge supported the advection of cooler temperatures from a relative temperature minimum in southeastern Oregon. This type of advection pattern supports the formation of the temperature inversion displayed in the sounding at this time (Figure not shown), but it has not yet reached the surface, a scenario typical of fog conditions. From 0000 UTC 8 January 2015 to 0000 UTC 9 January 2015, the ridge changed its orientation from NW-SE to NNW-SSE, shifting the source region of the midlevels from the Pacific to warmer inland air. After this shift, the temperature inversion extended to the surface and fog formed at the Salt Lake MATERHORN observation site.

IOP 2 began with a 500 hPa ridge aligned in much the same fashion as during the previous twelve hours. At 250 hPa (Figure 3.4), the strongest winds were downstream of the ridge, allowing it to remain relatively stationary and for the central pressure to build. The center of anticyclonic rotation was over Nevada at 1200 UTC 9 January at 500 hPa (Figure 3.5), leaving advection into this level unperturbed for 24 h. The sounding (Figure 3.6) shows a saturated surface as fog had formed in the valley within the previous 24 h. This can be seen as part of Near Fog Period 1 in Figure 3.1. More importantly, it shows a decoupled wind profile between the surface and the air above terrain height (~2200 m). A decoupling can be identified by low level winds that are independent of speed and direction of the air above them, a feature that is often coincident with a temperature inversion. This is indicative of a cold air pool, and environment that is very important to the evolution of

fog (Wolyn and McKee 1989; Whiteman et al. 2014; Chachere and Pu 2016). By 0000 UTC 10 January, a trough upstream of the dominating longwave ridge had reached the Pacific coast at 500 hPa (Figure 3.7). Valley cold pools are often broken by strong trough passages, making this a strong indicator that the existing fog environment could soon be destroyed. However, with the dropping temperatures associated with sunset and the inversion still present in the sounding (Figure 3.8), fog can once again be expected overnight throughout the end of IOP 2.

The next 24 hours, from 1200 UTC 10 January 2015 and into 0000 UTC 11 January 2015, the atmosphere began mixing with the approach of the low pressure trough at 500 hPa (Figure not shown). The trough passed over northern Utah between 1800 UTC and 2300 UTC, but it was difficult to pinpoint an exact time of passage because there was never a complete dissolution of the stable airmass in the valley.

## 3.3 Simulation Design

Numerical simulations were performed using WRF Version 3.7 (Skamarock et al. 2008). Four one-way nested domains were used with a horizontal grid resolution of 30 km, 10 km, 3.33 km, and 1.11 km (Figure 3.9). The high-resolution domain (d04, 1.11 km resolution) is centered around the Great Salt Lake and the Salt Lake and Heber observation sites. The model physics options are the same for every domain except for the cumulus scheme, where the Kain-Fritsch parameterization is only used for the two outer domains d01 and d02, at 30 km and 10 km grids, respectively. The control run is set up with the Thompson microphysics scheme, the Rapid Radiative Transfer Model (RRTM) longwave radiation and Dudhia shortwave radiation schemes, and the YSU planetary boundary layer

scheme. All details and descriptions of the parameterization schemes can be found in Skamarock et al. (2008). The correct simulation of the near surface conditions is essential in attaining a correct fog forecast (Pu et al. 2016). The Noah land surface model (Chen and Dudhia, 2001) was used, as it is an advanced land surface model that can predict surface temperature, soil moisture, and temperature in multiple soil layers. The NCEP North American Model (NAM) analysis was used as the initial and boundary conditions. A 48 h simulation was conducted and was initialized at 1200 UTC 8 January.

A real-time WRF forecast was conducted during the MATERHORN-Fog field campaign, with the same model setting as described above and 41 vertical sigma levels. Postfield evaluation (Pu et al. 2016) indicated that the largest errors that occurred in the real-time WRF forecasts are due to a misrepresentation of the boundary layer, especially near the surface (such as 2-m temperature and 10-m winds). In order to better represent the vertical scale of valley phenomena, in this study we changed the number of model vertical levels from 41 to 61. This included lowering the height of the bottom level of the model (~18 m in current control run versus ~30 m in the real-time WRF run) and placing the additional nineteen levels in the planetary boundary layer. Figures 3.10-3.12 compares the near-surface relative humidity, temperature, and wind from model forecasts with tethersonde balloon taken during MATERHORN-Fog IOP 2 at the Heber site (the only tethersonde balloon site) at 0900 UTC 10 January 2015. It clearly illustrates that the simulation with 61 vertical level resolution more accurately represents the lowest levels of the model domain. Although the improvements are by fractions of degrees in temperature and less than five percent in relative humidity, it is these small changes that the model has

to capture in order to represent the conditions in which fog forms. The results motivate us to set the vertical resolution for all experiments in this study to 61 levels.

The WRF model has multiple options for each type of physical parameterization schemes. In order to investigate the sensitivity of numerical prediction of inversion fog to various physical processes and in order to understand which processes might contribute to the fog development and evolution, a total of fourteen (including control) sensitivity experiments were conducted to compare results against the control described above. For each of the sensitivity tests, only one type of parameterization varies from the control simulation in the WRF model. Specifically, sensitivity to cloud microphysics (CM), planetary boundary layer (PBL), radiation, and land surface schemes were tested.

Among these sensitivity experiments, four CM sensitivity experiments were performed with the Thompson (control), Thompson aerosol aware, Lin, and Morrison microphysics. Two special experiments were conducted using the Thompson Aerosol Aware CM scheme to examine the effects of the aerosol concentration and how it acts as cloud condensation nuclei, an important component of fog formation. This selection is based on the fact that Salt Lake City has particularly high concentrations of anthropogenic aerosols in the wintertime. One experiment was run using a logarithmic decay of aerosol concentration with height (a sufficient approximation), and the other was run using a climatology of aerosols based on ten years of observed aerosol data that was collected and manually injected into the model (Colarco et al. 2010). The Lin microphysics scheme uses a five-class hydrometeor system that includes ice sedimentation, which was employed to test ice fog conditions. Finally, the Morrison scheme was chosen to test the sensitivity of single-moment vs. double-moment parameterizations of cloud microphysics.

One sensitivity experiment was conducted to examine how planetary boundary layer parameterization influenced the results and the Mellor-Yamada-Janjic (MYJ) PBL scheme was included in the sensitivity experiment. This choice examined the influence of first order versus 1.5 order parameterization of vertical mixing.

Two tests were implemented to study the differences that shortwave radiation schemes would produce on the results, and the Goddard and RRTMG shortwave radiation schemes were chosen to compare to the control. The Goddard shortwave scheme will include an ozone profile that is not present in the control, and the RRTMG can interact with cloud fractions instead of only fully resolved clouds.

A separate set of tests were performed to test the influence of longwave radiation parameterizations on the results, conducted with the Goddard and GFDL (Eta) longwave schemes. The Goddard scheme was chosen for the same reason as above, but the GFDL scheme was chosen because it uses spectral calculation instead of a discrete calculation system.

The land surface scheme was changed to the thermally diffusive scheme as another experiment. This was chosen based on the thermally diffusive scheme's ability to recognize snow cover at the surface. The final experiment also changed the land surface, where a control simulation was initialized with forced albedo values from observations. Table 3.1 summarizes the configurations of all experiments.

The evaluation of real-time WRF forecasts also shows that the simulation of fog events is sensitive to the forecast leading time (Pu et al. 2016). Considering the model spin-up period, the initialization time of 1200 UTC 8 January, twenty-six hours before the start of IOP 2 was chosen for most of the simulations. We then investigate the dependence

of the numerical simulations on initialization time. Three simulations with the same configuration as the above control, Lin microphysical, and thermal diffusion land surface schemes were tested. The initialization time was changed from 1200 UTC 8 January 2015 to 0000 UTC 9 January 2015.

Two algorithms for visibility were used in this study. The first is based on Gultepe and Milbrandt (2009) and the parameterization is as follows:

$$VIS_{RH_{5\%}} = -0.000114RH^{2.70} + 27.45 \quad (3.1)$$

Relative humidity values used for this parameterization were corrected, meaning they are calculated differently based on relative humidity to water at temperatures above 0.5 °C and relative humidity with respect to ice at temperatures below this value. Instead of choosing 0 °C as the threshold, this study choses 0.5 °C due to the nature of the temperature in this IOP to hover around freezing. This calculation will include all of the borderline values. The second algorithm used is based on Stoelinga and Warner (1999). This algorithm is based on the extinction of five types of hydrometeors: cloud water ($\beta_{cw}$), rain water ($\beta_{rw}$), cloud ice ($\beta_{ci}$), snow ($\beta_{sn}$), and graupel ($\beta_{gp}$). Henceforth, this will be called the GSD parameterization as the algorithm was further developed by the Global System Division (GSD), ESRL/NOAA. It is presented as follows:

$$\beta = \beta_{cw} + \beta_{rw} + \beta_{ci} + \beta_{sn} + \beta_{gp} + 1^{-10} \quad (3.2)$$

where $\beta$ is the extinction coefficient for the five water species, calculated:

$$\beta_{cw} = 144.7{C_{cw}}^{0.88} \quad (3.3)$$

$$\beta_{rw} = 2.24{C_{rw}}^{0.75} \quad (3.4)$$

$$\beta_{ci} = 327.8C_{ci} \quad (3.5)$$

$$\beta_{sn} = \alpha_{sn} \times C_{sn} \tag{3.6}$$

$$\beta_{gp} = 4.0 C_{gp}^{\,0.75} \tag{3.7}$$

where $C_{cw}$, $C_{rw}$, $C_{ci}$, $C_{sn}$, and $C_{gp}$ are the associated mass concentrations (g/m$^3$) for cloud water, rain water, cloud ice, snow, and graupel, respectively. This is then input into a visibility format:

$$VIS_{hydro} = min\left(90., \frac{\alpha_{vis}}{\beta}\right) \tag{3.8}$$

where

$$\alpha_{vis} = -\ln(0.02) \tag{3.9}$$

by Kunkel (1984). The extinction coefficient of snow ($\alpha_{sn}$) varies with temperature as:

$$\alpha_{sn} = 10. \times \left(1 - \alpha_{temp}\right) + 6.0 \alpha_{temp} \tag{3.10}$$

where

$$0 < \alpha_{temp} < 1, \qquad if\ 0 < Temp < 1 \tag{3.11}$$

$$\alpha_{temp} = 0, \qquad if\ Temp < 1 \tag{3.12}$$

$$\alpha_{temp} = 1, \qquad if\ Temp \geq 1 \tag{3.13}$$

The impact of night and day is also taken into effect, and the visibility is modified as:

$$VIS_{hydro\_n} = 1.69 \times 1.609 \times \left(\frac{VIS_{hydro}}{1.609}\right)^{0.86} \tag{3.14}$$

$$VIS_{hydro\_dn} = \alpha_{dn} \times VIS_{hydro} + (1 - \alpha_{dn}) \times VIS_{hydro\_n} \tag{3.15}$$

where $\alpha_{dn}$ is 0 for night time hours and 1 for day time hours. $VIS_{hydro}$ is then compared to a relative humidity visibility parameterization:

$$VIS_{rh} = 60.0 \times exp(-2.5 \times q_{rh}) \tag{3.16}$$

where

$$q_{rh} = min\left(0.8, \left(\frac{rh}{100. - 0.15}\right)\right) \tag{3.17}$$

with *rh* interpolated from the highest values of the lowest four model levels. When $VIS_{rh}$ is less than 10 km, the effect of low-level wind shear between the lowest 4 levels increasing from 4 to 6 m/s is taken into account. This modification of visibility is:

$$VIS_{rh}(ws) = VIS_{rh} + \alpha_{ws} \times (10 - VIS_{rh}) \tag{3.18}$$

where $\alpha_{ws}$ is the impact factor of wind shear ranging from 0 to 1, 0 for wind shear equal to 4 m/s and 1 for with shear over 6 m/s. After this computation is complete, the simplified form of the parameterization can be computed:

$$VIS_{GSD} = \min\left(VIS_{rh}, VIS_{hydro\_dn}\right) \tag{3.19}$$

Results from these visibility algorithms will be analyzed compared to observations during MATERHORN IOPs 1 and 2.

## 3.4 Evaluation of Simulation Results

The results from the control and the sensitivity experiments will be compared with observations. First, the synoptic conditions will be assessed to determine if, as in Pu et al. (2016), the errors are confined to the boundary layer. Then, an evaluation of the control simulations is performed by comparing with observations taken during MATERHORN-Fog. This will be followed by a comparison of each sensitivity experiment to the control simulation.

### 3.4.1 Control Simulation vs. Observations

#### *3.4.1.1 Synoptic Conditions*

Figures 3.13-3.15 compare synoptic maps valid during the MATERHORN-Fog experiment with the WRF-generated control experiment solution valid at 1200 UTC 9 January 2015 at 250 hPa, 500 hPa, and 700 hPa pressure levels. As discussed in the synoptic overview, the most important features to be captured are the longwave ridges seen at each pressure level along with their associated high height features. Dashed orange lines and blue "H"s have been drawn on each figure in order to better see their placement. After a close comparison, it is noted that the WRF model captures the synoptic setup quite well. At each level, agreement is present in height, ridge placement, wind speed and direction, temperature, and relative humidity values are seen. These results are consistent regardless of sensitivity experiment or lead time, indicating that the WRF model has sufficiently represented the synoptic background for IOPs 1 and 2.

The only discrepancies can be found at the 700 hPa level, often at the top or near the top of the boundary layer throughout the entirety of the experiment. Although the errors are slight (temperatures about two degrees warmer than observed), they should be associated with simulation errors in the boundary layer. Pu et al. (2016) indicated apparent errors in these layers with the real-time WRF forecasts. In the following sections, further evaluation in the boundary layer is conducted by comparing simulation results from various experiments with observations during MATERHORN-Fog.

### *3.4.1.2 Boundary Layer Conditions*

Figures 3.16-3.21 illustrates the results of the control simulation for the Salt Lake Valley site. Figure 3.16 compares the sounding profiles from the control simulation and the National Weather Service sounding released at the Salt Lake City International Airport, less than 15 km from the Salt Lake Valley site. The sounding reveals what the synoptic maps alluded to in the previous section: errors are almost entirely confined to the boundary layer. While there is evidence of a decoupling in the wind profile, coincident with the temperature inversion, the model is not producing fog due to errors in temperature and dew point temperature. Temperatures are at most three degrees higher than observations throughout the boundary layer, and dew points are two degrees lower. This creates erroneously low relative humidity values, as the absolute humidity predicted by the WRF is correct when compared to observations (Figure 3.19).

Figures 3.17–3.21 display the time series of WRF control simulations of temperature, dew point temperature, relative humidity, absolute humidity, and wind speed with ASOS station data. They show that the small errors in the prediction of near surface variables in the WRF can lead to big errors in a fog forecast. Figures 3.17 and 3.18 shows that the model accurately captures the maximum temperatures and dew point temperatures seen in each diurnal cycle. However, between 2300 MST 08 January and 0800 MST 09 January, temperatures are over forecasted by as many as three degrees and dew point temperatures are over forecasted by as many as two degrees. Looking at the absolute humidity time series (Figure 3.19), the WRF has produced more moisture during these hours than what is observed (a 0.08 $g/m^3$ moisture bias). This is echoed in the relative humidity time series (Figure 3.20), where the WRF predicted much higher relative

humidity values than observed. The wind speed time series (Figure 3.21), however, shows that the WRF solution has values within one meter per second of those observed. An accurate forecast of this variable is vital in the prediction of fog, as winds that are too high can mechanically mix the column and advect what fog does form away from the observation site. Figure 3.22 shows the visibility forecast from the relative humidity visibility algorithm. The blue shading shows where near fog was observed at the Salt Lake Valley site, and the red shading shows where it is predicted by the model. The relative humidity used in this algorithm is the corrected relative humidity as described above, where ice is taken into effect. In the observations, the near fog was observed from 0000 MST to 1500 MST 09 January and from 2200 MST 09 January to 0500 MST 10 January, but the model does not predict fog past 0800 MST 9 January.

The second period of fog is missed altogether in Figure 3.22. This is mainly due to a six-degree error in forecasted temperature by the WRF (Figure 3.17). When combined with relatively little error in dew point temperature, the relative humidity is too low, as seen in Figure 3.20. Erroneously low relative humidity values affect the way the RH visibility algorithm performs. Figure 3.23 shows the GSD visibility time series. Using this parameterization, the WRF does not produce the necessary conditions to predict fog.

### 3.4.2 Sensitivity of Fog Simulations to WRF Physical Parameterization Schemes

#### *3.4.2.1 Microphysical Schemes*

Four cloud microphysics sensitivity tests were performed: Thompson Aerosol Aware with climatology, Thompson Aerosol Aware without climatology, Lin, and

Morrison microphysics schemes. Figures 3.24–3.29 shows results from the Thompson Aerosol Aware with climatology simulation and the Lin simulation in Figures 3.30–3.36. These two tests were chosen to be represented in the figure because there was no significant difference between the Thompson aerosol aware with climatology and without climatology, nor between the Morrison and the control. The lack of difference between the aerosol schemes is surprising because Salt Lake City suffers from the trapping of anthropogenic particles in cold air pools during the winter, but because there are sufficient cloud condensation nuclei, this did not make much of a difference in the simulations. Both Aerosol Aware schemes did not produce a valuable fog forecast mainly due to temperature error.

Using the Lin microphysical scheme, the WRF model predicts near-surface atmospheric variables much more effectively than any of the other schemes, namely a sharp reduction in temperature error after 0500 MST 09 January. Instead of the three-degree warm bias seen in the control and Thompson Aerosol Aware simulations, we see a cold bias in the Lin microphysics scheme after the above time. At any given point after 0500 MST 09 January, the modeled temperatures are about two degrees cooler than observed. This is due to the generation of clouds in the WRF (Figure 3.32). They manifest at 0500 MST 09 January, and remain over the Salt Lake Valley MATERHORN observation point through the end of the model simulation.

Due to these changes in temperatures, one might expect the WRF to handle absolute humidity differently, and this is the case. Looking at the absolute humidity time series (Figure 3.33), the maximum error seen throughout the duration of the simulation is 0.04 $g/m^3$, half of what was produced in the control simulation. However, because the amount

of moisture is correct, the cold bias in temperature produces excess relative humidity after 0500 MST 09 January (Figure 3.34). The relative humidity values exceed the observations by as much as 20%. This implies a bias when using the relative humidity to produce a visibility forecast, and this is seen in Figure 3.35. The Lin cloud microphysics scheme, however, does produce a second period of fog where every other sensitivity test, thus far, has not (Figure 3.36). There are periods of false positives (between 2000 MST 08 January and 0000 MST 09 January and between 1800 MST and 2200 MST 09 January). The period between fog events is also forecast incorrectly, falling between 1200 MST 09 January and 1600 MST 09 January, but the duration between fog events is four hours in both cases. The GSD visibility algorithm was also tested for this experiment, and was able to represent two distinct periods of fog (Figure 3.37). The first period was much shorter than observed, only lasting between 0600 and 1200 MST 09 January, and the second was longer than observed, spanning from 1600 MST 09 January to 0500 MST 10 January. As with the relative humidity visibility algorithm, although the timing was wrong, the amount of time between each period of fog was forecast correctly.

The Morrison cloud microphysics scheme (Figures not shown) echoed the errors seen in the control simulation. Although the absolute humidity produced by the run was within one $g/m^3$ of what was observed, the warm temperature bias produced relative humidity values that were too low to represent fog. This problem was once again not remedied using the GSD visibility parameterization.

### *3.4.2.2 Planetary Boundary Layer Schemes*

To examine the effect of the planetary boundary layer (PBL) scheme, the MYJ scheme was chosen to compare against the control YSU PBL scheme. The simulation results with the MYJ scheme are consistent with the control, the warm bias in temperature skewing the relative humidity toward drier than observed values. Of particular interest in this iteration is the wind profile seen in the sounding at Salt Lake City (Figure 3.38). The winds simulated throughout the boundary layer, specifically at the top of the temperature inversion, are much higher than observations. The model produced winds are nearly five m/s in excess of the observations at terrain height.

At the surface, the relative humidity values predicted by the model were also much too low in comparison to those observed, arising from errors in the forecast temperature (Figures 3.39 – 3.41). Like every simulation except for the one with Lin microphysics scheme, fog under predicted using the relative humidity visibility algorithm (Figure 3.42), but it did not last long enough nor was the second fog period predicted. The GSD visibility algorithm also did not produce visibilities lower than 6 km throughout the duration of the simulation (Figure 3.43). This sensitivity test is among the weakest performers in capturing the fog.

### *3.4.2.3 Land Surface Schemes*

Since the MATERHORN-Fog field campaign was conducted during the winter, it is important that the winter characteristics of the land surface be captured. In order to accurately represent the present snow and ice cover, a sensitivity test was conducted using the thermal diffusion land surface scheme and another was run with forced initial albedo

values.

Temperatures produced by the thermal diffusion scheme in the sounding presented in Figure 3.44 follow the observation much more closely than any of the sensitivity experiments in this study. Figure 3.45 shows that the simulation has successfully reproduced temperatures with the most consistency with observations (within one half degree of observations) until 1000 MST 09 January. This scheme then produces similar temperature errors throughout the duration of the simulation. The simulated relative humidity values (Figure 3.46) also capture most of the signal seen in the observations until 1000 MST 09 January. After this time, temperatures begin to exceed those observed, and the relative humidity in turn becomes up to 20% less than witnessed. The wind speeds were modeled with accuracy (Figure 3.47). Like other simulations, the relative humidity visibility scheme captured the fog at the beginning of the first near fog period, but misses the second period entirely (Figure 3.48). The GSD visibility scheme did not represent any fog (Figure 3.49).

Forcing observed albedo values at the beginning of the simulation did not improve our forecast from the control simulation. Warm temperature biases of the same magnitude, about three degrees, remain in the evening hours, leading to erroneously low relative humidity values (Figures 3.51 and 3.52, respectively). With no negative contribution from the wind (Figure 3.53), this affects the relative humidity visibility algorithm (Figure 3.54), but despite the similarity in temperature between this simulation and the control, the results show less fog represented in this simulation. One period of fog was forecast and it was before either period of fog was observed. There is a slightly warmer temperature profile in this run than the control, with the difference in the two runs amounting to less than half

a degree. However, this slight warming allows the temperatures to remain out of the threshold needed to calculate relative humidity with respect to ice instead of water. Therefore, although this run is no drier than the control, it is manifested differently due to how relative humidity is calculated. The GSD visibility algorithm once again fails to show fog for this simulation (Figure 3.55).

#### *3.4.2.4 Radiation Schemes*

Radiation budgets have an influential impact on the formation and evolution of fog. The emission of longwave radiation is closely linked to the formation of daily radiation fog. This process is a contributing factor to the fog seen at the forecast sites for the MATERHORN-Fog campaign. Four sensitivity tests were run to test these influences, two with shortwave parameterizations and two with longwave.

For the shortwave sensitivity experiments, the Goddard shortwave and RRTMG shortwave schemes were chosen to test against the RRTM scheme used in the control simulation. The two schemes showed very similar results, so only the Goddard shortwave scheme is shown (Figures 3.56–3.61). Persistent ridging across the forecast area during the entirety of MATERHORN-Fog allowed for clear skies throughout the period. This means all incoming solar radiation reached the surface, creating little variability in the shortwave radiation. Both schemes show higher temperatures than observations, a staple at this point in the analysis, and relative humidity values too low to account for fog formation. Neither test accurately captured the extent of the first fog period nor forecasted the second.

For the longwave sensitivity experiments, the Goddard was once again chosen, but due to the lack of variability between the Goddard and the RRTMG, the GFDL (Eta) longwave scheme was chosen as the second option. However, this did not make much of a difference as the results do not have startling differences. Therefore, the only scheme represented is the Goddard longwave scheme (Figures 3.62–3.67). Temperature and relative humidity results are consistent with the other experiments, too warm and thusly too dry. Overall, the results do not seem to be affected by testing the shortwave versus longwave radiation schemes.

### 3.4.3 Sensitivity of Fog Simulations to Lead Time

As seen in nearly every simulation, forecast errors were exacerbated after thirty hours of the simulation. The smallest errors introduced in the beginning of the simulation can grow to serious proportions the longer the simulation is run. This is a problem because it occurred in the middle of our fog forecast period, causing most of the simulations to miss the second fog period. In order to examine the effect of lead time on the accurate representation of inversion fog in the numerical simulation, a sensitivity test was run with an initialization time of 0000 UTC 9 January. This simulation was set with the same configuration as the control to see if forecasted variables were significantly improved.

Figures 3.68–3.75 shows the results of the experiment with the control configuration initialized at 0000 UTC 9 January. Immediately obvious is the dramatically better representation of relative humidity (Figure 3.72) compared to the control (Figure 3.20). However, this "better" representation is due to errors in variables that were handled more deftly in the control simulation. A look at the temperature time series (Figure 3.69)

reveals that the errors that were present in the control simulation are not mitigated. There still exists a three-degree warm bias in temperature overnight and errors are expounded late in the simulation (after 0500 MST 10 January). A result of this simulation that was not present in the control is the warm bias in dew point temperatures. Throughout the last forty-two hours of the simulation (2300 MST 08 January – 1700 MST 10 January), there exists at least a one-degree warm bias, with dew points up to five degrees warmer than observed. Unlike the control, when the errors were confined to the overnight hours, this warm bias persists through the daylight hours as well.

This leads to an over prediction of moisture, as evidenced by the absolute humidity graph (Figure 3.71). Therefore, the WRF is picking up on more moisture than is observed, causing a moist bias for this simulation. However, these biases are coincided in a way that makes an accurate representation of relative humidity possible. Although the forecast in Figure 3.72 is the best produced by this sensitivity study, it is only due a miscalculation of other surface variables. Using this configuration, two distinct periods of fog are captured using the relative humidity visibility algorithm, the first from 2300 MST 08 January to 0800 MST 09 January, and the second from 1700 MST 09 January to 0900 MST 10 January. Both periods were not without their false positives at the beginning of each forecast period (Figure 3.74), but expansive enough to represent portions of the observed fog. Using this configuration, we are still unable to produce an expansive enough forecast to capture the observations. The GSD visibility algorithm only produced one period of forecasted fog in the second observed fog period.

## 3.5 Summary and Discussion

The WRF model faced a challenge accurately predicting fog conditions at the surface. Since fog is a "threshold phenomena," the accuracy of its forecast is dependent on the accurate prediction of boundary layer temperature, dew point, and wind fields. In this study, the WRF model struggled to produce fog conditions using algorithms based on both relative humidity and hydrometeor concentration critera.

Most of the errors are confined to the boundary layer. In most experiments, simulated temperatures were too warm when attempting to reproduce the fog present in MATERHORN-Fog IOPs 1 and 2, especially in the overnight hours. Dew point temperatures were forecast much more proficiently than temperatures, leading to accurate representations of absolute moisture in the model. This implies that errors seen in relative humidity values were nearly entirely dependent on errors in forecast temperature. The most accurate surface variable forecast was surface wind speed, eliminating errors due to excessive mixing or advection at the surface.

An investigation into the errors caused by incorrect representation of radiation at the surface was conducted. The results are shown in Figures 3.76–3.79, for the control, Goddard shortwave, Goddard longwave, and control with forced initial albedo. Figure 3.76 shows that all experiments are capturing correct downward shortwave flux except for the Goddard longwave parameterization (green) which overestimates this value. Downward longwave radiation shows much more spread between the simulations, especially prevalent after 0500 MST 09 January (Figure 3.77). However, none have more than a 20 $W/m^2$ prolonged deviation from observations. Upward shortwave radiation (Figure 3.78) is a different story, as all experiments overestimate observed values by at

least 20 W/m$^2$, with the Goddard longwave scheme showing most error with values double of what was observed. These errors are also seen in upward longwave radiation, but with underestimation (Figure 3.79). Most errors show a -40 W/m$^2$ bias overnight, a major contribution to the warm bias in temperatures seen in these hours in nearly every experiment.

The lead time experiment shows that better prediction of observed fog is sensitive to when a run is initialized. This is due to introduction of error early in a forecast that can be exacerbated as the run progresses. The first set of experiments were initialized at 0500 MST, right before sunrise. As seen in every experiment, the near-surface variables were handled with much more proficiency in the daylight hours, allowing less error to be introduced early in the model simulation. However, when initialized at 1700 MST, near nightfall, more error was introduced early because of the WRF's inability to accurately capture the emission of longwave radiation from the surface. Therefore, more error was introduced early in the forecast, causing for a bigger deviation from the observations. It is important to consider when your model is initialized based on past performance so that you may mitigate the introduction of early-simulation error.

The simulations that produced too much fog, although incorrect, are useful. Fog poses a danger to commuters of all types: drivers, bikers, and jet passengers. Therefore, a forecast of fog can aid National Weather Service forecasters in the issuance of fog advisories. This information can be invaluable to the citizens of the northern Utah valleys and can potentially lessen the risk of dangerous travel during these foggy periods. It can also aid in the rescheduling of flights ahead of time so that commuters are not delayed and airports are not at a risk of lost revenue due to last-minute rescheduling. However, as

indicated in this chapter, accurate prediction of fog depends on model configurations, physical parameterizations, and forecast lead time (implying a sensitivity to initial conditions). Thus, it is still an area that needs further exploration in numerical weather prediction.

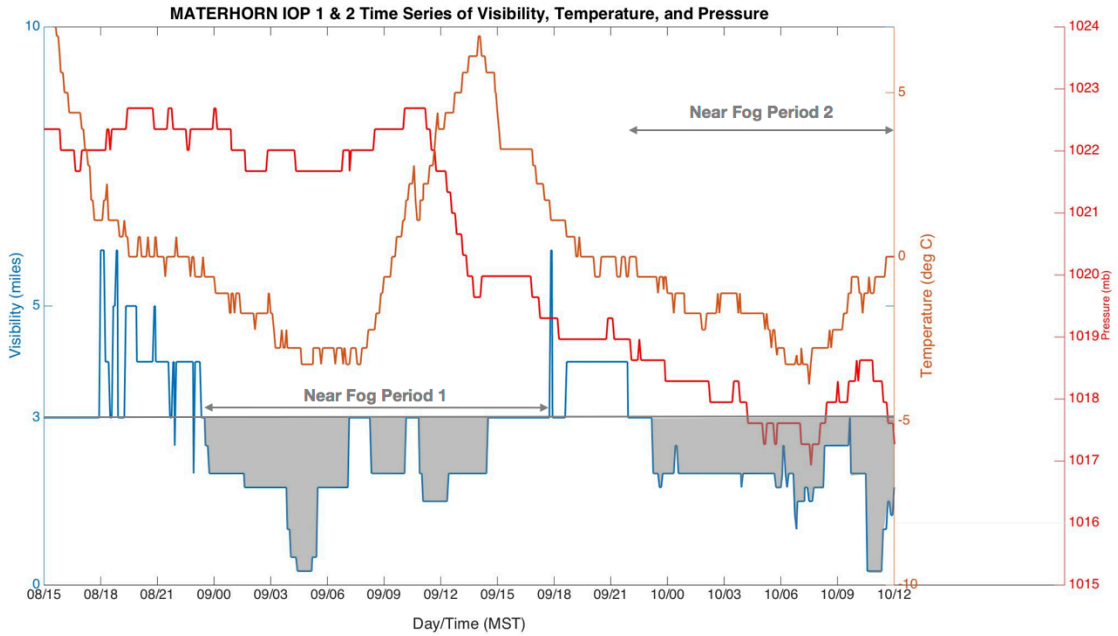


Figure 3.1. A time series of visibility (blue), temperature (orange), and pressure (red) for Salt Lake City for the entirety of MATERHORN-Fog IOP 1 and 2 (1500 MST January 8 to 1200 MST 9 January, and 1400 MST January 9 to 1200 MST January 10, respectively). Two periods of near fog are indicated with gray arrows and shading, Near Fog Period 1 from 0000 MST to 1800 MST January 9 and Near Fog Period 2 from 2200 MST January 9 to 1200 MST January 10.

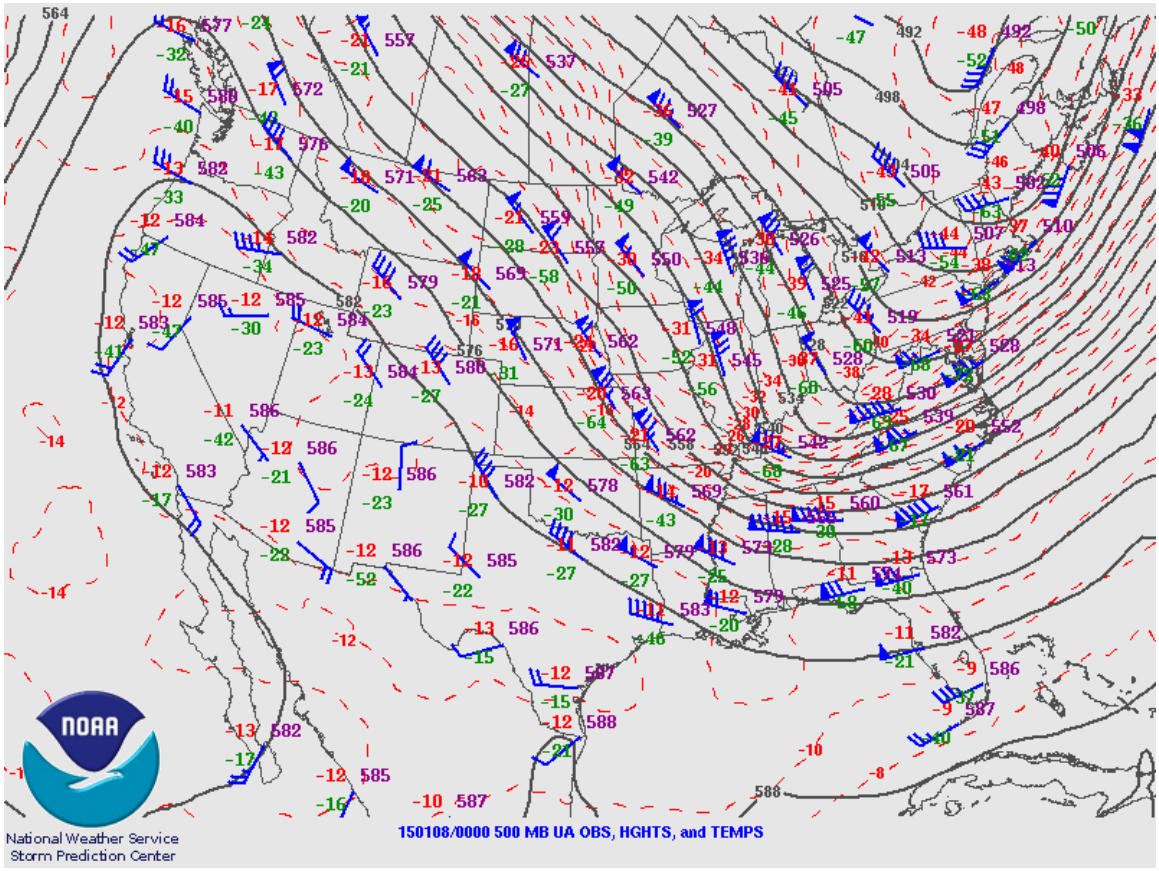


Figure 3.2. NOAA/NWS SPC 500 hPa map from 0000 UTC 08 January 2015. Geopotential height contours (solid lines), isotherms (red dashed lines), and wind barbs (speed in knots) contoured.

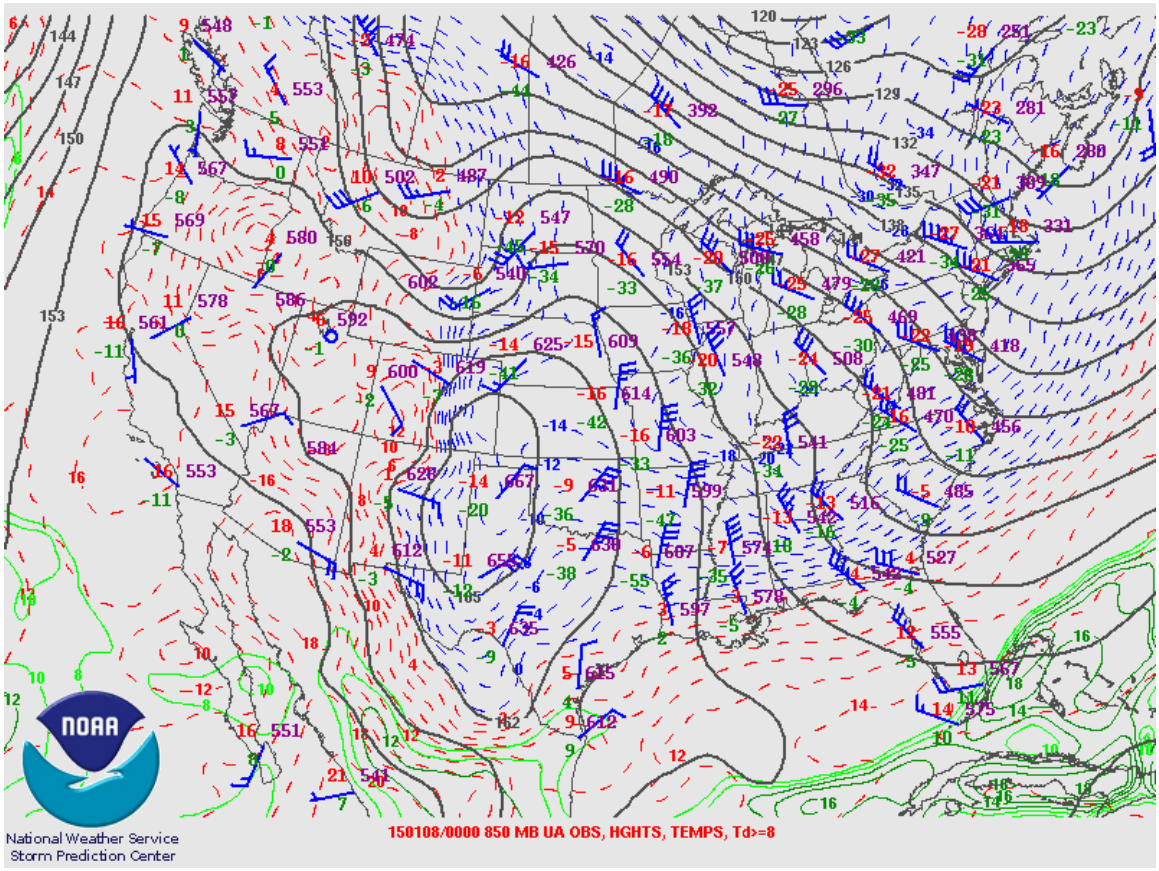


Figure 3.3. NOAA/NWS SPC 850 hPa map from 0000 UTC 08 January 2015. Geopotential height contours (solid lines), isotherms (red and blue dashed lines), wind barbs (speed in knots), and isodrosotherms (solid green lines) are contoured.

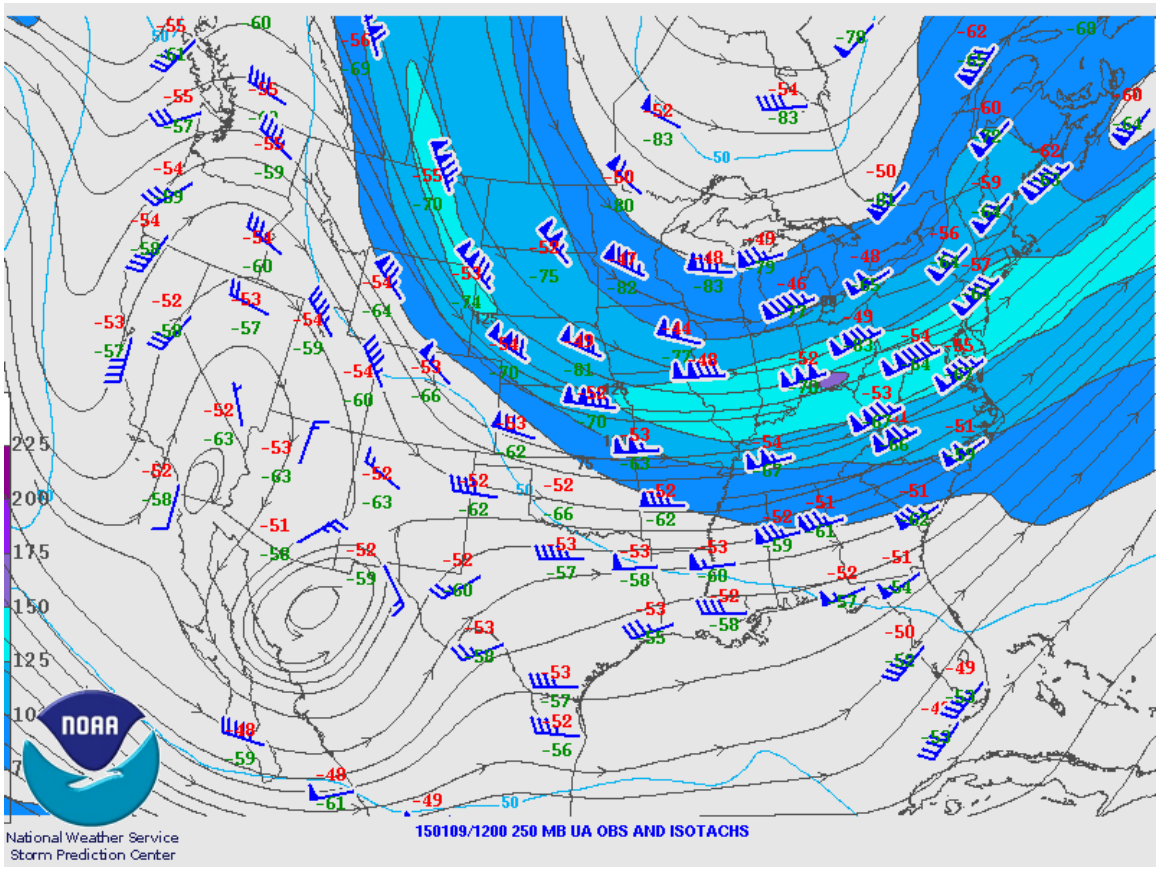


Figure 3.4. NOAA/NWS SPC 250 hPa upper air map from 1200 UTC 9 January 2015. Geopotential height contours (solid lines), streamlines (gray solid lines with arrows), isotherms (red dotted lines), wind barbs (speed in knots), and isotachs (filled contours) are analyzed.

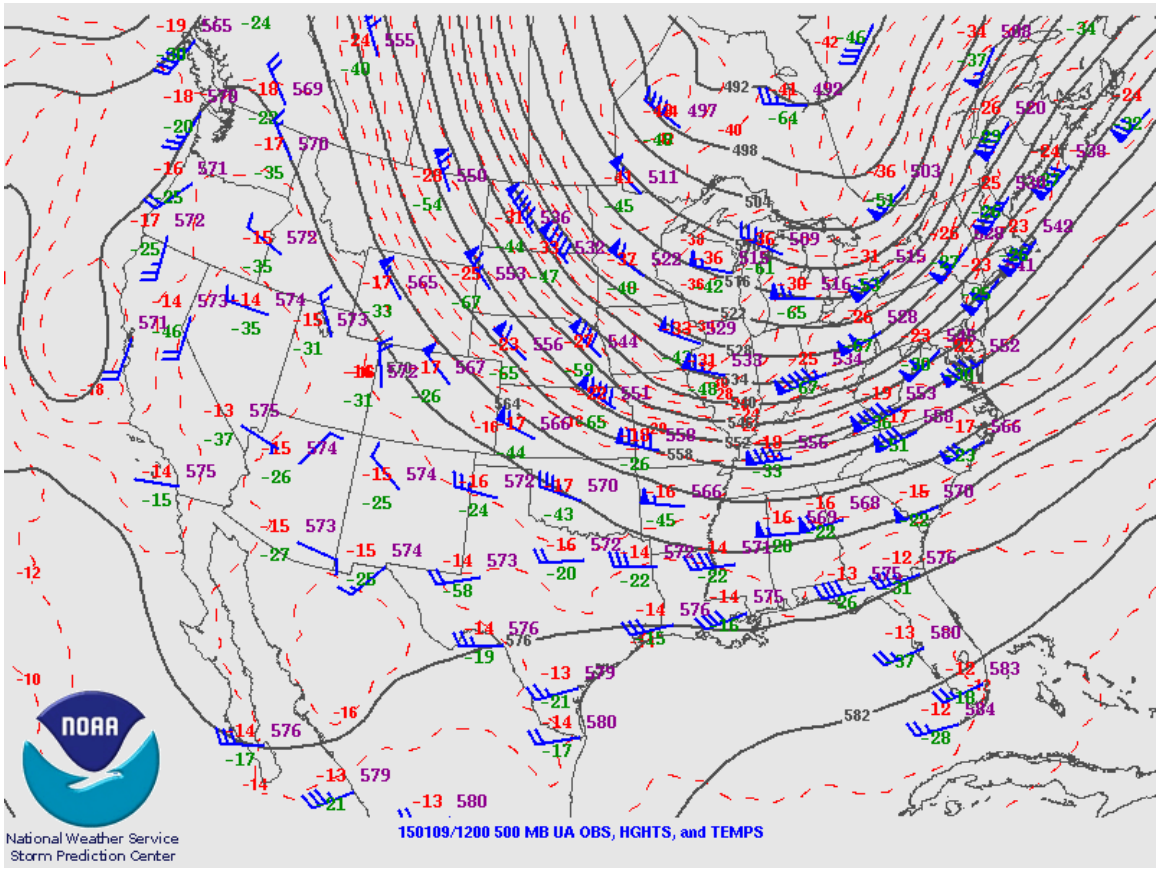


Figure 3.5. NOAA/NWS SPC 500 hPa upper air map from 1200 UTC 9 January 2015. Geopotential height contours (solid lines), streamlines (gray solid lines with arrows), isotherms (red dotted lines), and wind barbs (speed in knots) are analyzed.

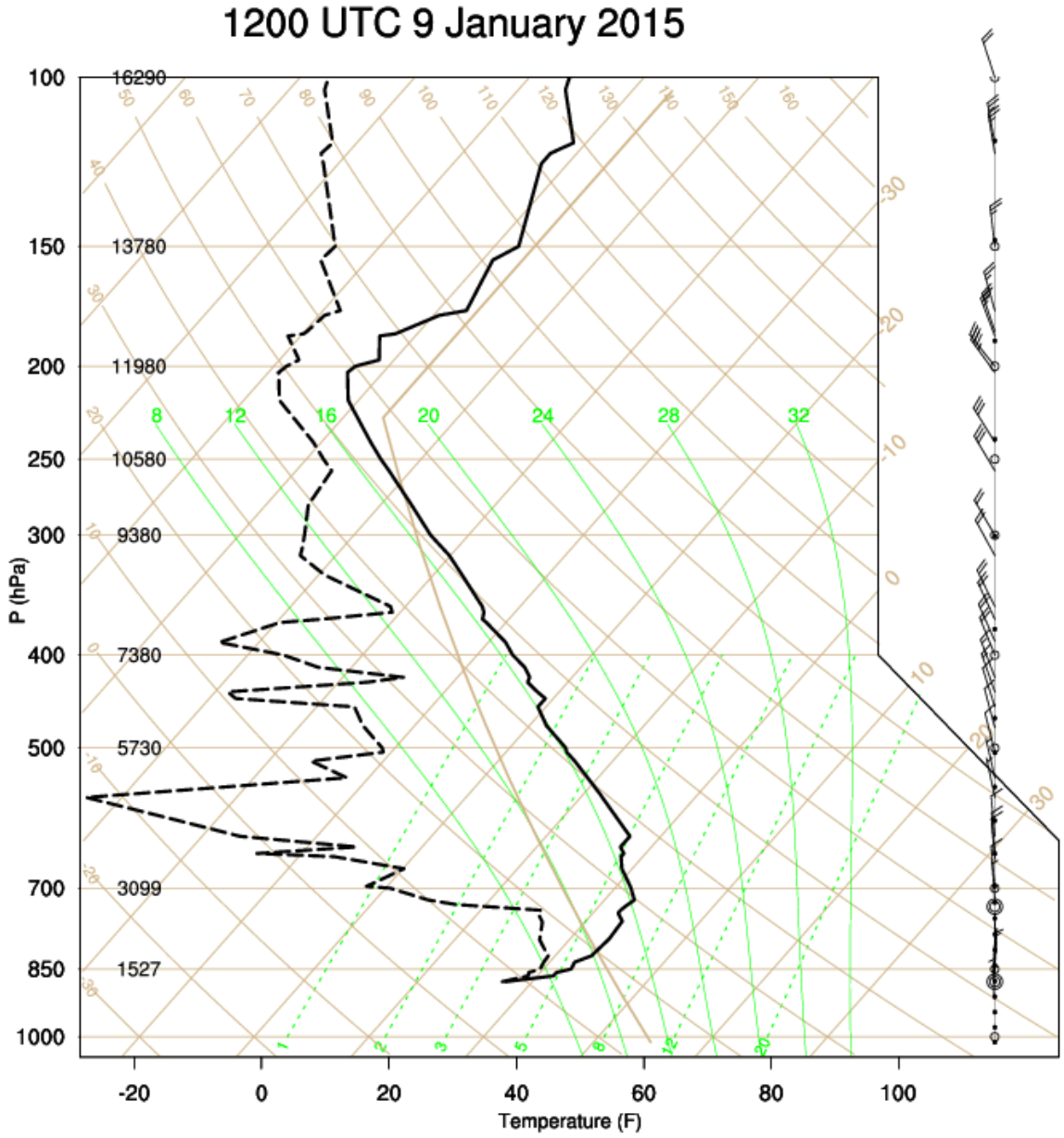


Figure 3.6. Sounding from Salt Lake City International Airport (KSLC) from 1200 UTC 9 January 2015. Temperature (F) along x-axis and pressure (hPa) along y-axis. Temperature (C) (straight beige lines), dry adiabats (curved beige lines), moist adiabats (curved green lines), saturation mixing ratio lines (dotted straight green lines), and wind barbs (speed in knots) analyzed. Temperature for this sounding is the solid black line, and dew point temperature for this sounding is the dotted black line.

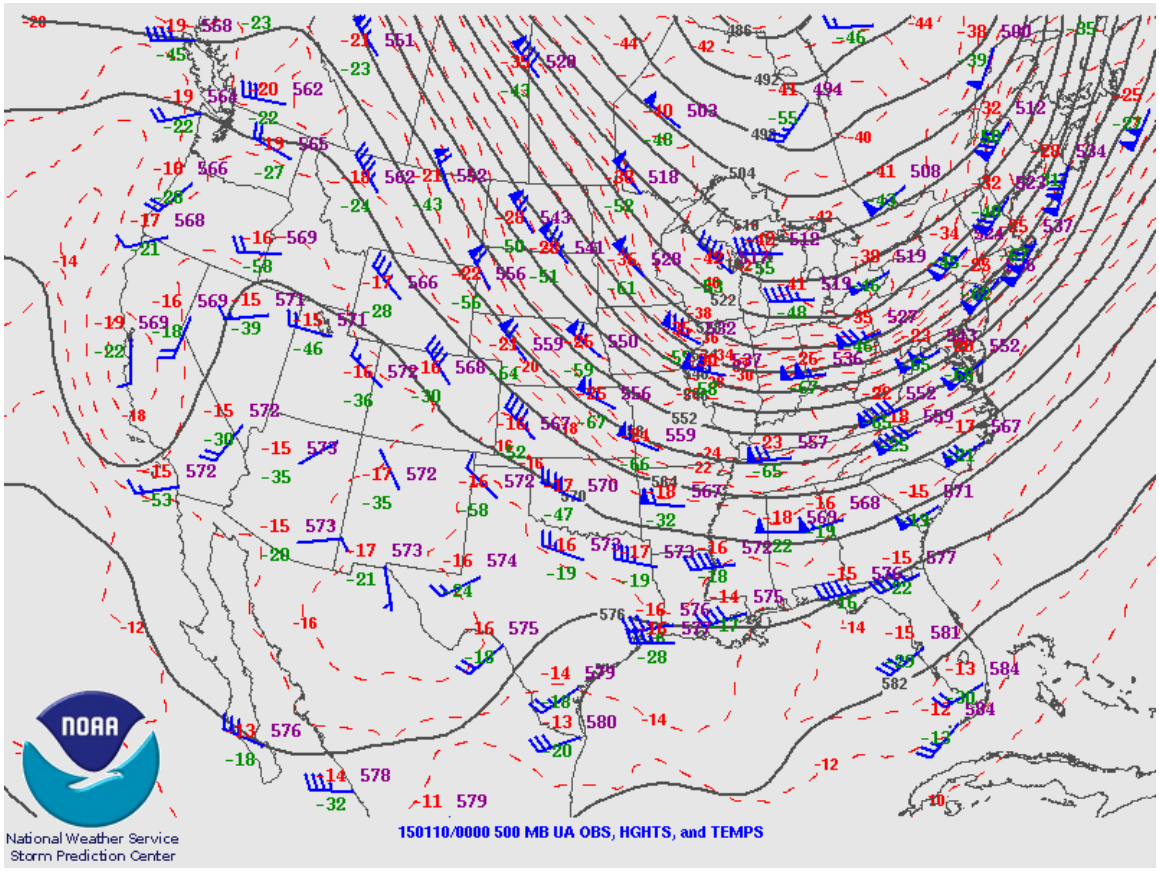


Figure 3.7. NOAA/NWS SPC 500 hPa map valid at 0000 UTC 10 January 2015. Geopotential height contours (solid lines), isotherms (red dotted lines), and wind barbs (speed in knots) are analyzed.

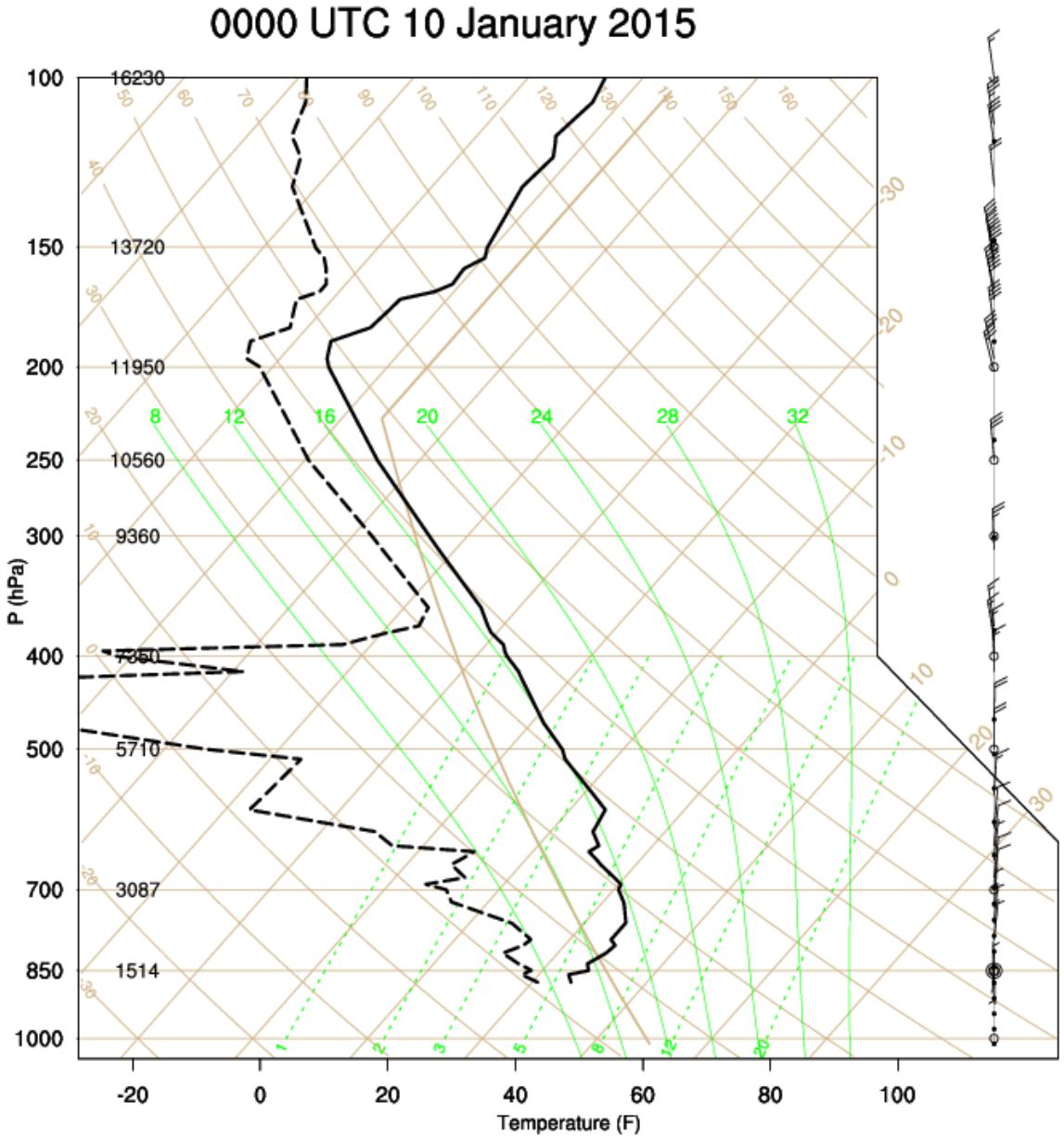


Figure 3.8. Sounding from Salt Lake City International Airport (KSLC) from 0000 UTC 10 January 2015. Temperature (F) along x-axis and pressure (hPa) along y-axis. Temperature (C) (straight beige lines), dry adiabats (curved beige lines), moist adiabats (curved green lines), saturation mixing ratio lines (dotted straight green lines), and wind barbs (speed in knots) analyzed. Temperature for this sounding is the solid black line, and dew point temperature for this sounding is the dotted black line

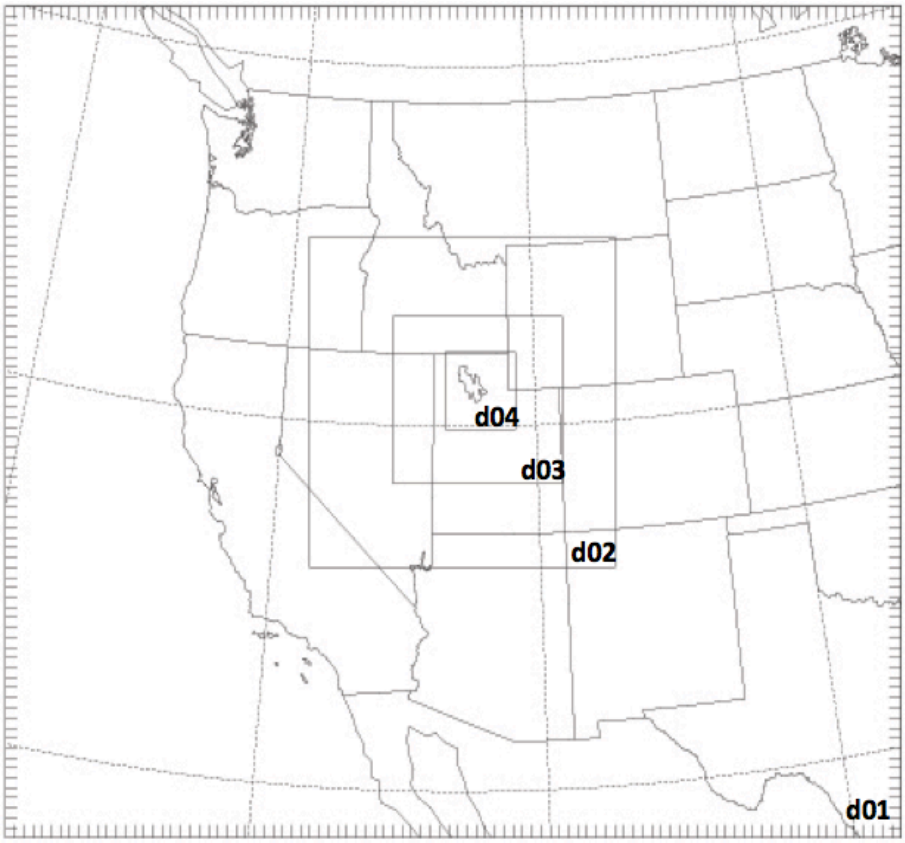


Figure 3.9. Locations of model domains. The resolutions for d01, d02, d03, and d04 are 30 km, 10 km, 3.33 km, and 1.11 km, respectively.

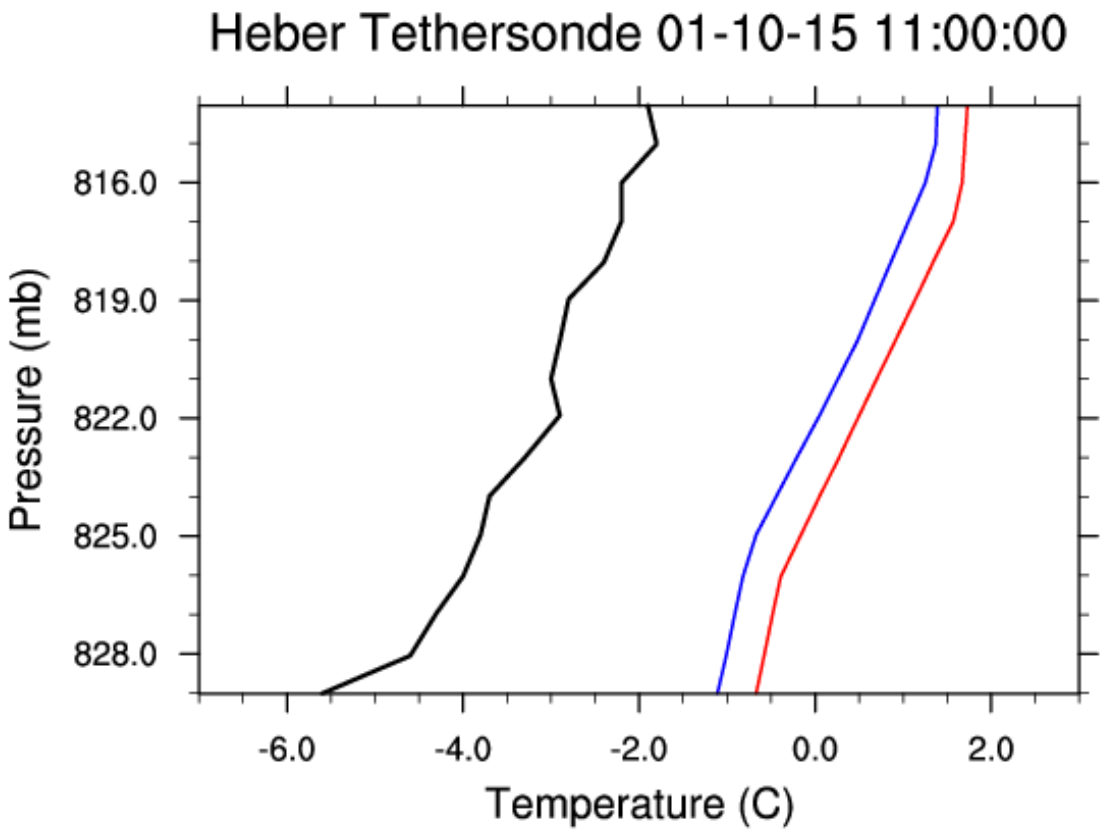


Figure 3.10. Comparison of tethersonde balloon profiles taken during MATERHORN-Fog IOP 2 (black line) of near surface temperature with model solution from 41 vertical levels (red line) and 60 levels (blue line) at Heber site at 1100 UTC 10 January.

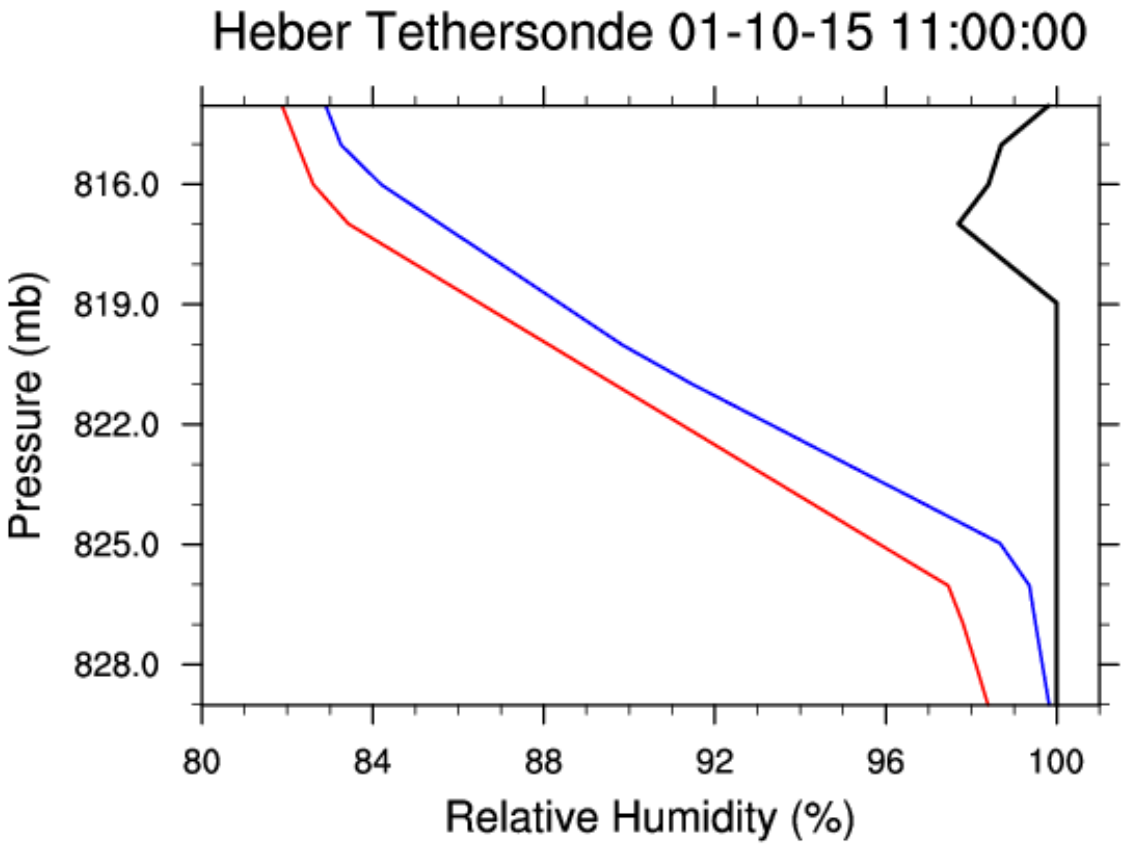


Figure 3.11. Comparison of tethersonde balloon profiles taken during MATERHORN-Fog IOP 2 (black line) of near surface relative humidity with model solution from 41 vertical levels (red line) and 60 levels (blue line) at Heber site at 1100 UTC 10 January.

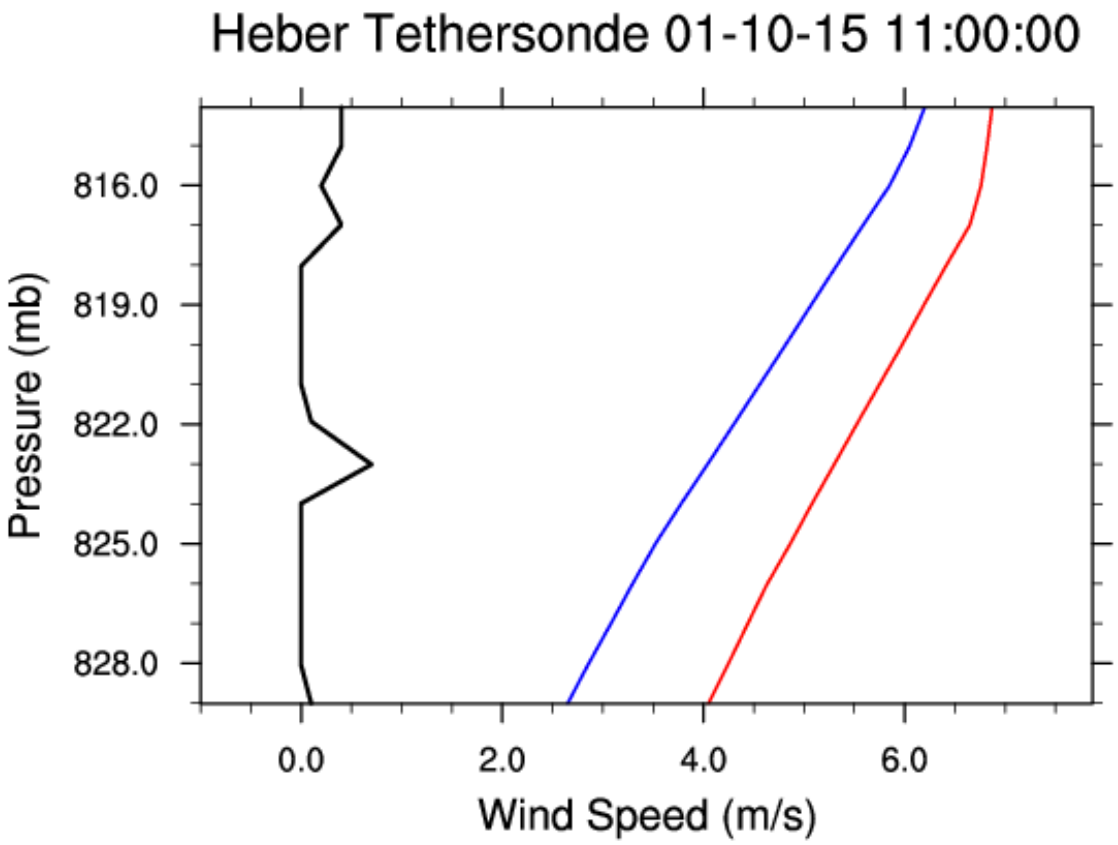


Figure 3.12. Comparison of tethersonde balloon profiles taken during MATERHORN-Fog IOP 2 (black line) of near surface wind speed with model solution from 41 vertical levels (red line) and 60 levels (blue line) at Heber site at 1100 UTC 10 January.

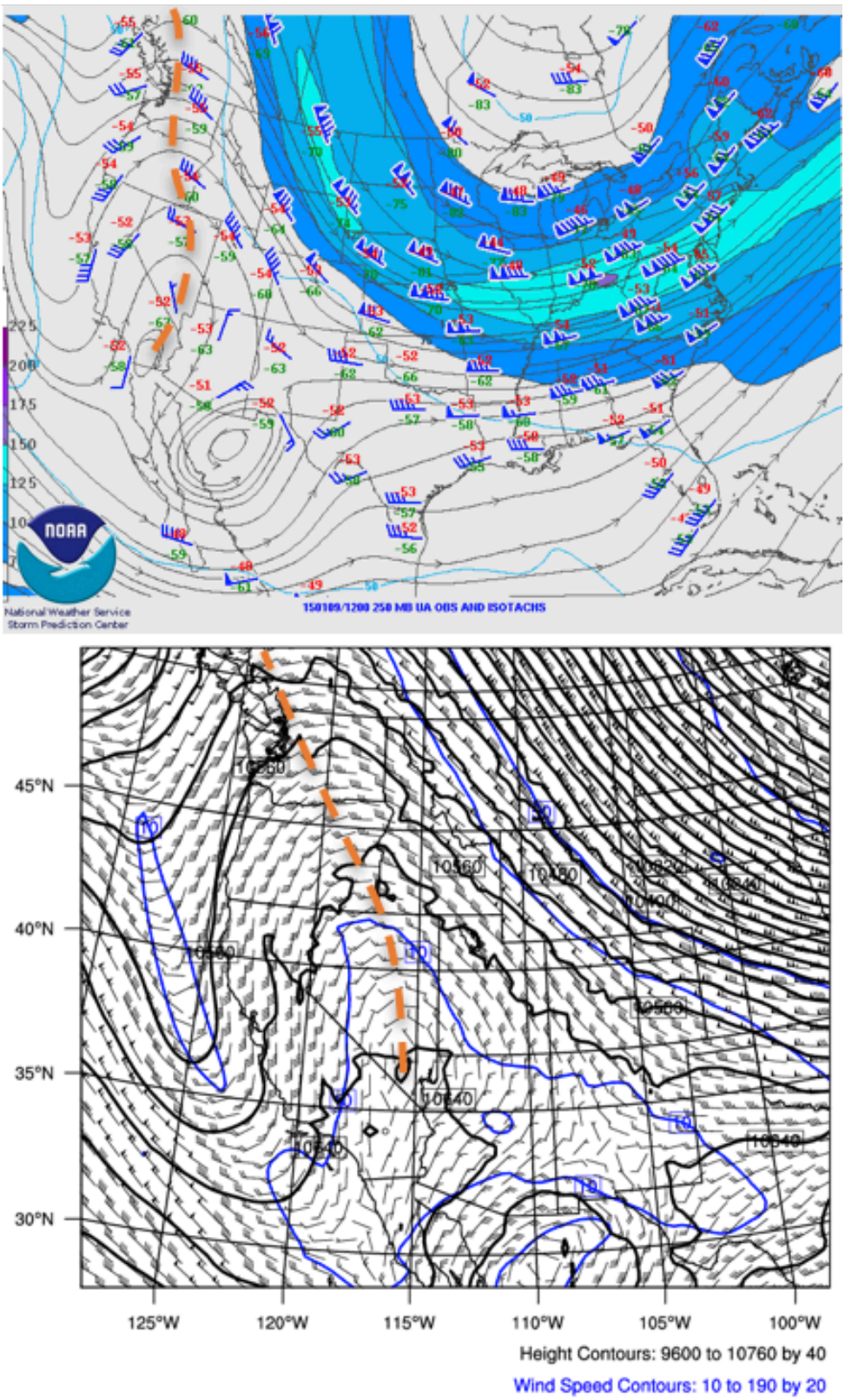


Figure 3.13. 250 hPa comparison of synoptic map (top) and associated WRF-generated solutions (bottom) from the control experiment initialized with a twenty-six-hour lead time for 1200 UTC 9 January 2015.

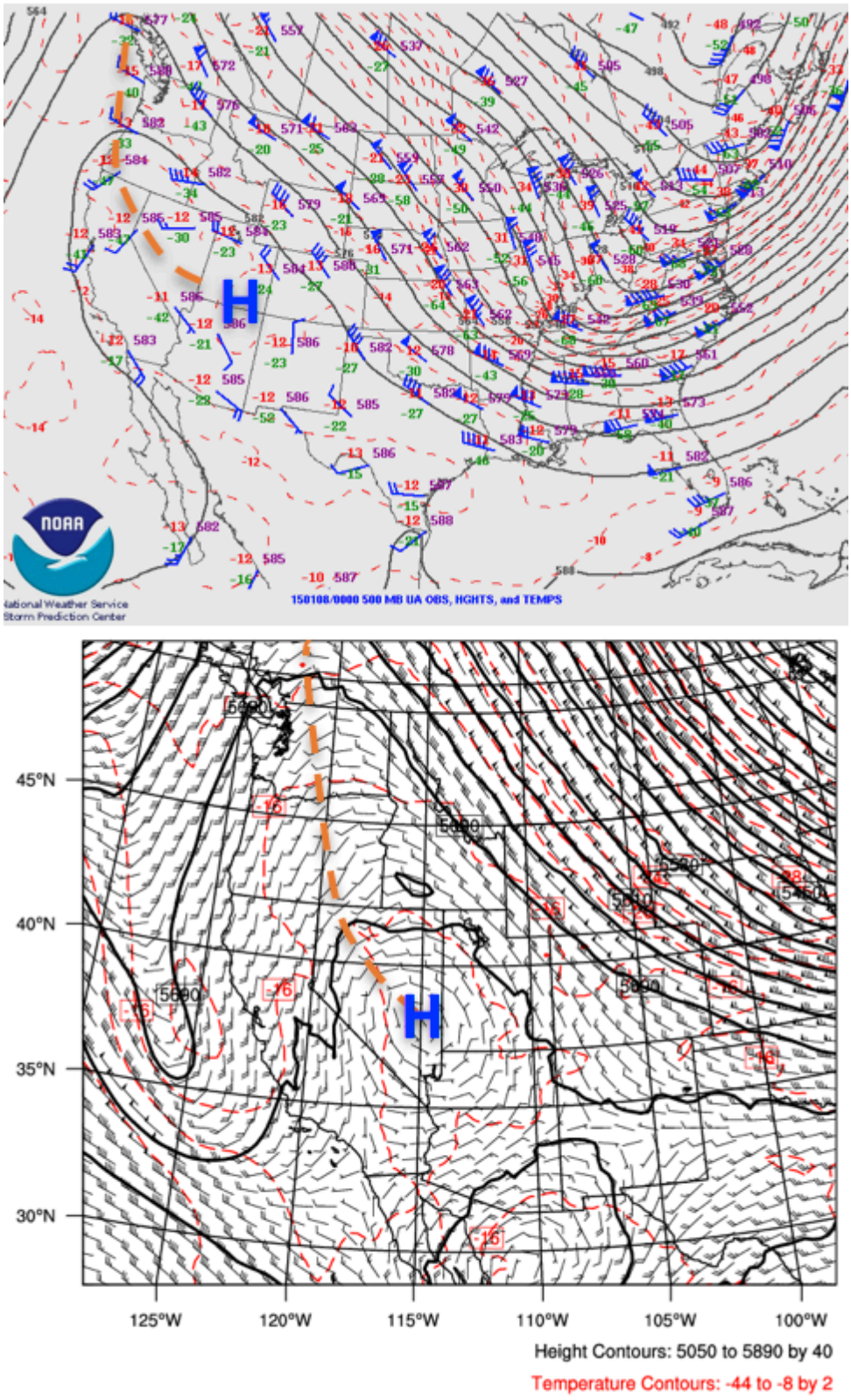


Figure 3.14. 500 hPa comparison of synoptic map (top) and associated WRF-generated solutions (bottom) from the control experiment initialized with a twenty-six-hour lead time for 1200 UTC 9 January 2015.

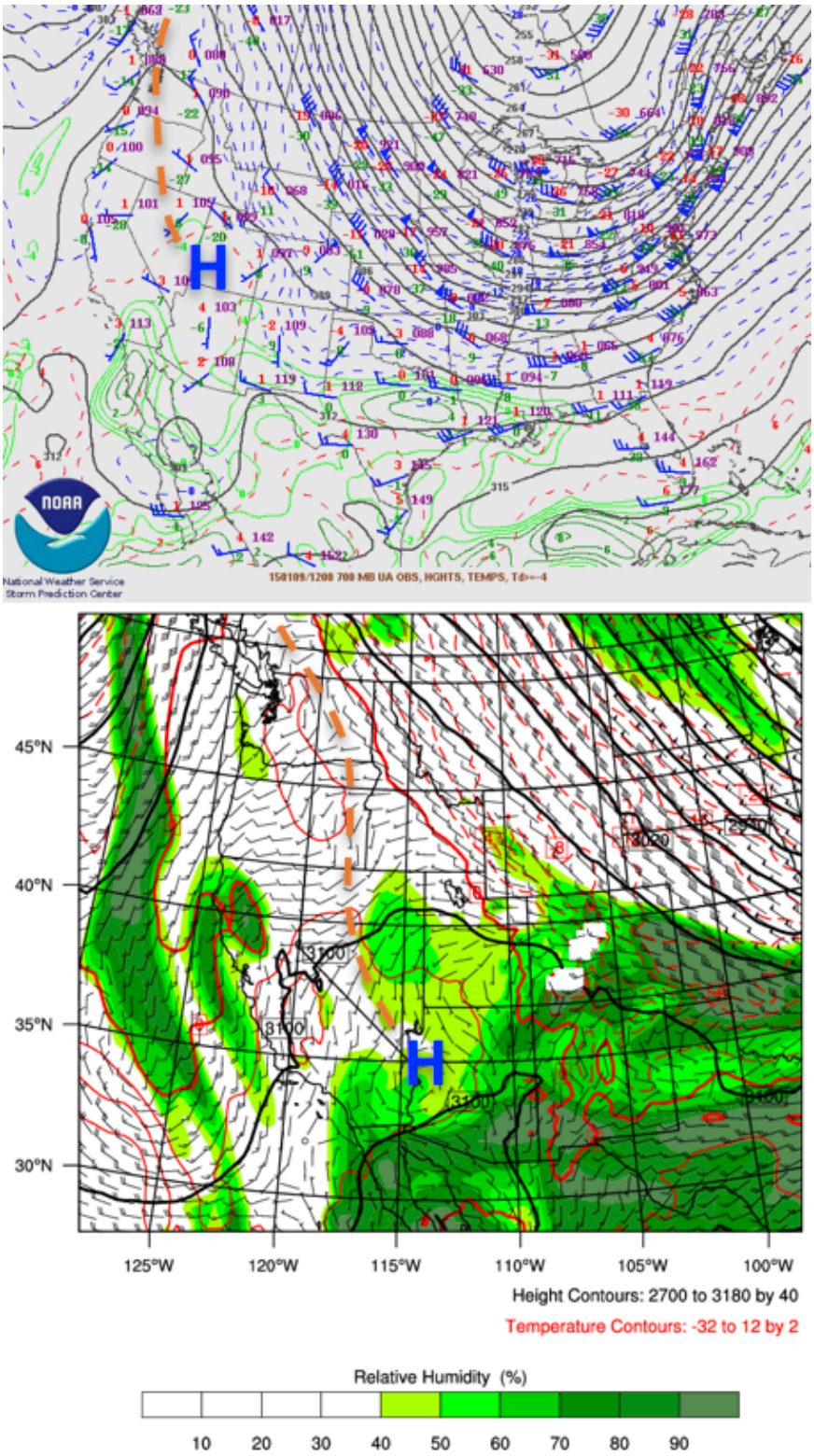


Figure 3.15. 700 hPa comparison of synoptic map (top) and associated WRF-generated solutions (bottom) from the control experiment initialized with a twenty-six-hour lead time for 1200 UTC 9 January 2015.

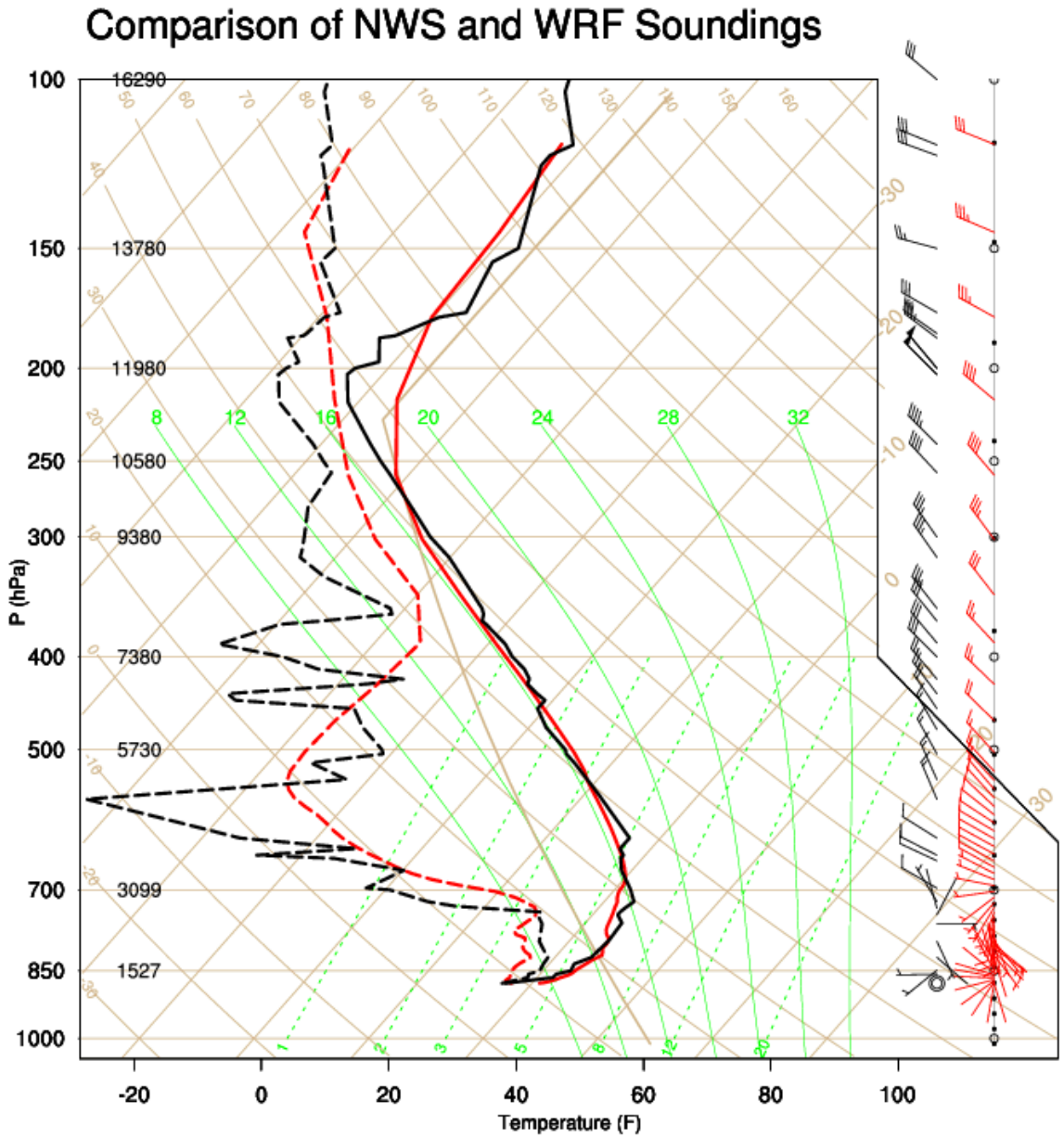


Figure 3.16. Sounding comparison at Salt Lake City International Airport (KSLC) from 1200 UTC 09 January 2015 between observations and control model solution. Temperature (F) along x-axis and pressure (hPa) along y-axis. Temperature (C) (straight beige lines), dry adiabats (curved beige lines), moist adiabats (curved green lines), saturation mixing ratio lines (dotted straight green lines), and wind barbs (speed in knots) analyzed. Observed temperature for this sounding represented by the solid black line, and observed dew point temperature for this sounding represented the dotted black line. Modeled temperature for this sounding represented by the solid red line, and modeled dew point temperature for this sounding represented by the dotted red line.

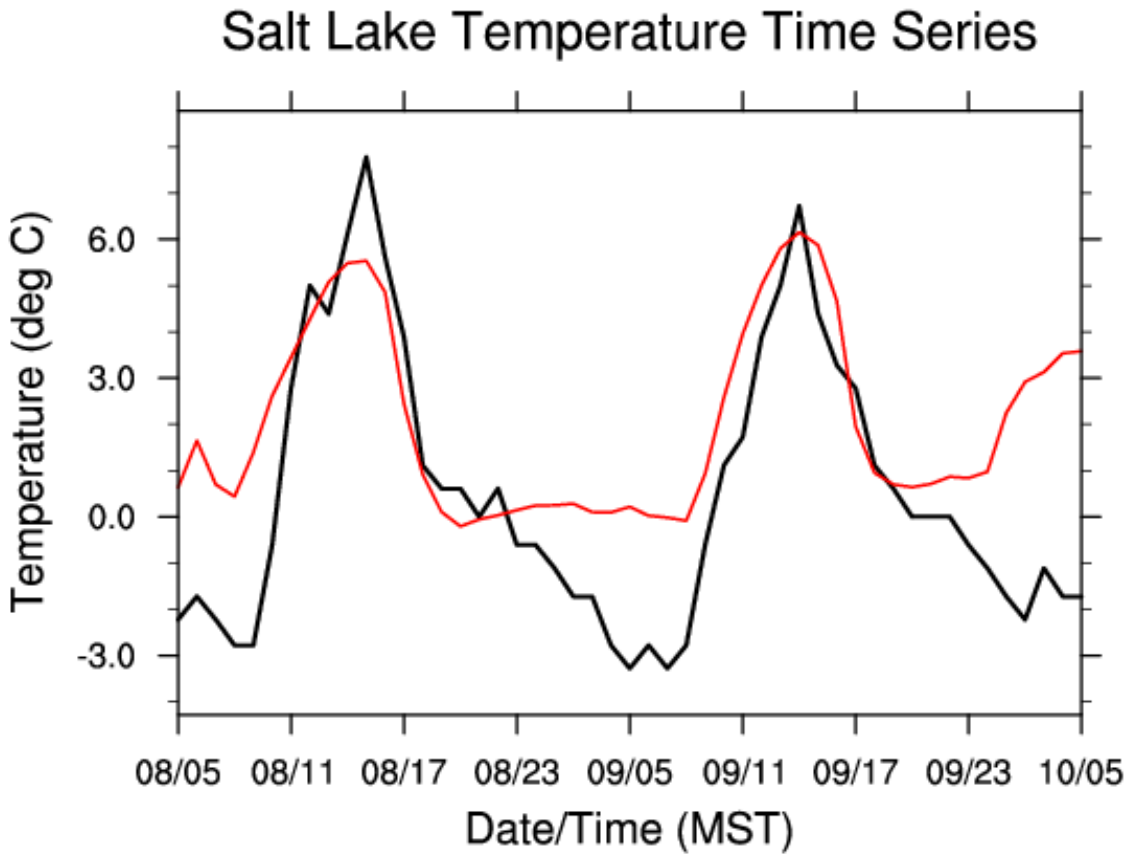


Figure 3.17. Temperature time series comparison for duration of control model simulation. Observed temperature in black, model solution in red.

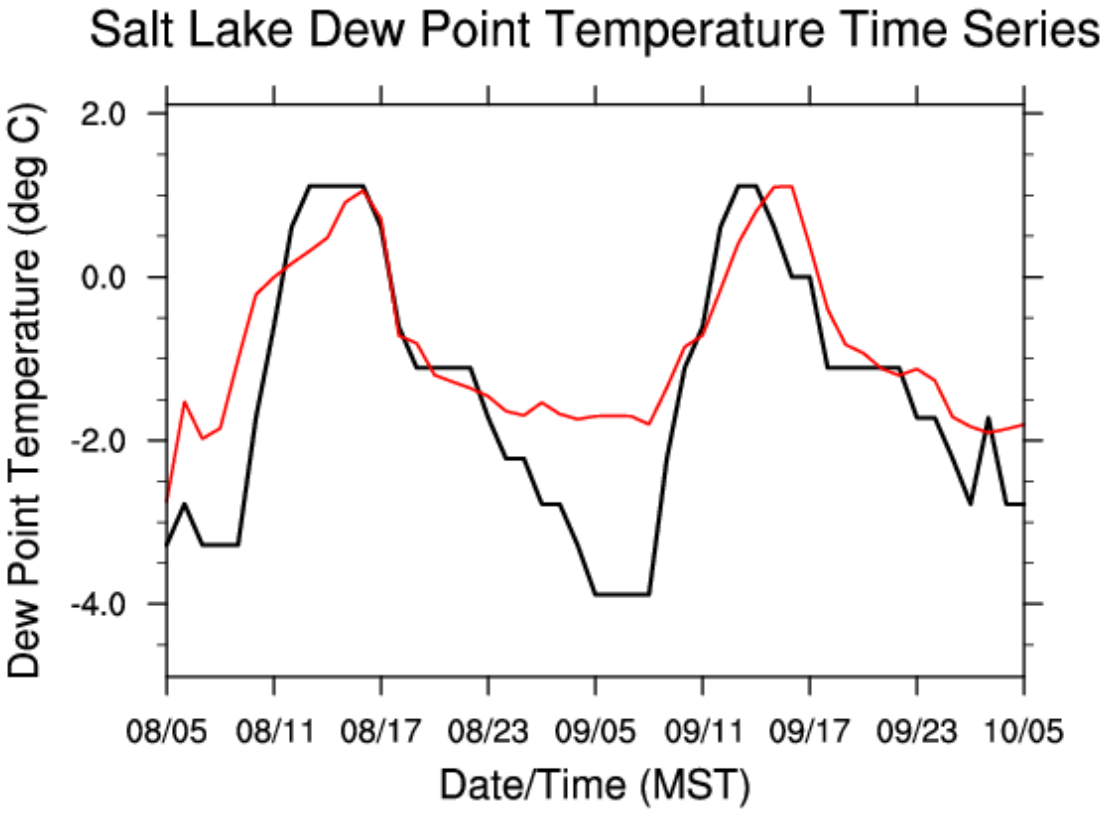


Figure 3.18. Dew point temperature time series comparison for duration of control model simulation. Observed dew point temperature in black, model solution in red.

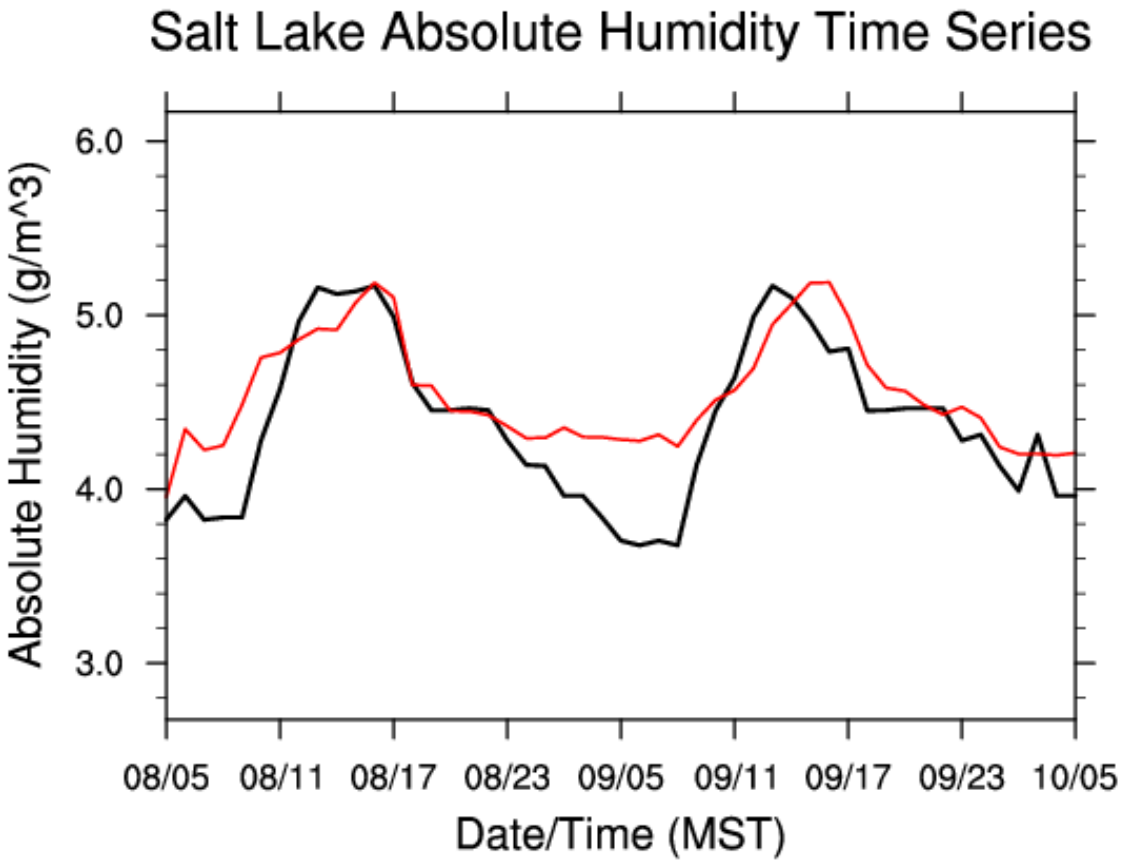


Figure 3.19. Absolute humidity time series comparison for duration of control model simulation. Observed absolute humidity in black, model solution in red.

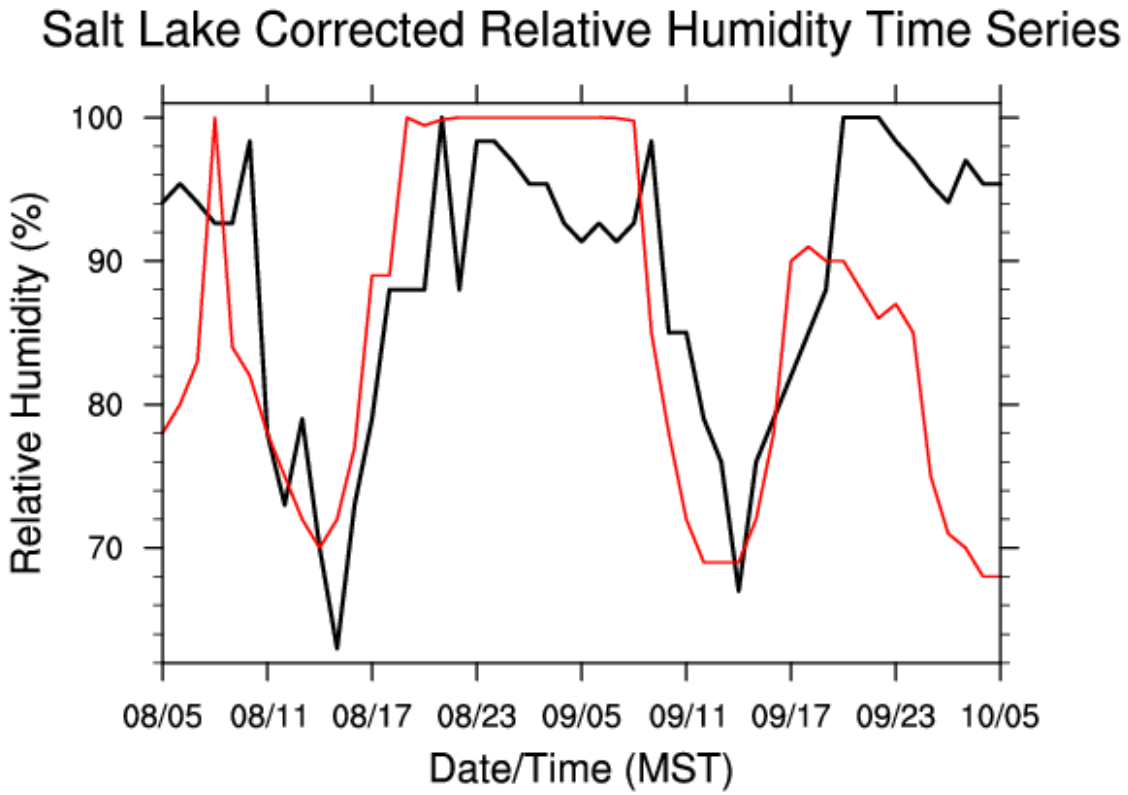


Figure 3.20. Corrected relative humidity time series comparison for duration of control model simulation. Observed corrected relative humidity in black, model solution in red.

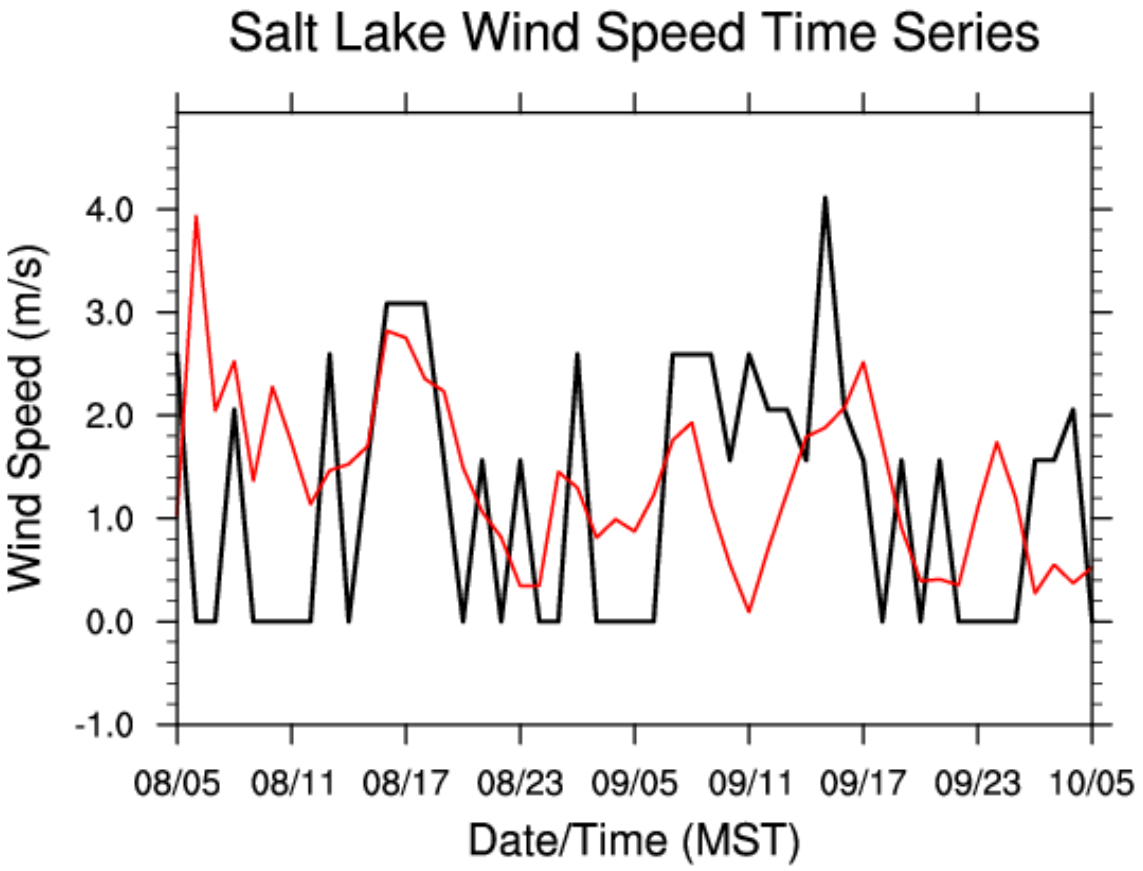


Figure 3.21. Wind speed time series comparison for duration of control model simulation. Observed corrected relative humidity in black, model solution in red.

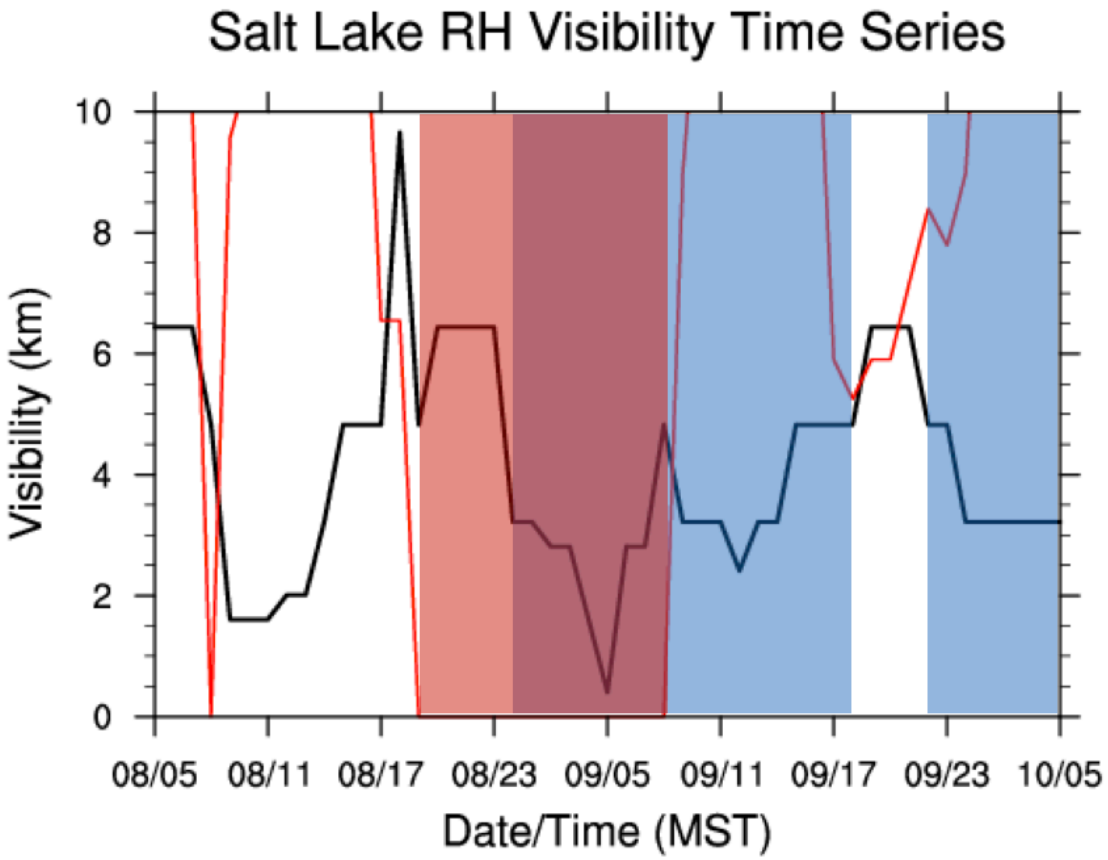


Figure 3.22. Visibility time series comparison calculated with respect to corrected relative humidity for control simulation. Observed visibility is in black, model solution in red. Blue shading represents observed fog, and red shading represents fog in model solution.

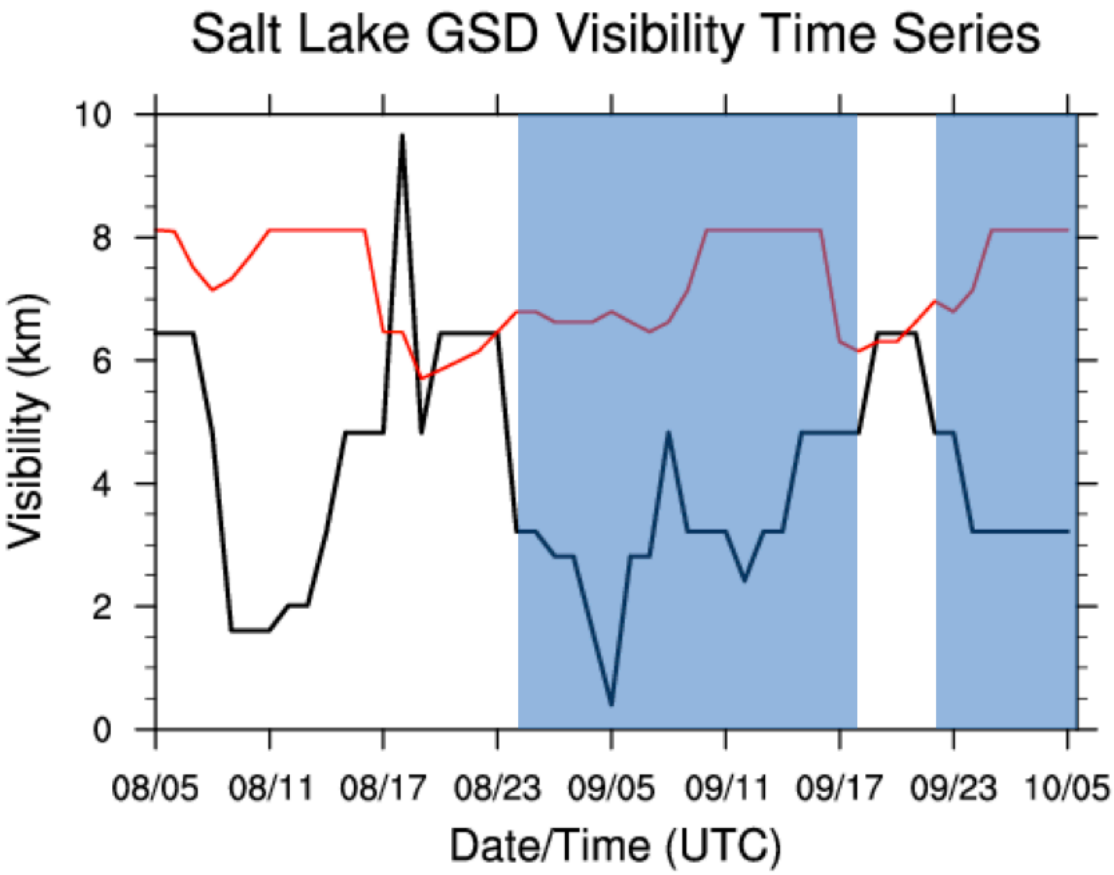


Figure 3.23. Visibility time series comparison calculated with respect to GSD visibility algorithm for control simulation. Observed visibility is in black, model solution in red. Blue shading represents observed fog, and red shading represents fog in model solution.

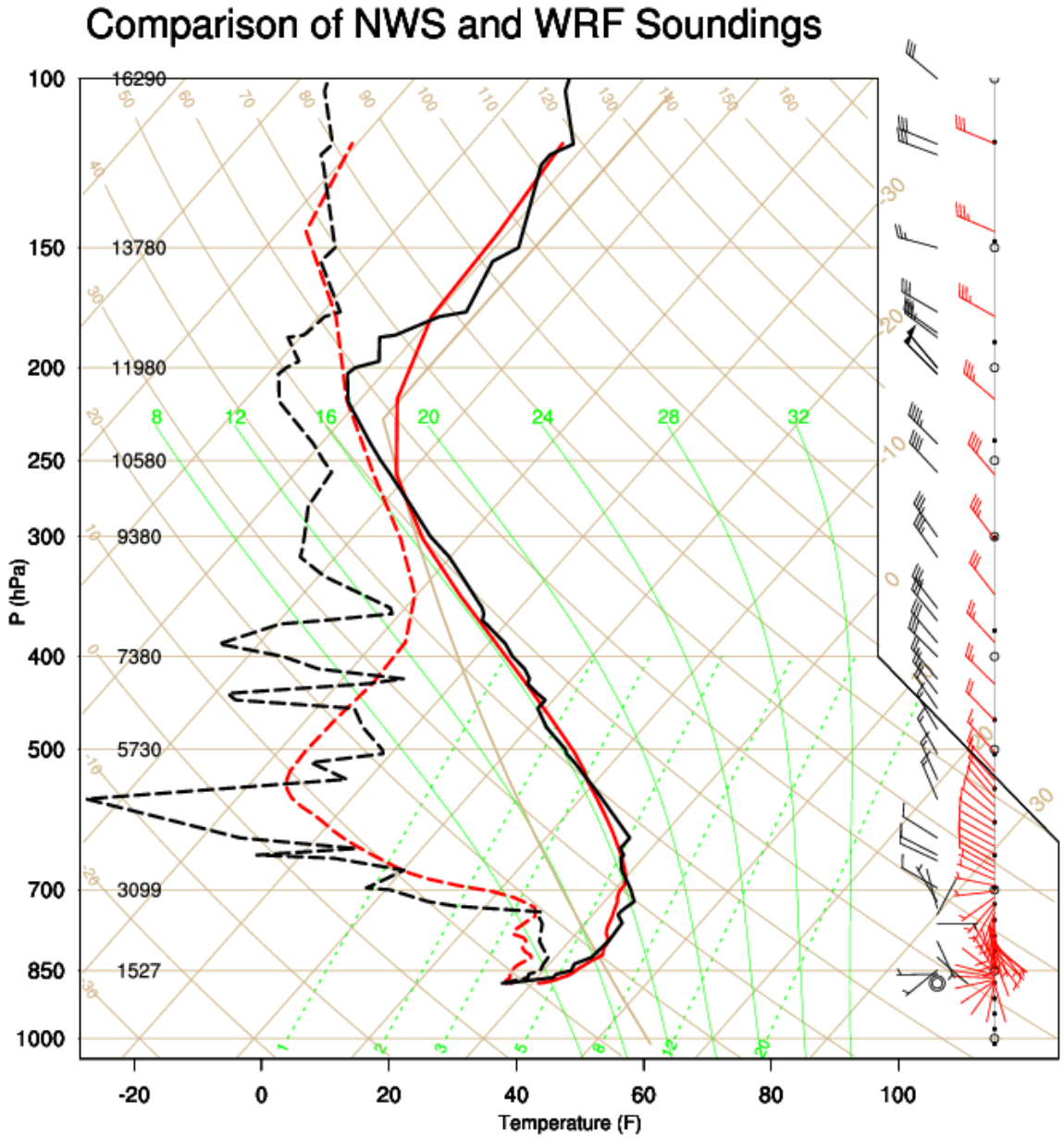


Figure 3.24. Sounding comparison at Salt Lake City International Airport (KSLC) from 1200 UTC 09 January 2015 between observations and sensitivity test run with Thompson Aerosol Aware cloud microphysics. Temperature (F) along x-axis and pressure (hPa) along y-axis. Temperature (C) (straight beige lines), dry adiabats (curved beige lines), moist adiabats (curved green lines), saturation mixing ratio lines (dotted straight green lines), and wind barbs (speed in knots) analyzed. Observed temperature for this sounding represented by the solid black line, and observed dew point temperature for this sounding represented the dotted black line. Modeled temperature for this sounding represented by the solid red line, and modeled dew point temperature for this sounding represented by the dotted red line.

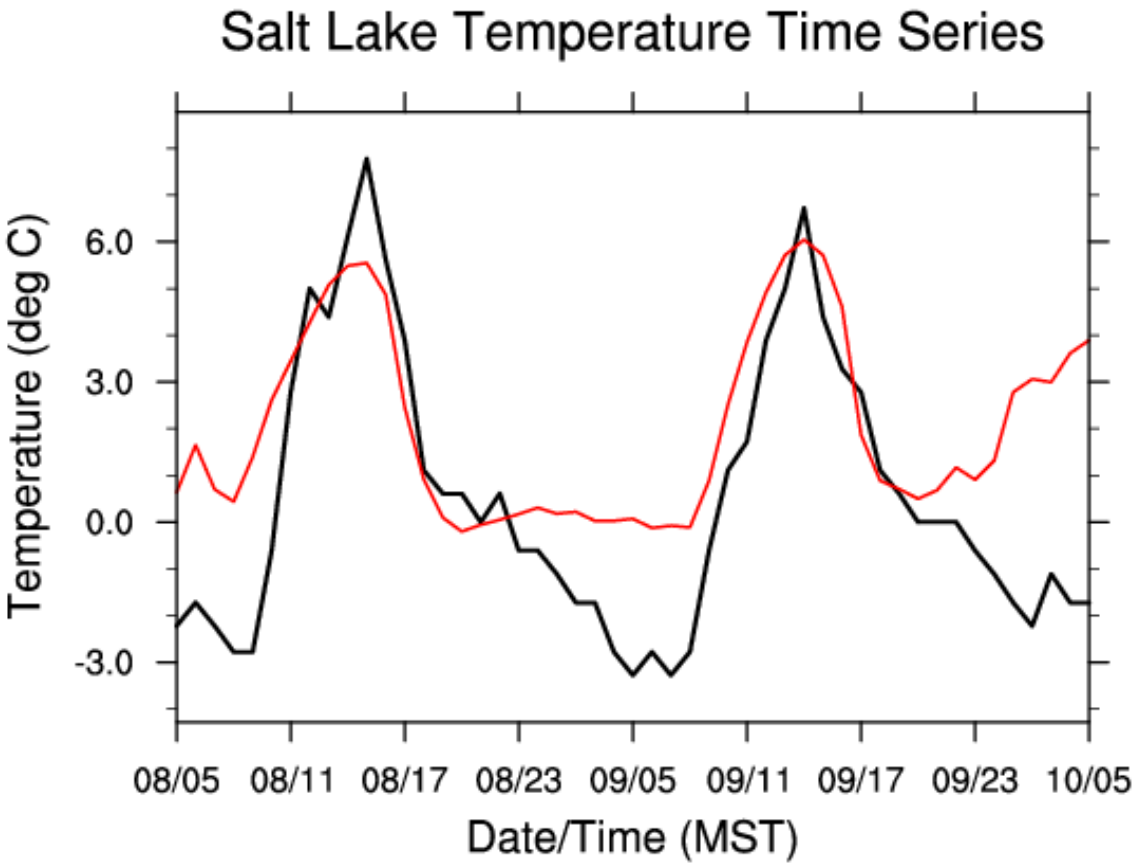


Figure 3.25. Temperature time series comparison for duration of Thompson Aerosol Aware model simulation. Observed temperature in black, model solution in red.

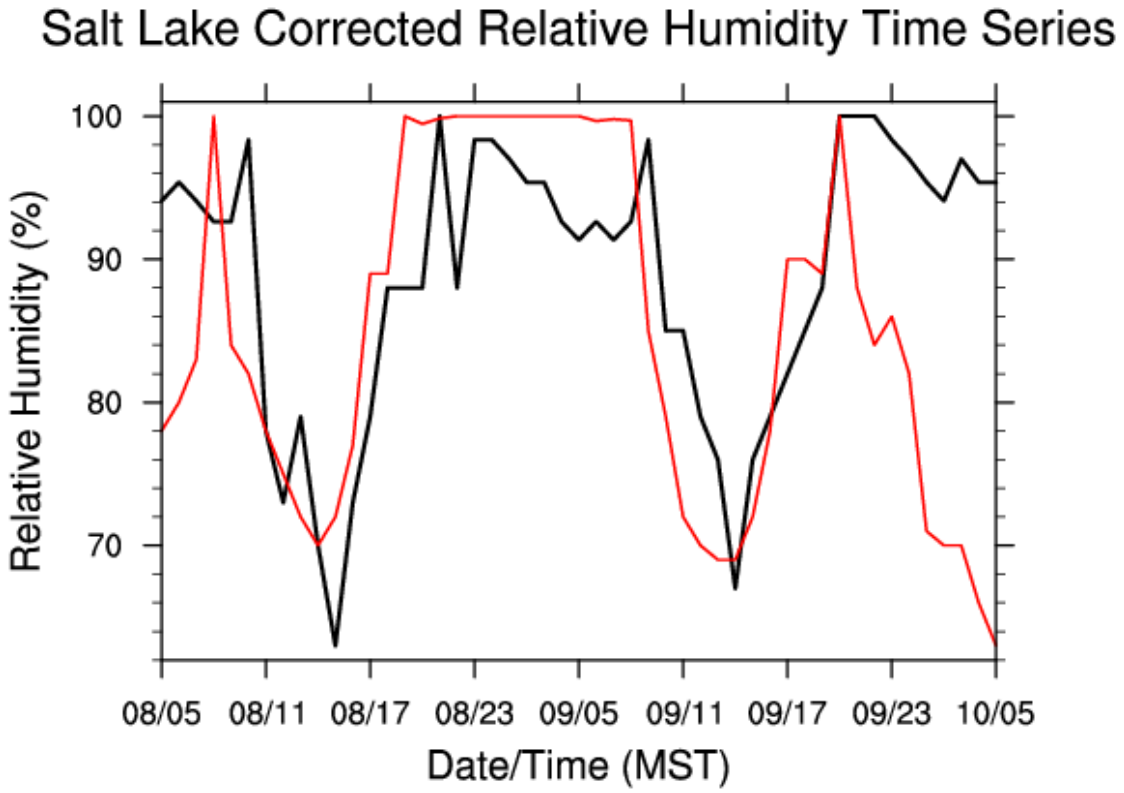


Figure 3.26. Corrected relative humidity time series comparison for duration of Thompson Aerosol Aware model simulation. Observed corrected relative humidity in black, model solution in red.

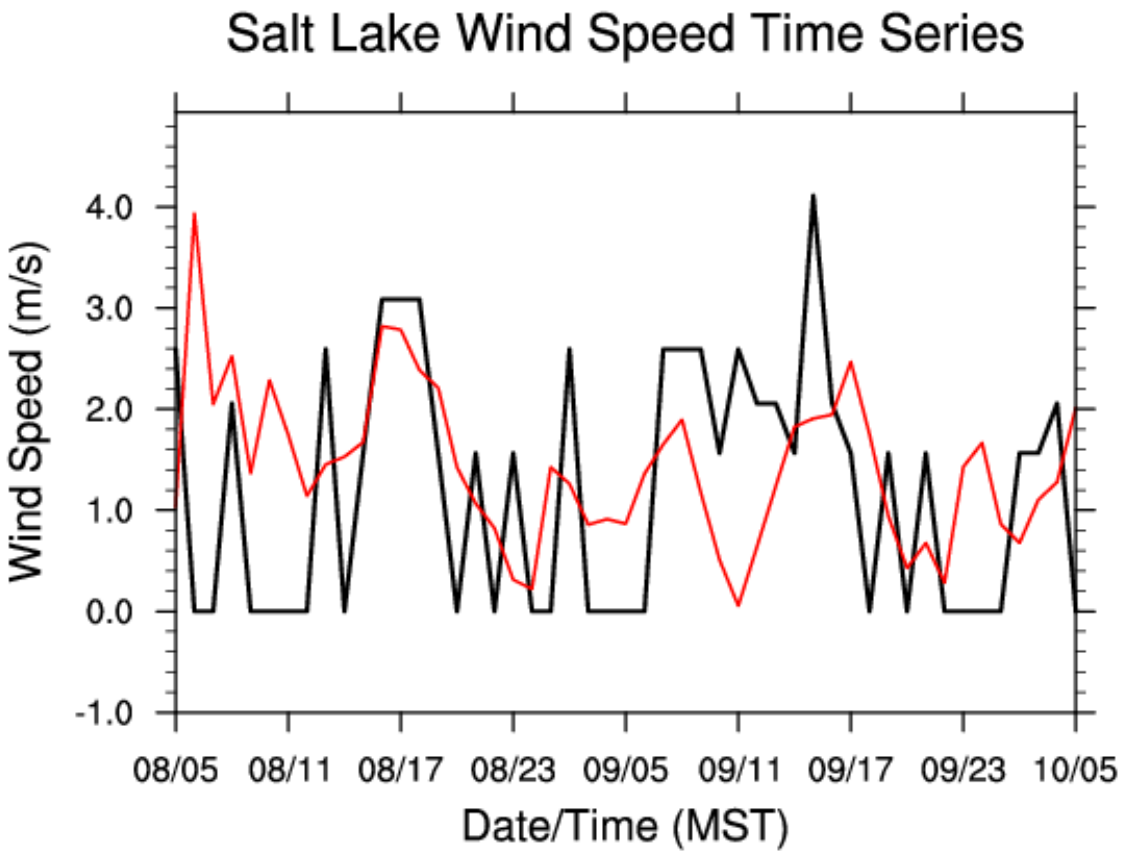


Figure 3.27. Wind speed time series comparison for duration of Thompson Aerosol Aware model simulation. Observed corrected relative humidity in black, model solution in red.

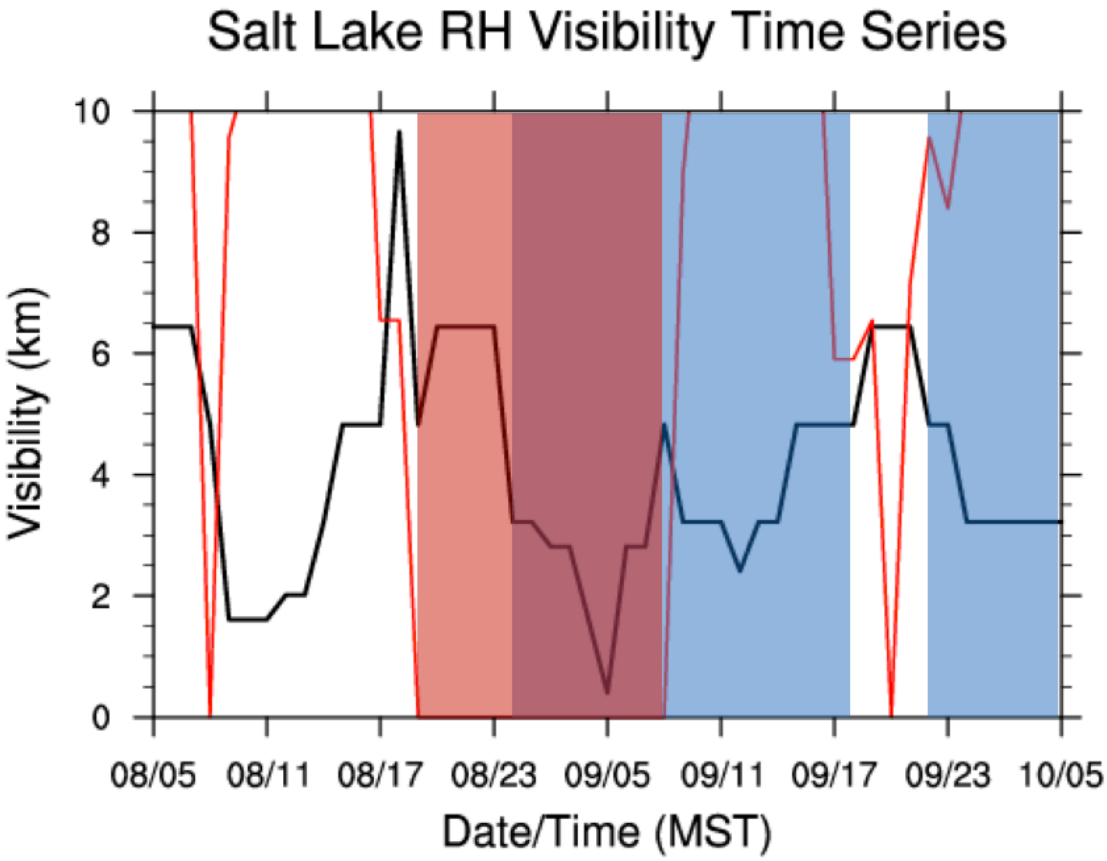


Figure 3.28. Visibility time series comparison calculated with respect to corrected relative humidity for Thompson Aerosol Aware simulation. Observed visibility is in black, model solution in red. Blue shading represents observed fog, and red shading represents fog in model solution.

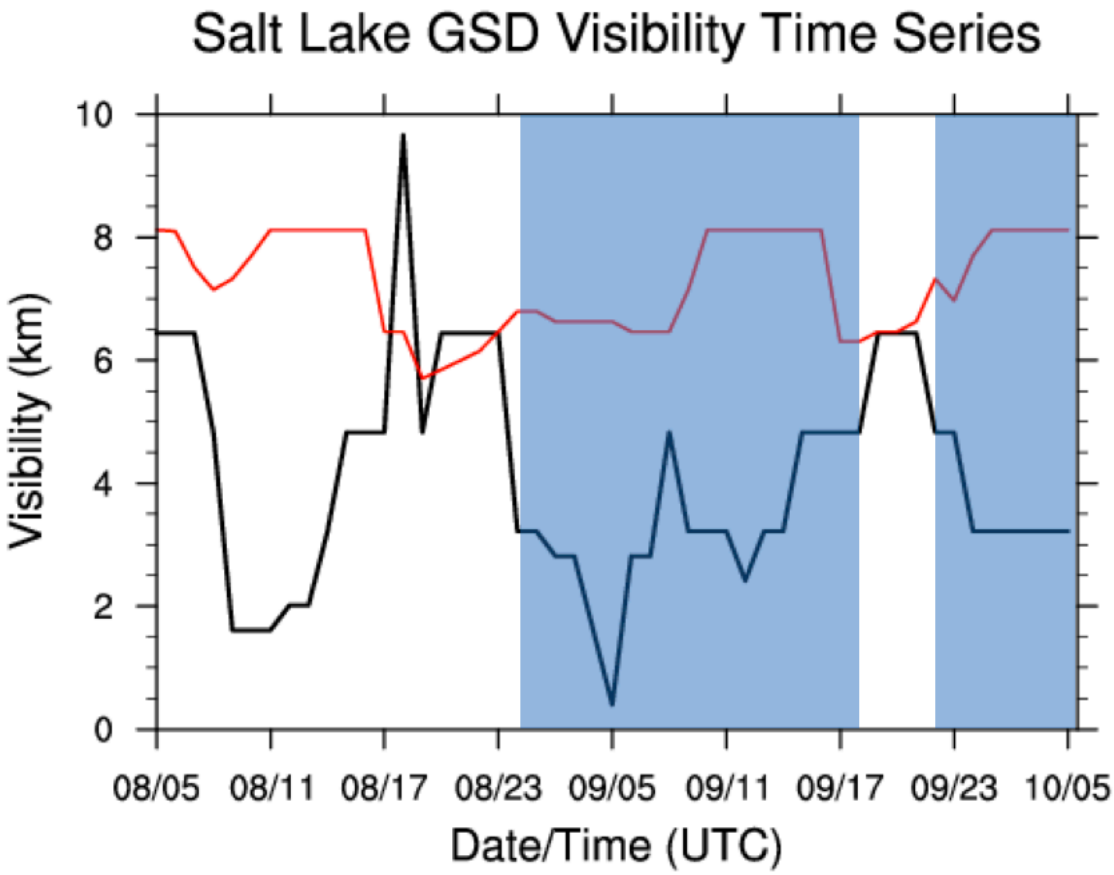


Figure 3.29. Visibility time series comparison calculated with respect to GSD visibility algorithm for Thompson Aerosol Aware scheme. Observed visibility is in black, model solution in red. Blue shading represents observed fog, and red shading represents fog in model solution.

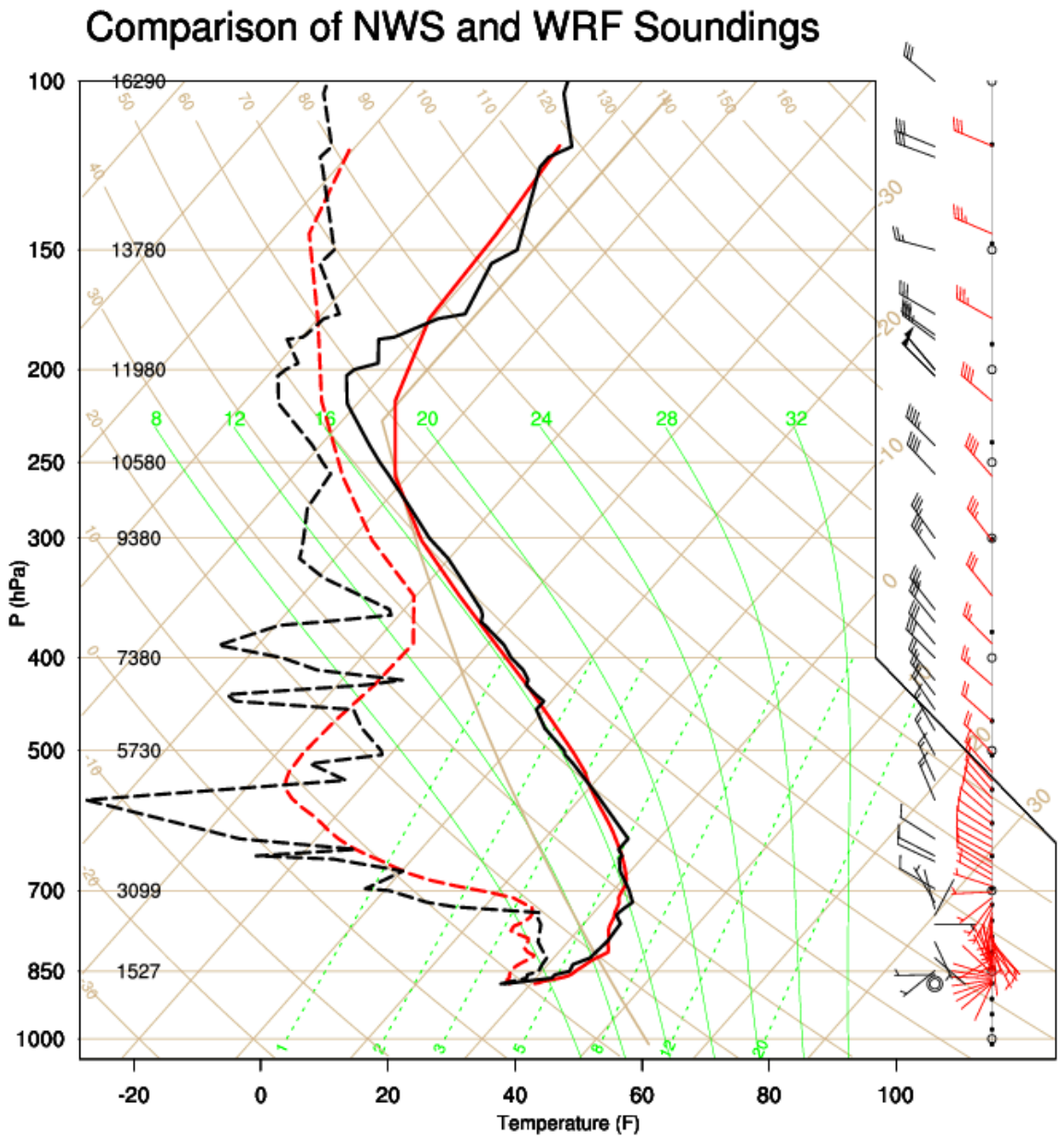


Figure 3.30. Sounding comparison at Salt Lake City International Airport (KSLC) from 1200 UTC 09 January 2015 between observations and sensitivity test run with Lin cloud microphysics. Temperature (F) along x-axis and pressure (hPa) along y-axis. Temperature (C) (straight beige lines), dry adiabats (curved beige lines), moist adiabats (curved green lines), saturation mixing ratio lines (dotted straight green lines), and wind barbs (speed in knots) analyzed. Observed temperature for this sounding represented by the solid black line, and observed dew point temperature for this sounding represented the dotted black line. Modeled temperature for this sounding represented by the solid red line, and modeled dew point temperature for this sounding represented by the dotted red line.

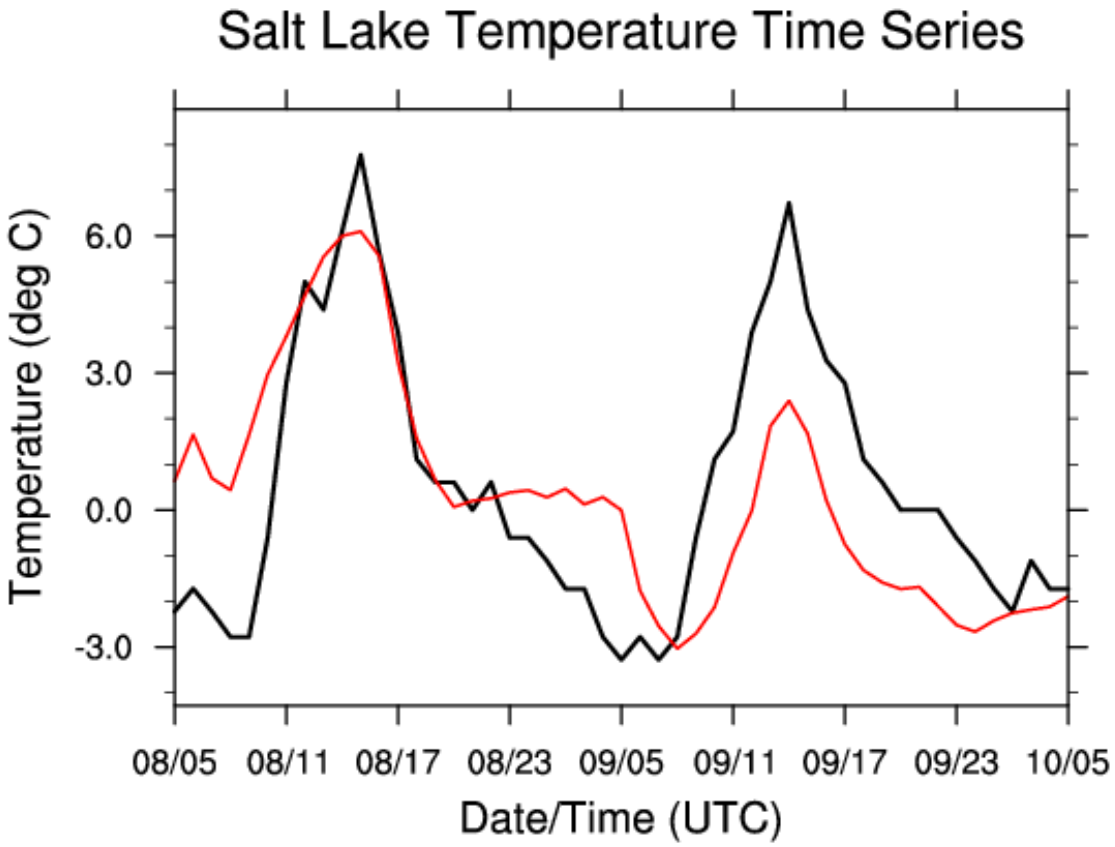


Figure 3.31. Temperature time series comparison for duration of Lin model simulation. Observed temperature in black, model solution in red.

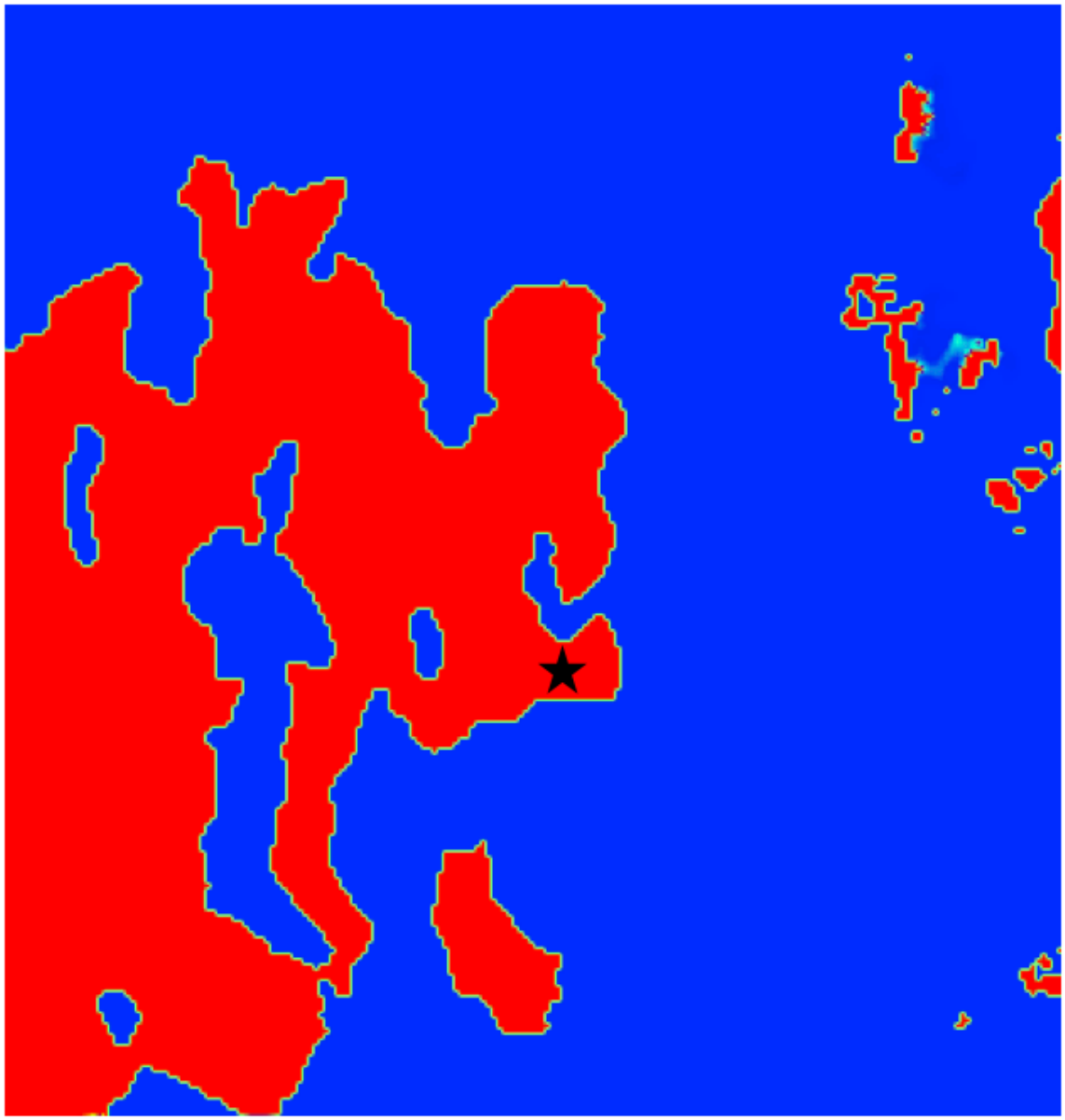

Figure 3.32. Map of cloud fraction for d04 for Lin cloud microphysics sensitivity test, valid 0500 MST 09 January. Red indicates a cloud fraction of 1, blue indicates a cloud fraction of 0. Black star indicates MATERHORN Salt Lake Valley site.

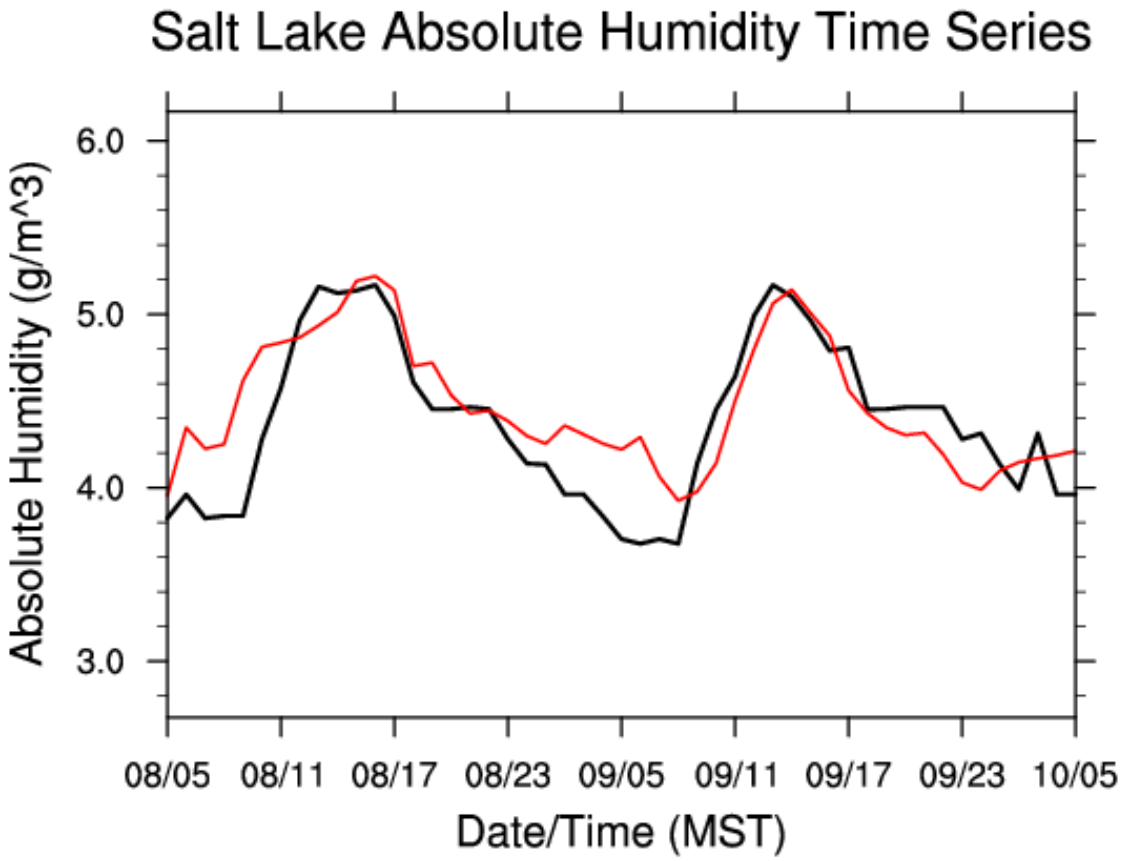


Figure 3.33. Absolute humidity time series comparison for duration of Lin cloud microphysics model simulation. Observed absolute humidity in black, model solution in red.

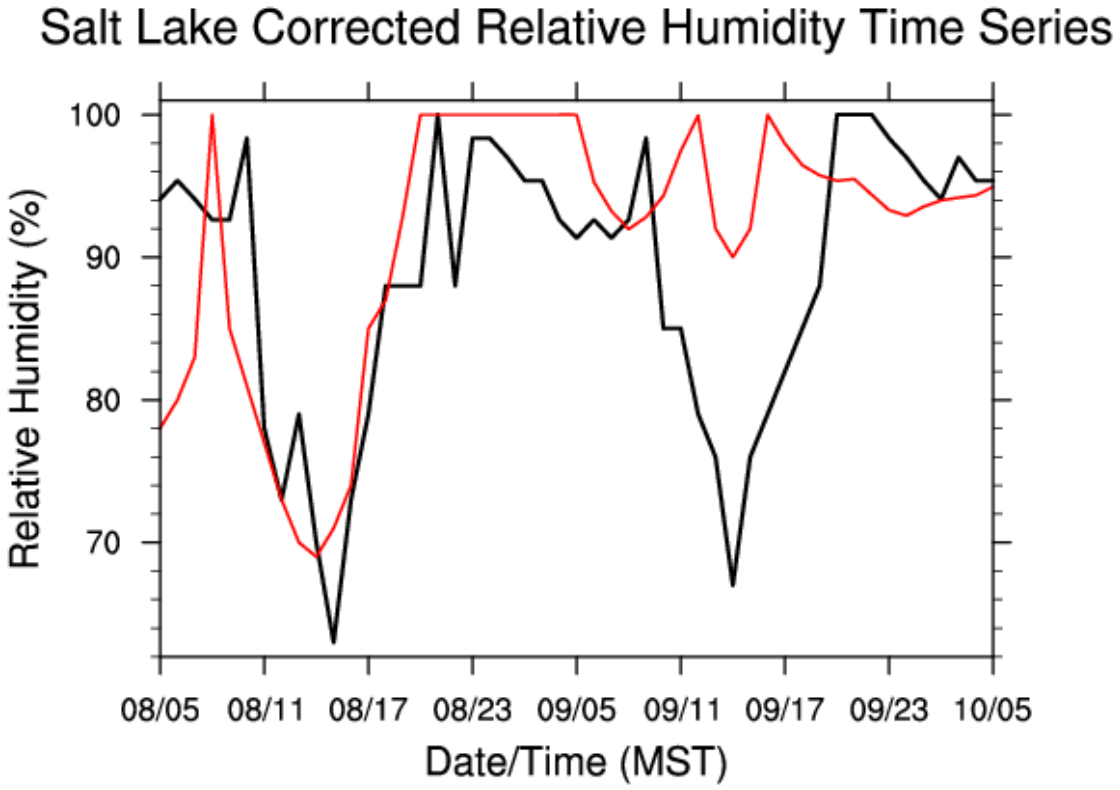


Figure 3.34. Corrected relative humidity time series comparison for duration of Lin cloud microphysics model simulation. Observed corrected relative humidity in black, model solution in red.

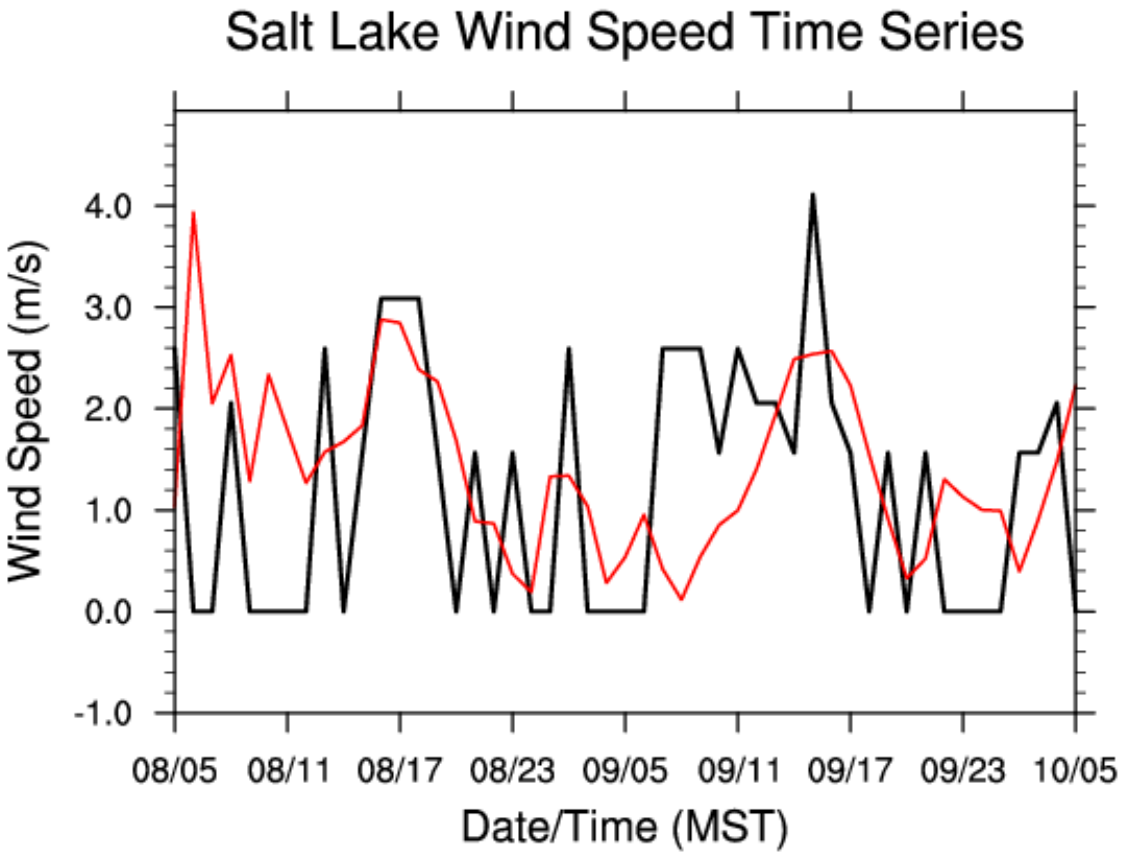


Figure 3.35. Wind speed time series comparison for duration of Lin cloud microphysics model simulation. Observed corrected relative humidity in black, model solution in red.

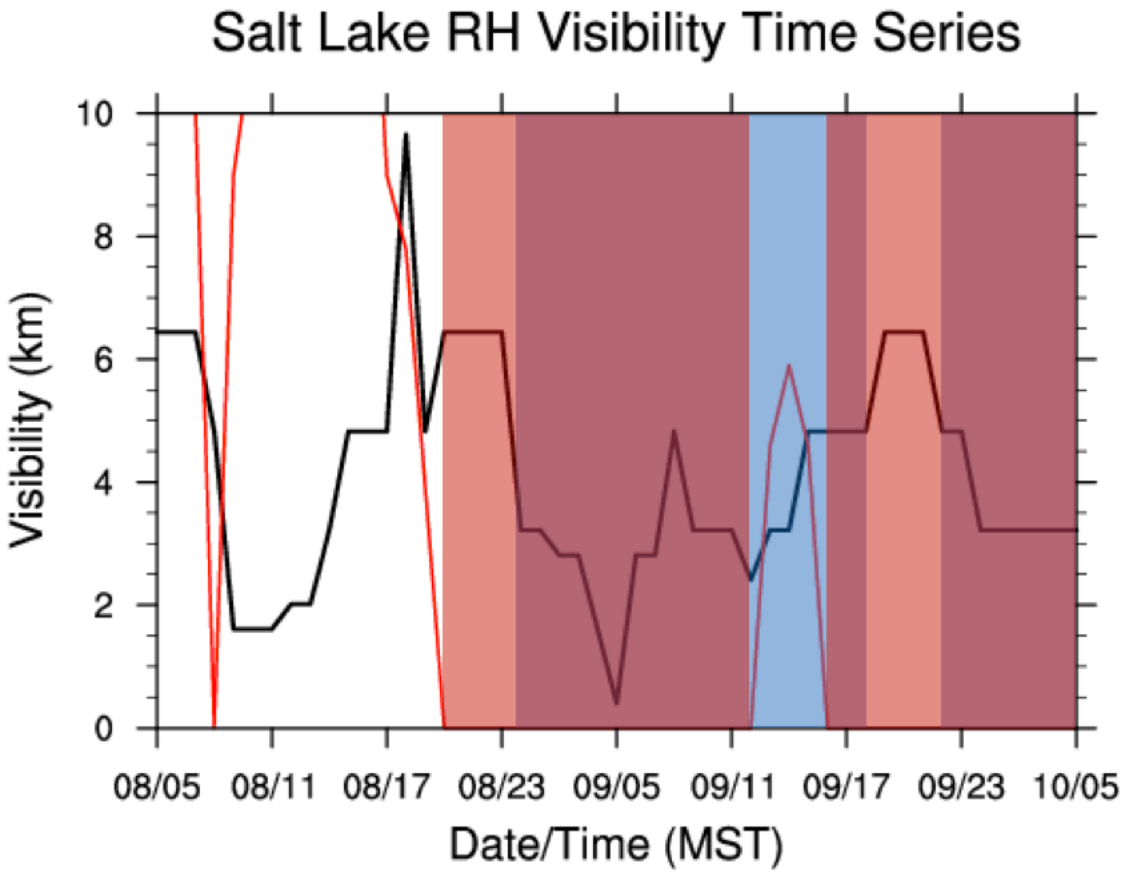


Figure 3.36. Visibility time series comparison calculated with respect to corrected relative humidity for Lin cloud microphysics simulation. Observed visibility is in black, model solution in red. Blue shading represents observed fog, and red shading represents fog in model solution.

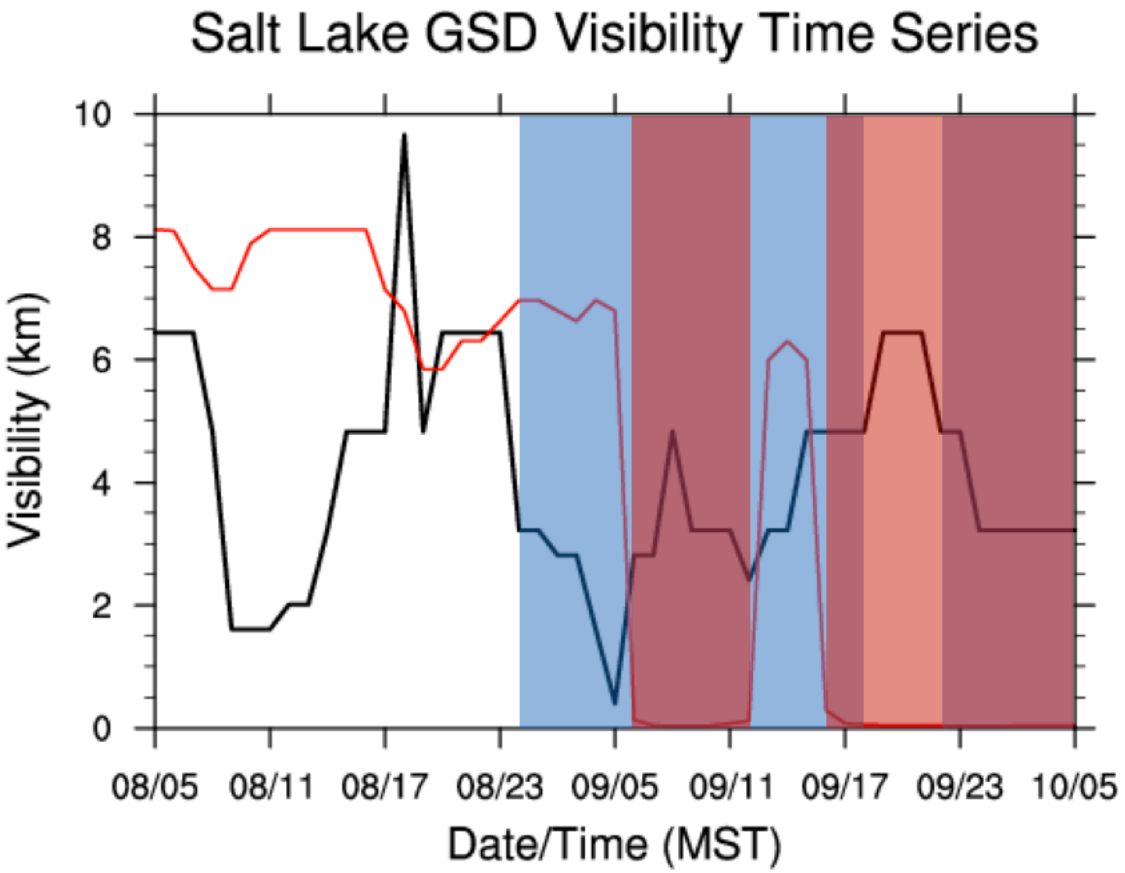


Figure 3.37. Visibility time series comparison calculated with respect to the GSD visibility algorithm for the Lin cloud microphysics simulation. Observed visibility is in black, model solution in red. Blue shading represents observed near fog, and red shading represents fog in model solution.

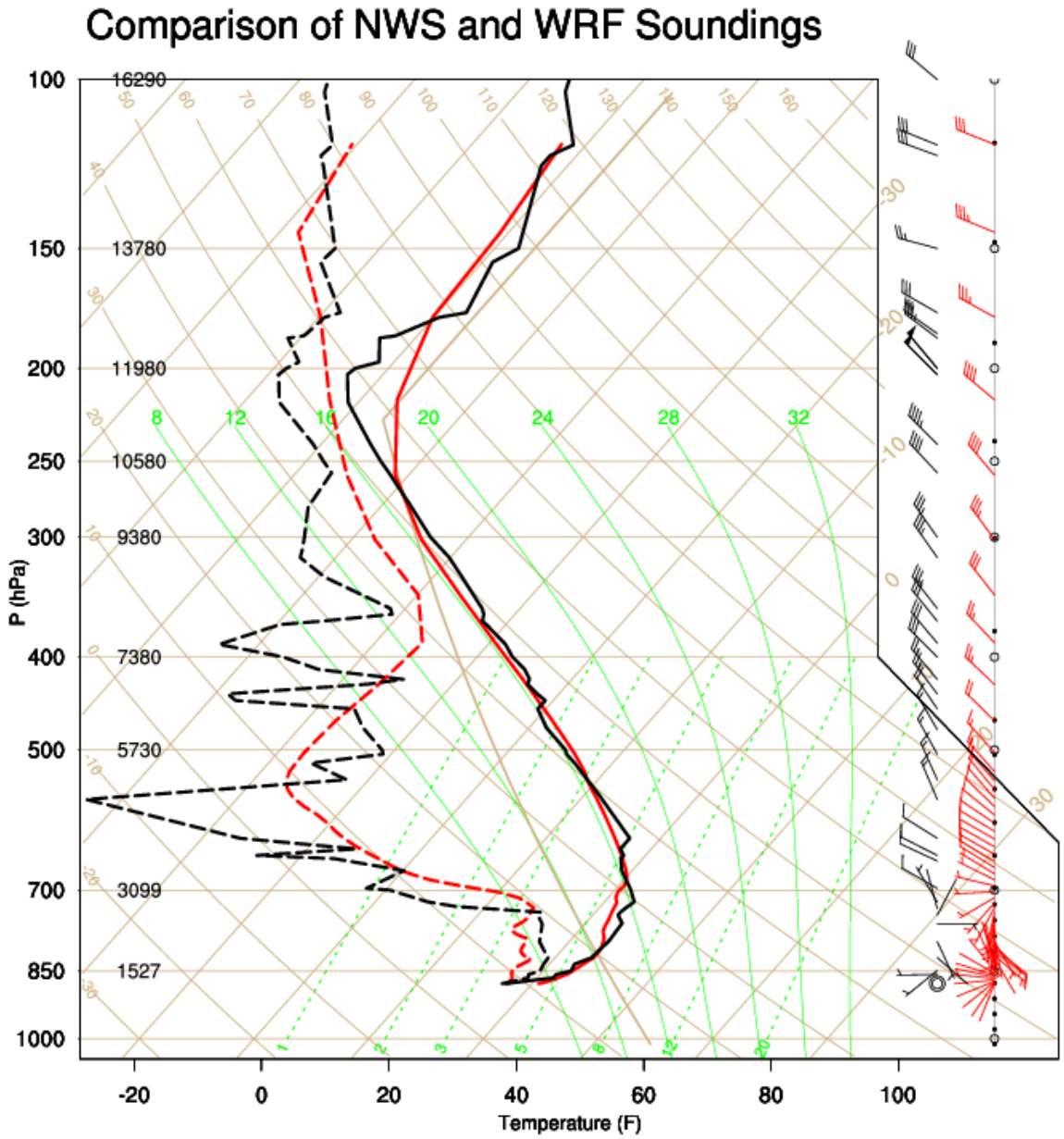


Figure 3.38. Sounding comparison at Salt Lake City International Airport (KSLC) from 1200 UTC 09 January 2015 between observations and sensitivity test run with the MYJ planetary boundary layer scheme. Temperature (F) along x-axis and pressure (hPa) along y-axis. Temperature (C) (straight beige lines), dry adiabats (curved beige lines), moist adiabats (curved green lines), saturation mixing ratio lines (dotted straight green lines), and wind barbs (speed in knots) analyzed. Observed temperature for this sounding represented by the solid black line, and observed dew point temperature for this sounding represented the dotted black line. Modeled temperature for this sounding represented by the solid red line, and modeled dew point temperature for this sounding represented by the dotted red line.

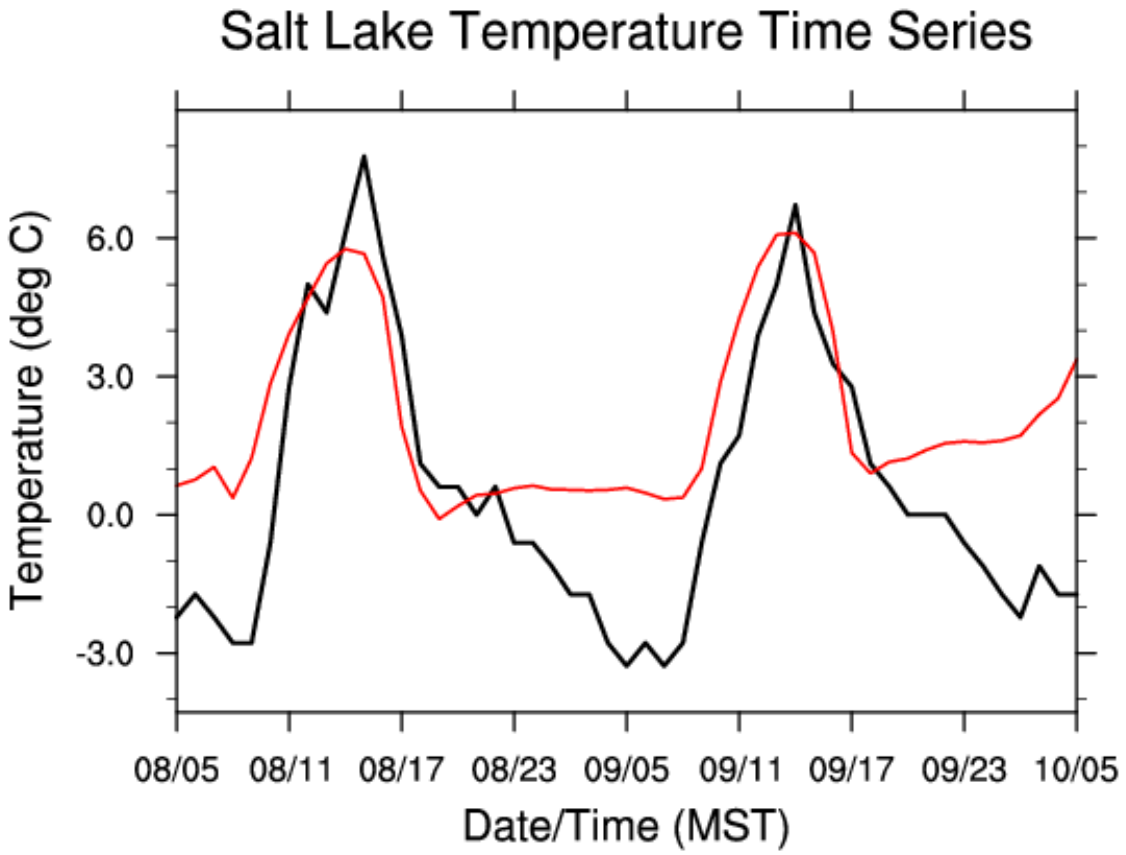


Figure 3.39. Temperature time series comparison for duration of MYJ planetary boundary layer model simulation. Observed temperature in black, model solution in red.

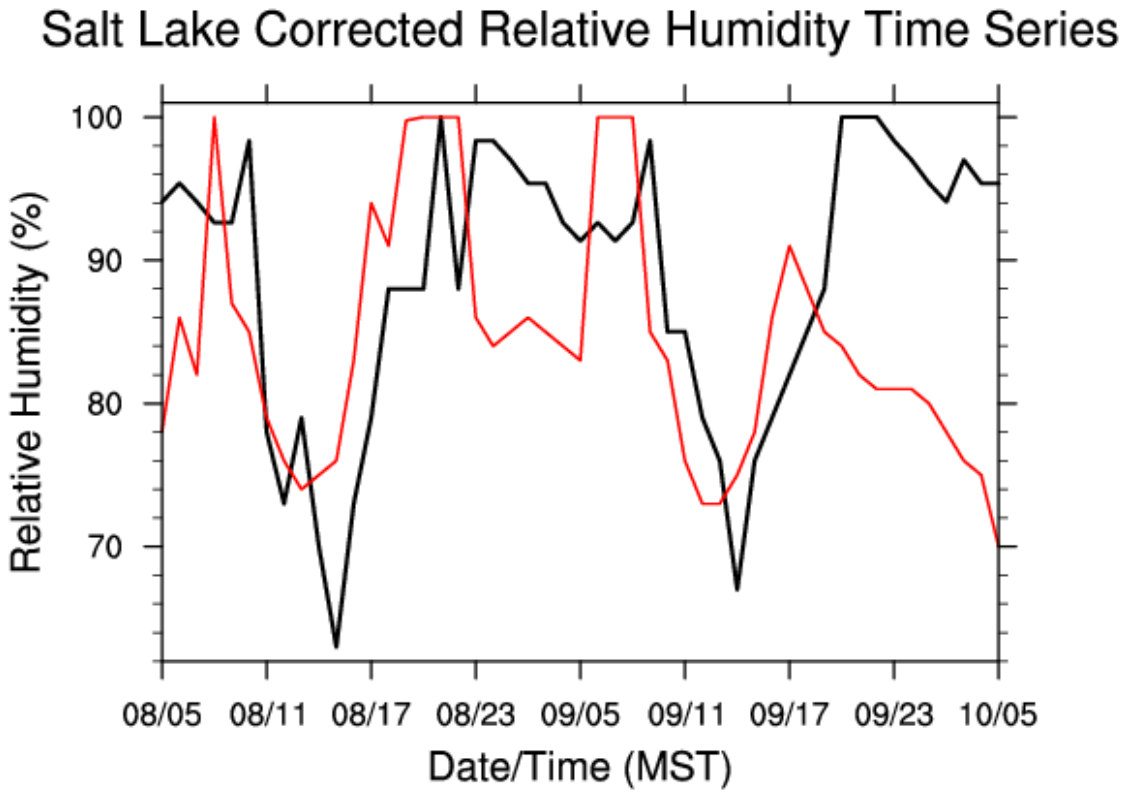


Figure 3.40. Corrected relative humidity time series comparison for duration of MYJ planetary boundary layer model simulation. Observed corrected relative humidity in black, model solution in red.

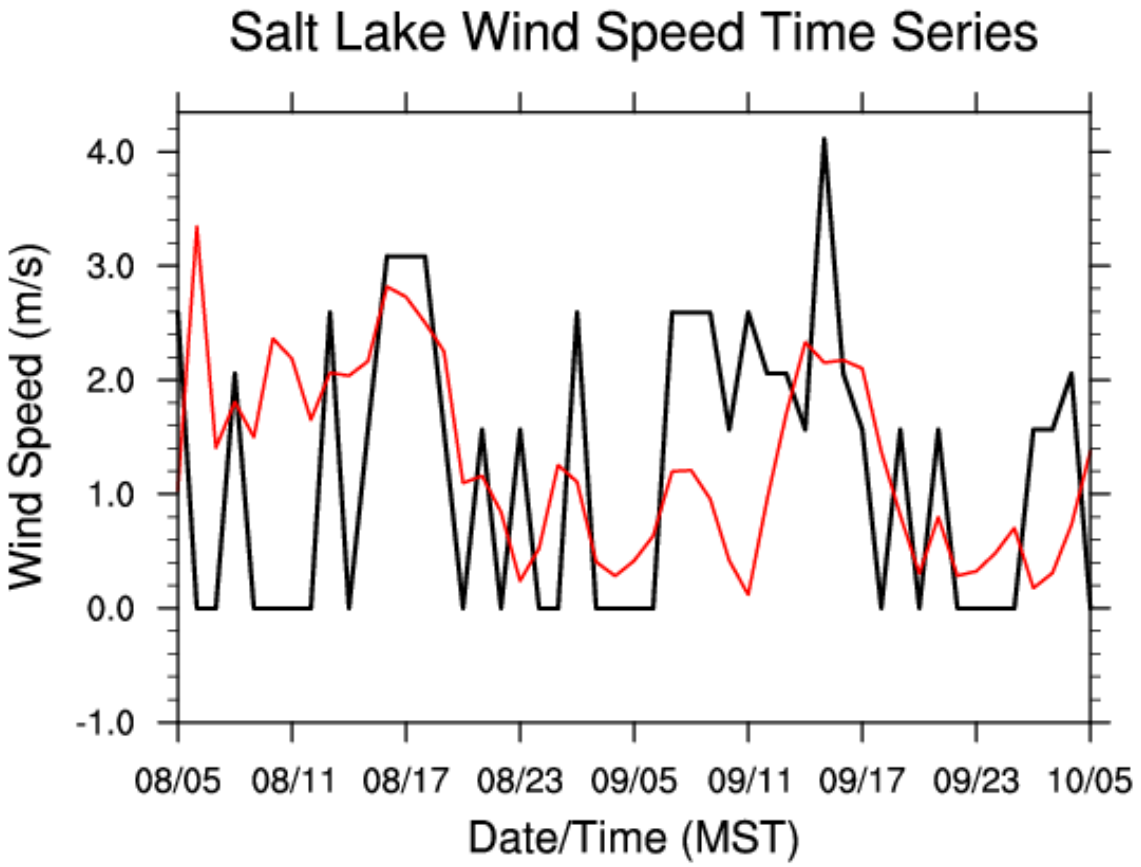


Figure 3.41. Wind speed time series comparison for duration of MYJ planetary boundary layer model simulation. Observed corrected relative humidity in black, model solution in red.

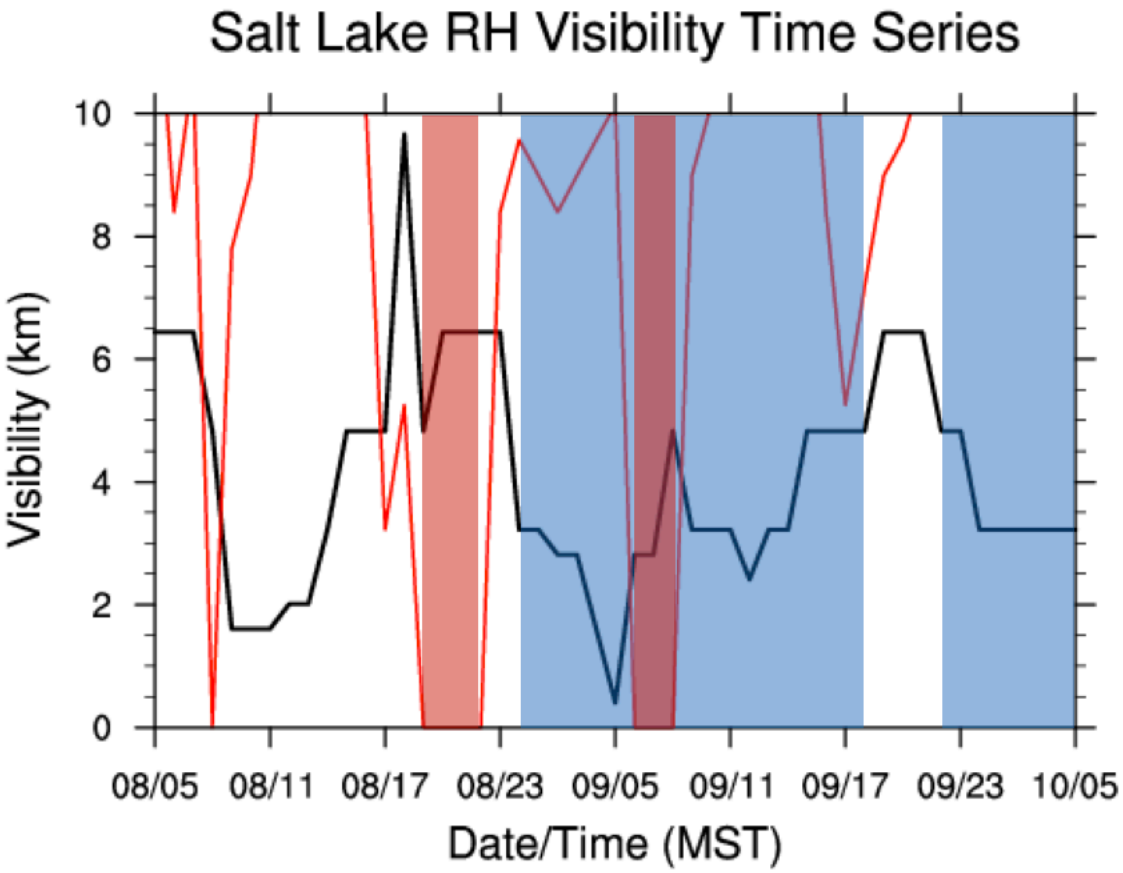


Figure 3.42. Visibility time series comparison calculated with respect to corrected relative humidity for MYJ planetary boundary layer simulation. Observed visibility is in black, model solution in red. Blue shading represents observed fog, and red shading represents fog in model solution.

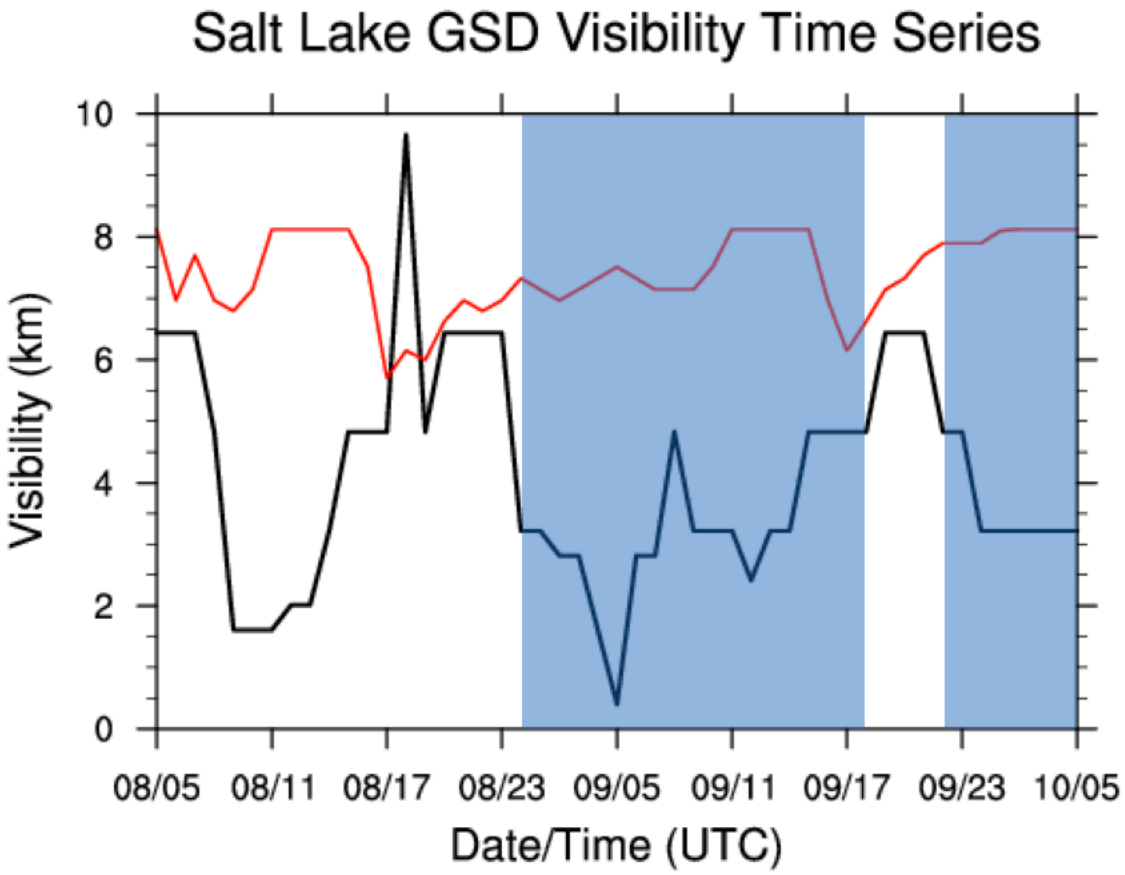


Figure 3.43. Visibility time series comparison calculated with respect to GSD visibility algorithm for the MYJ planetary boundary layer simulation. Observed visibility is in black, model solution in red. Blue shading represents observed near fog, and red shading represents fog in model solution.

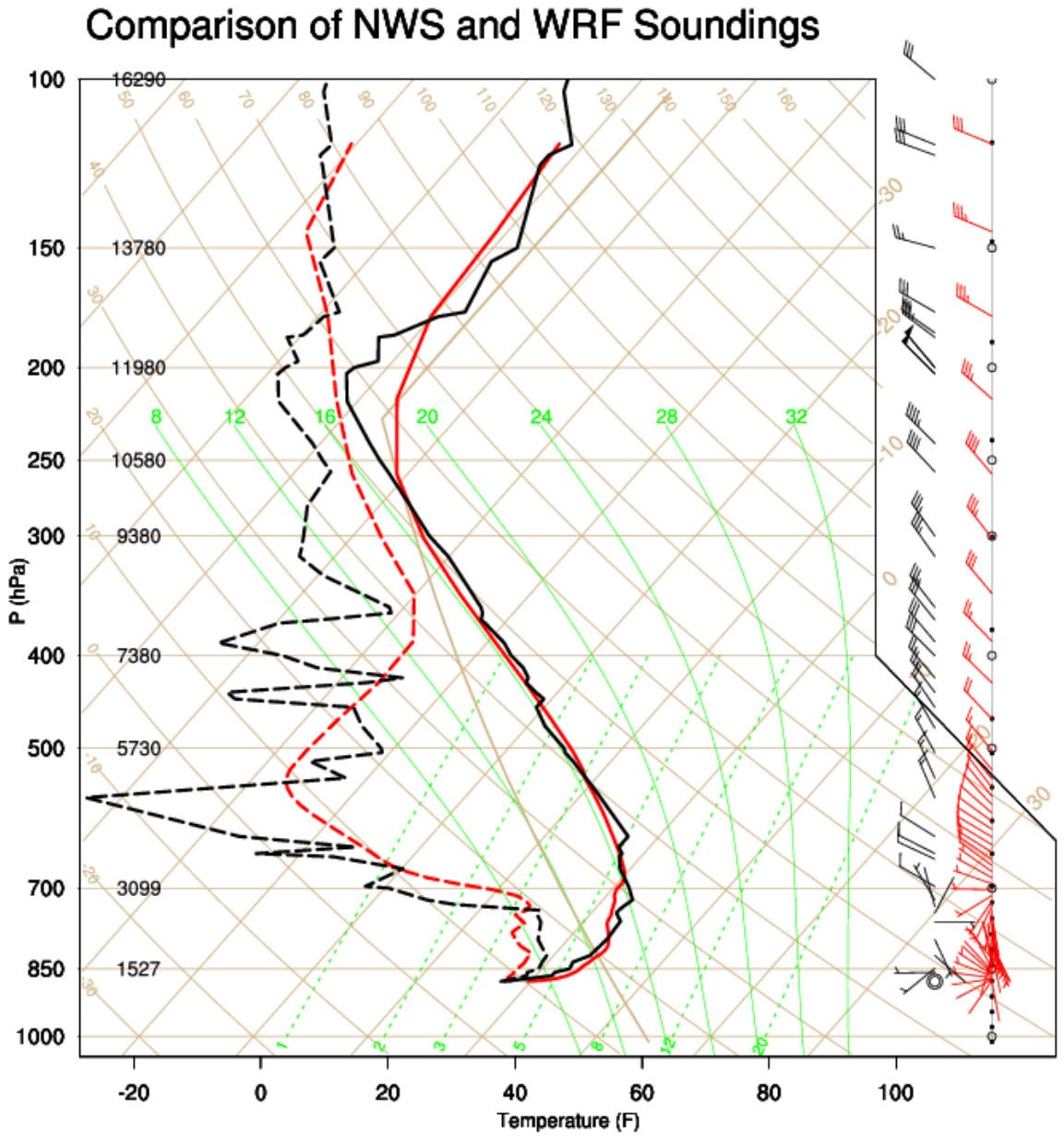


Figure 3.44. Sounding comparison at Salt Lake City International Airport (KSLC) from 1200 UTC 09 January 2015 between observations and sensitivity test run with the thermal diffusion land surface scheme. Temperature (F) along x-axis and pressure (hPa) along y-axis. Temperature (C) (straight beige lines), dry adiabats (curved beige lines), moist adiabats (curved green lines), saturation mixing ratio lines (dotted straight green lines), and wind barbs (speed in knots) analyzed. Observed temperature for this sounding represented by the solid black line, and observed dew point temperature for this sounding represented the dotted black line. Modeled temperature for this sounding represented by the solid red line, and modeled dew point temperature for this sounding represented by the dotted red line.

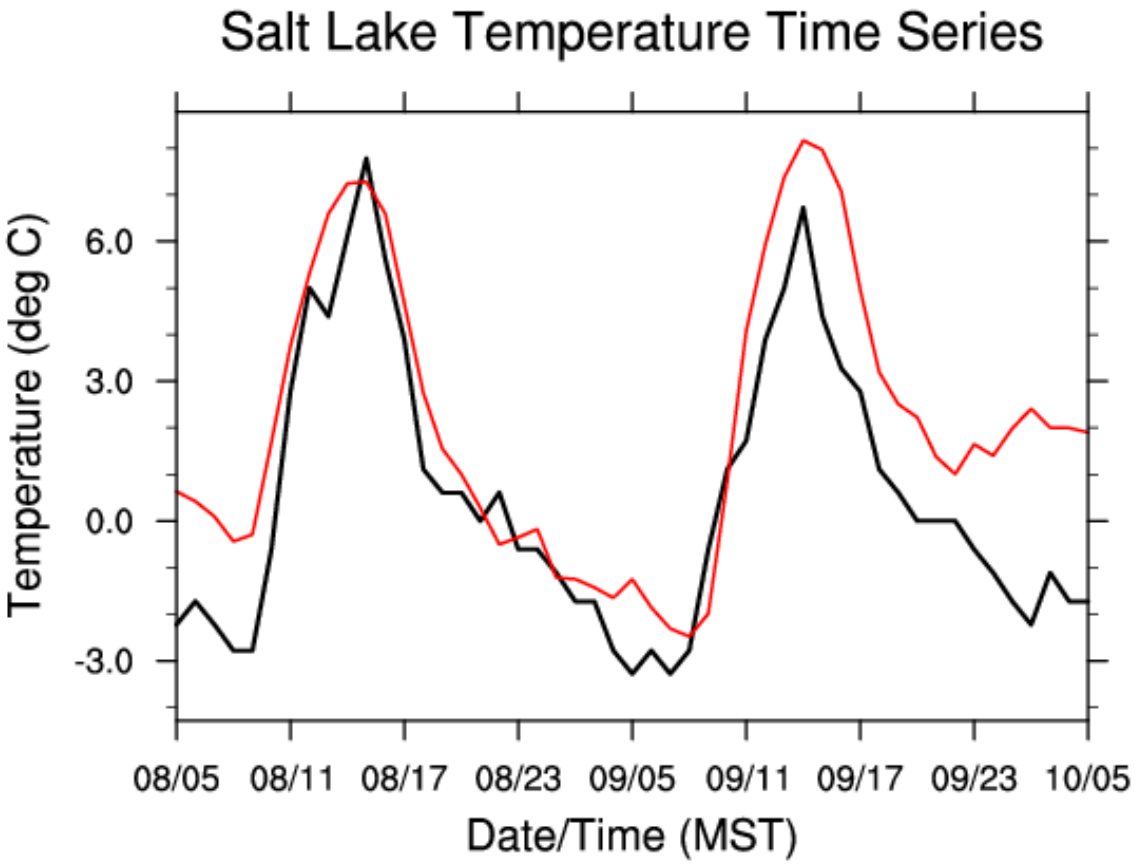


Figure 3.45. Temperature time series comparison for duration of the thermal diffusion land surface model simulation. Observed temperature in black, model solution in red.

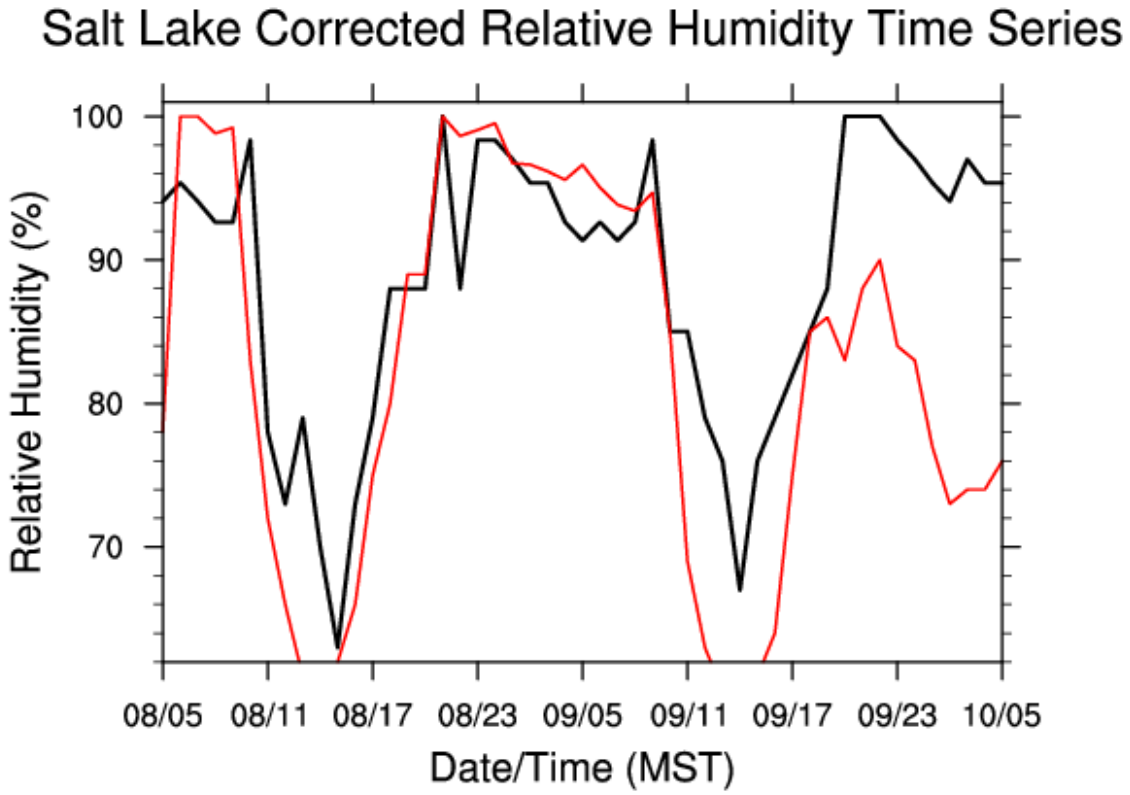


Figure 3.46. Corrected relative humidity time series comparison for duration of MYJ planetary boundary layer model simulation. Observed corrected relative humidity in black, model solution in red.

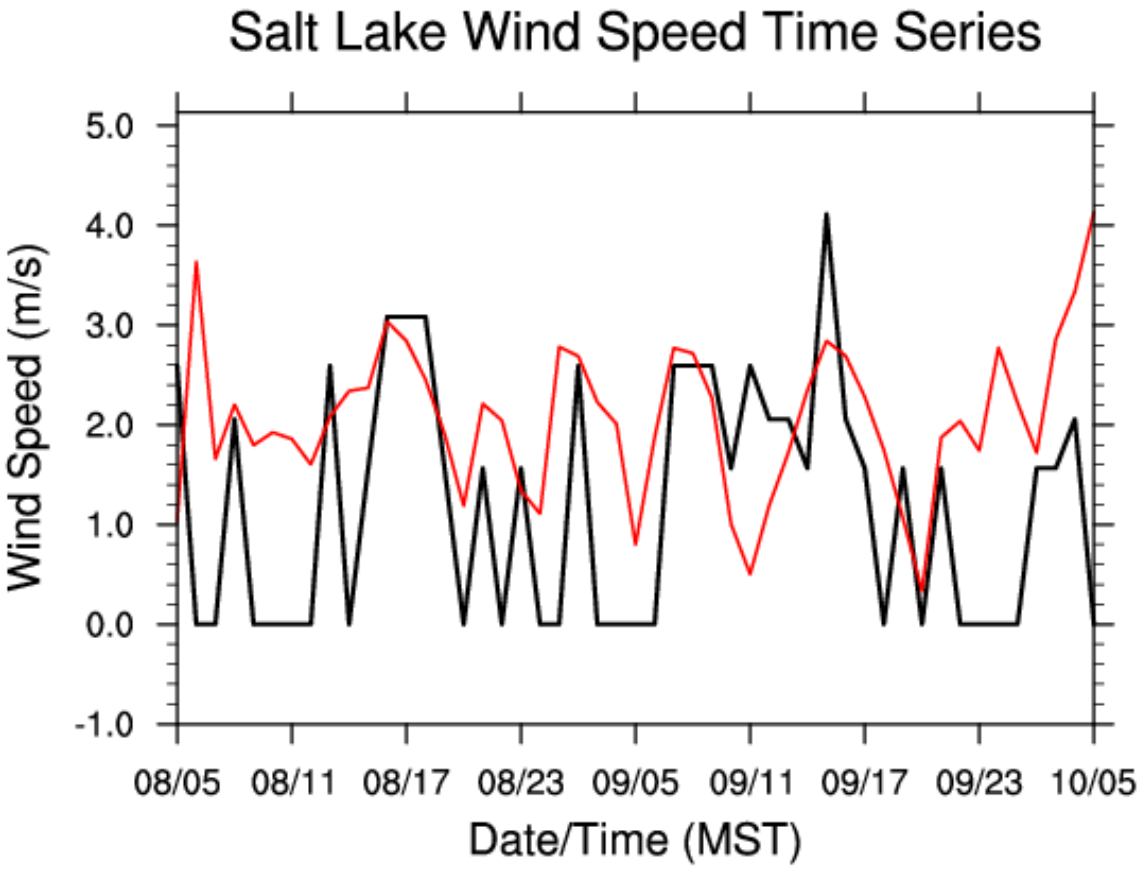


Figure 3.47. Wind speed time series comparison for duration of thermal diffusion land surface model simulation. Observed corrected relative humidity in black, model solution in red.

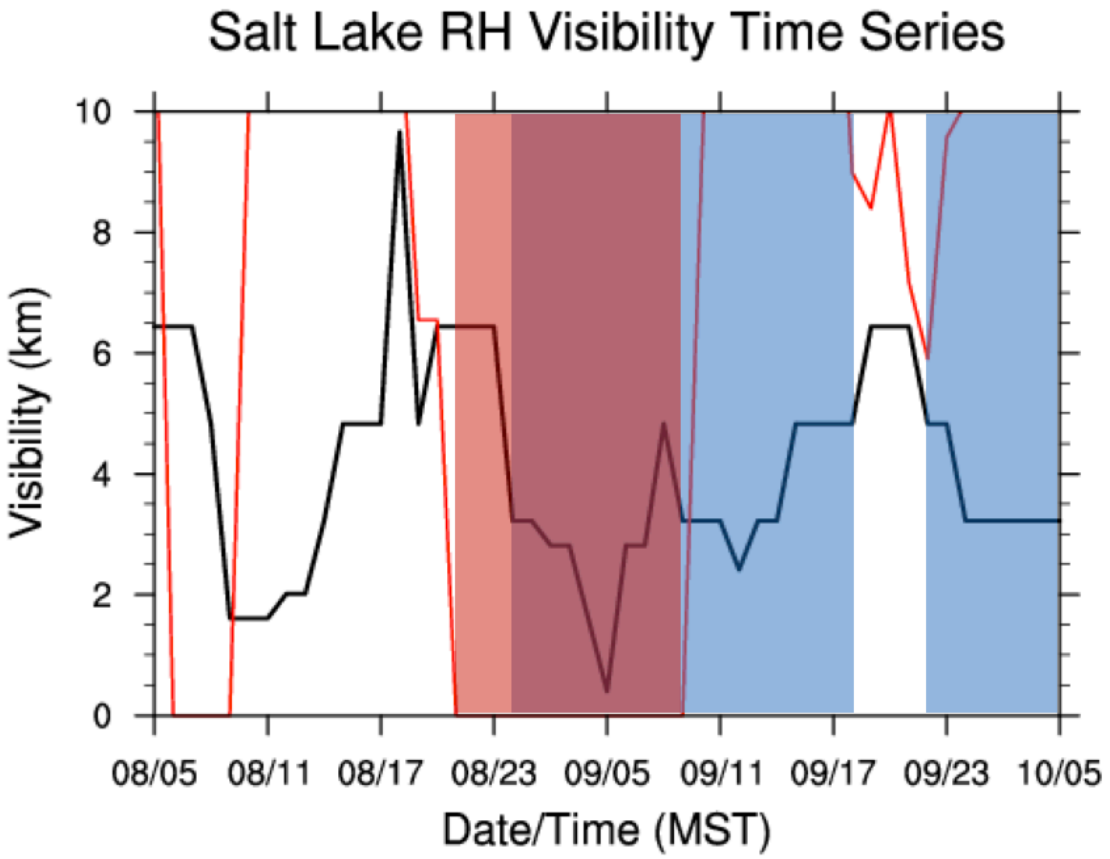


Figure 3.48. Visibility time series comparison calculated with respect to corrected relative humidity for thermal diffusion land surface simulation. Observed visibility is in black, model solution in red. Blue shading represents observed fog, and red shading represents fog in model solution.

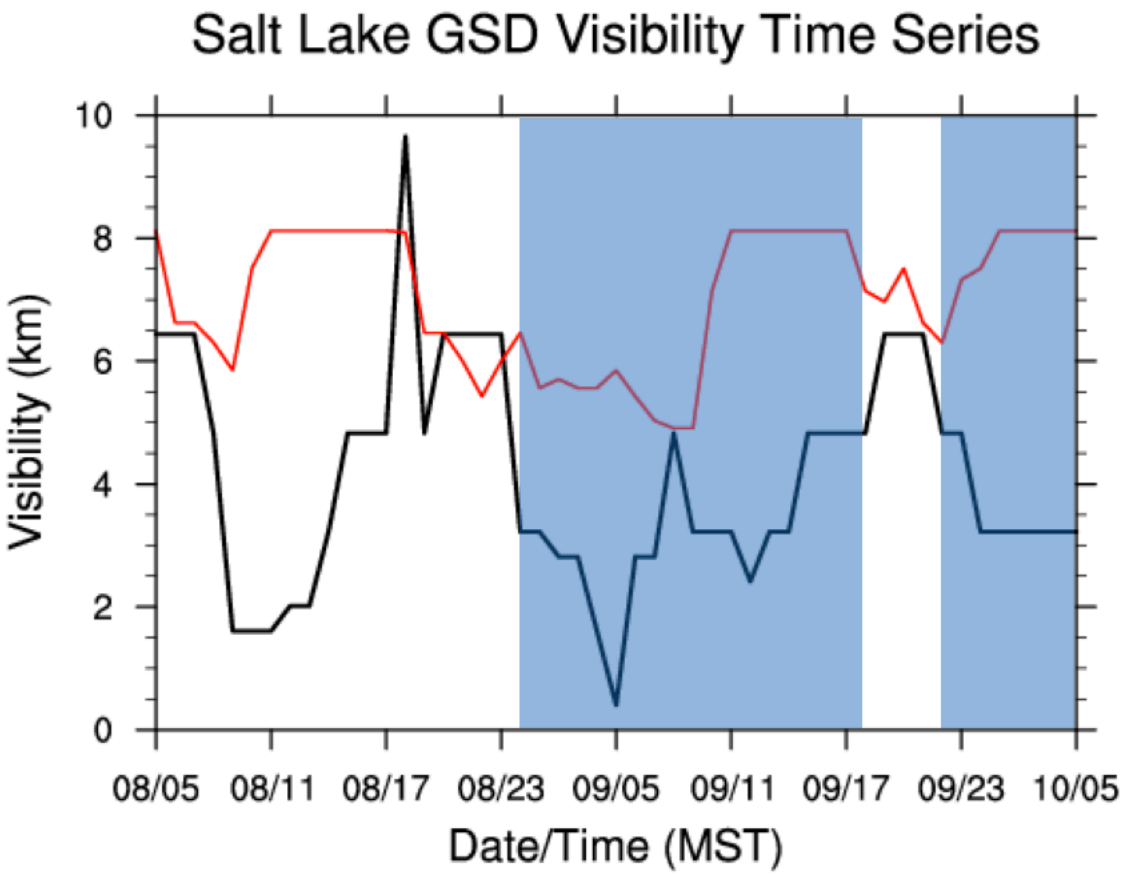


Figure 3.49. Visibility time series comparison calculated with respect to GSD visibility algorithm for thermal diffusion land surface simulation. Observed visibility is in black, model solution in red. Blue shading represents observed near fog, and red shading represents fog in model solution.

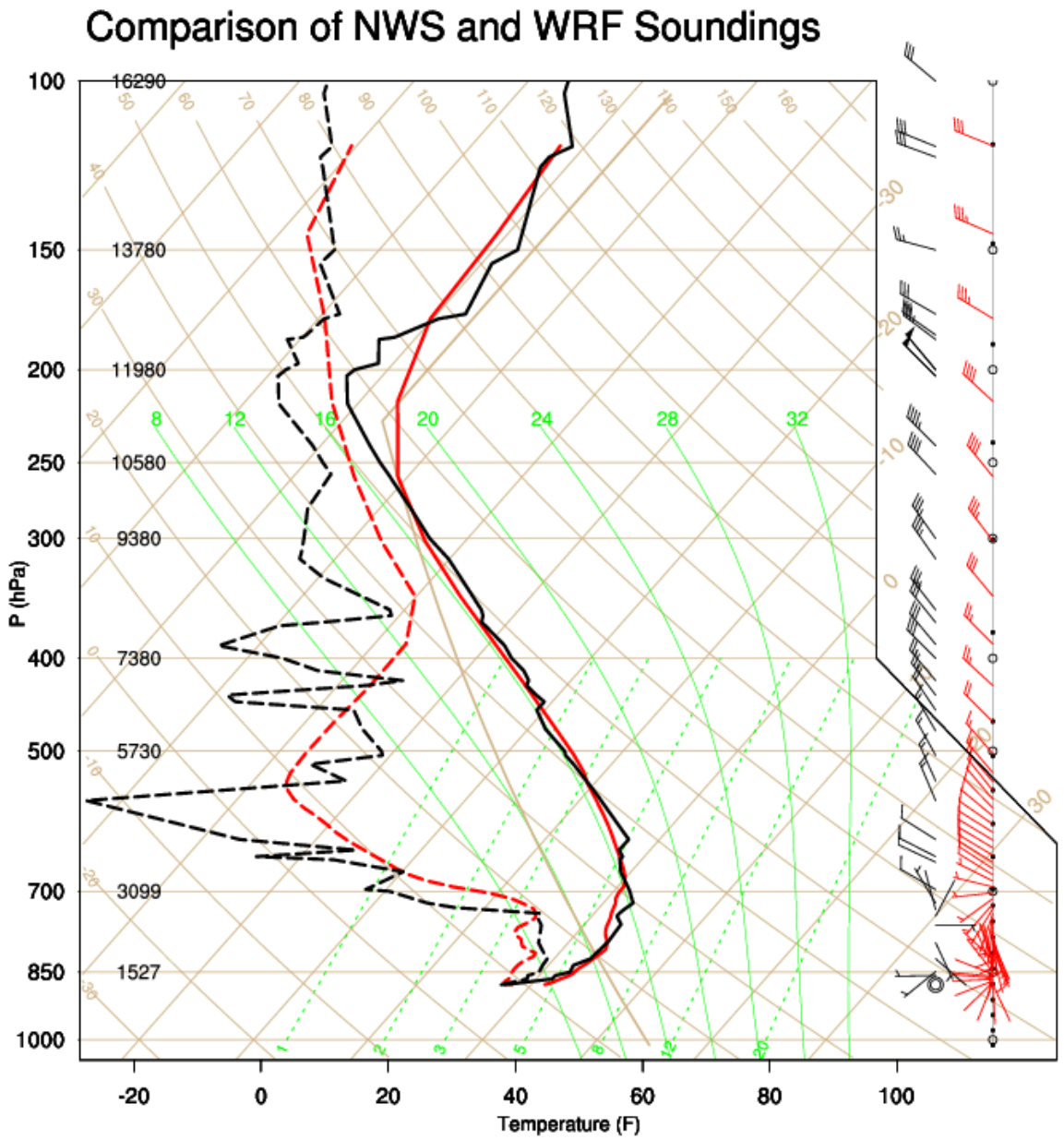


Figure 3.50. Sounding comparison at Salt Lake City International Airport (KSLC) from 1200 UTC 09 January 2015 between observations and sensitivity test run with forced initial albedo values. Temperature (F) along x-axis and pressure (hPa) along y-axis. Temperature (C) (straight beige lines), dry adiabats (curved beige lines), moist adiabats (curved green lines), saturation mixing ratio lines (dotted straight green lines), and wind barbs (speed in knots) analyzed. Observed temperature for this sounding represented by the solid black line, and observed dew point temperature for this sounding represented the dotted black line. Modeled temperature for this sounding represented by the solid red line, and modeled dew point temperature for this sounding represented by the dotted red line.

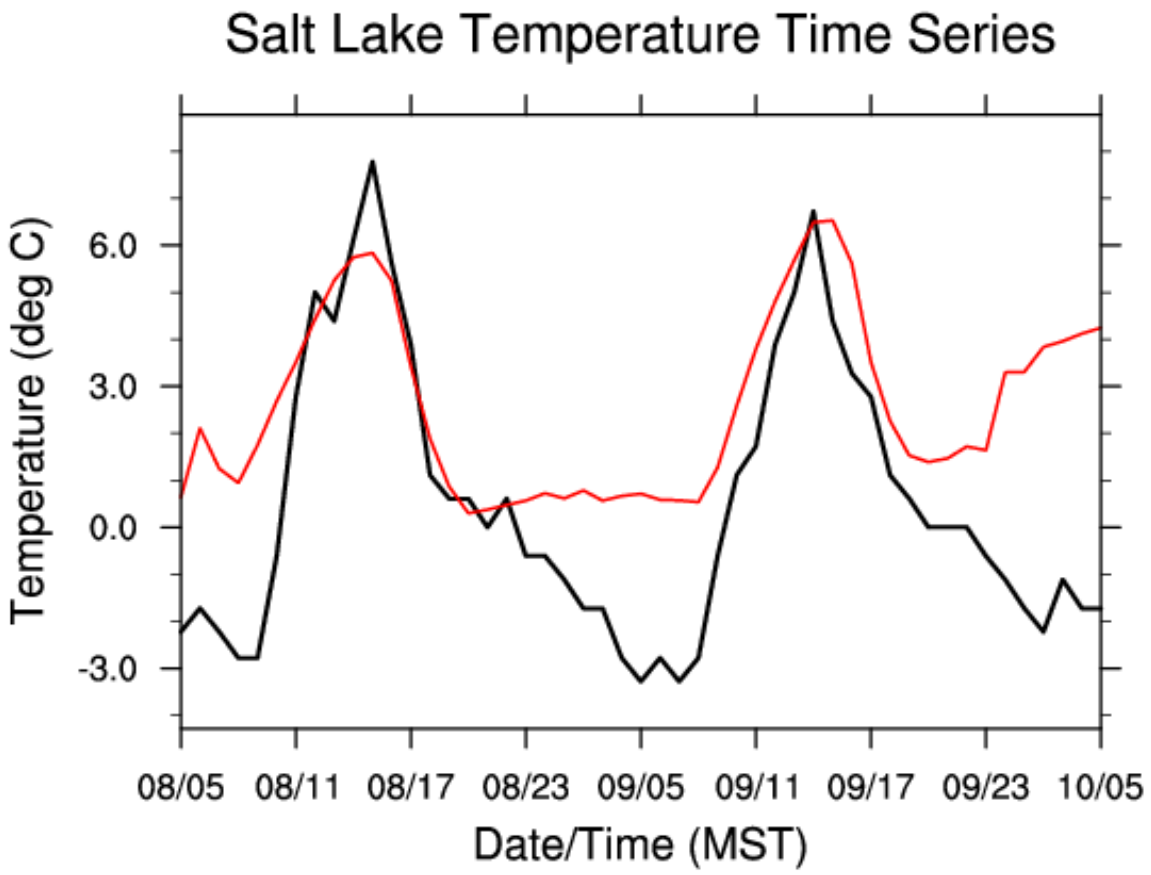


Figure 3.51. Temperature time series comparison for duration of the forced initial albedo simulation. Observed temperature in black, model solution in red.

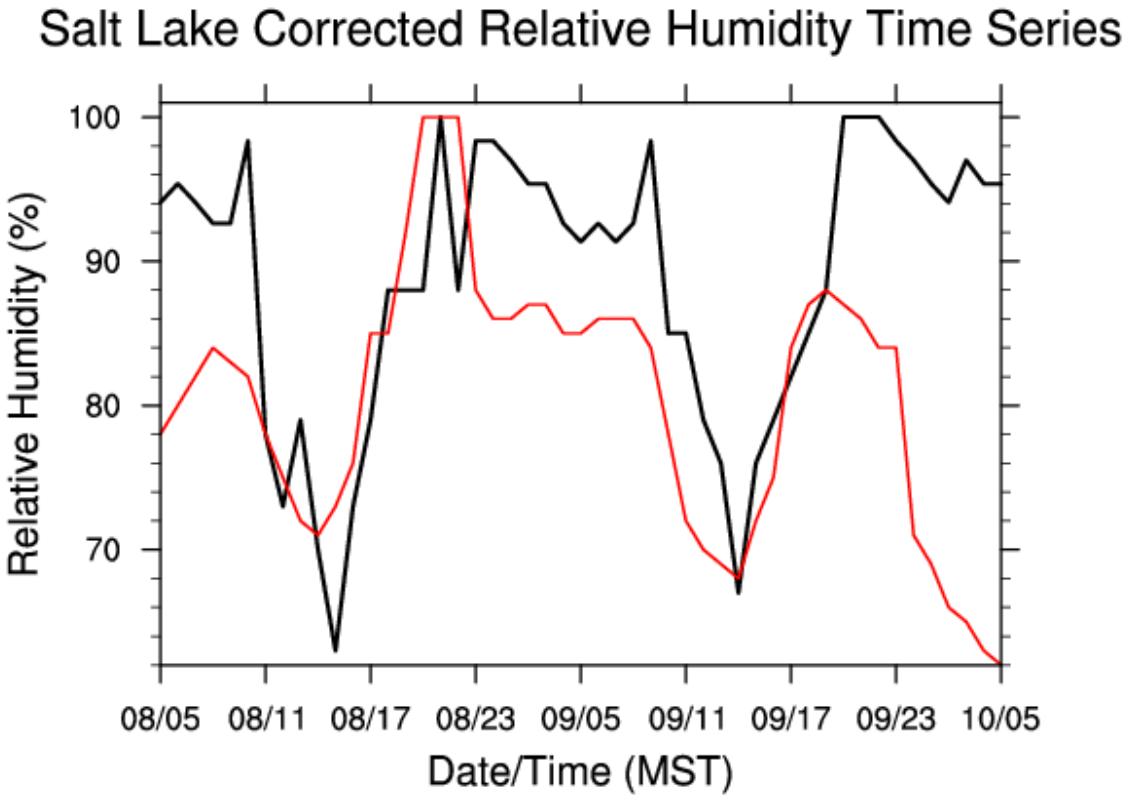


Figure 3.52. Corrected relative humidity time series comparison for duration of the forced initial albedo simulation. Observed corrected relative humidity in black, model solution in red.

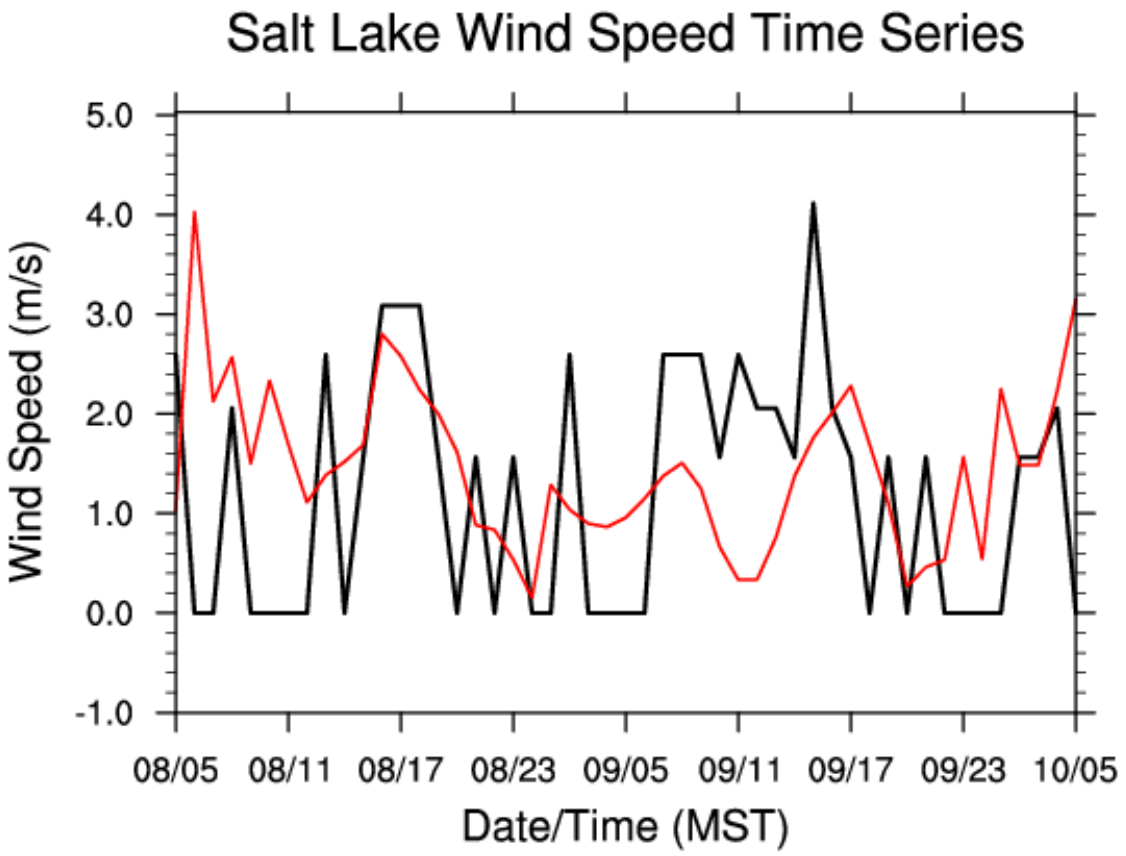


Figure 3.53. Wind speed time series comparison for duration of the forced initial albedo simulation. Observed corrected relative humidity in black, model solution in red.

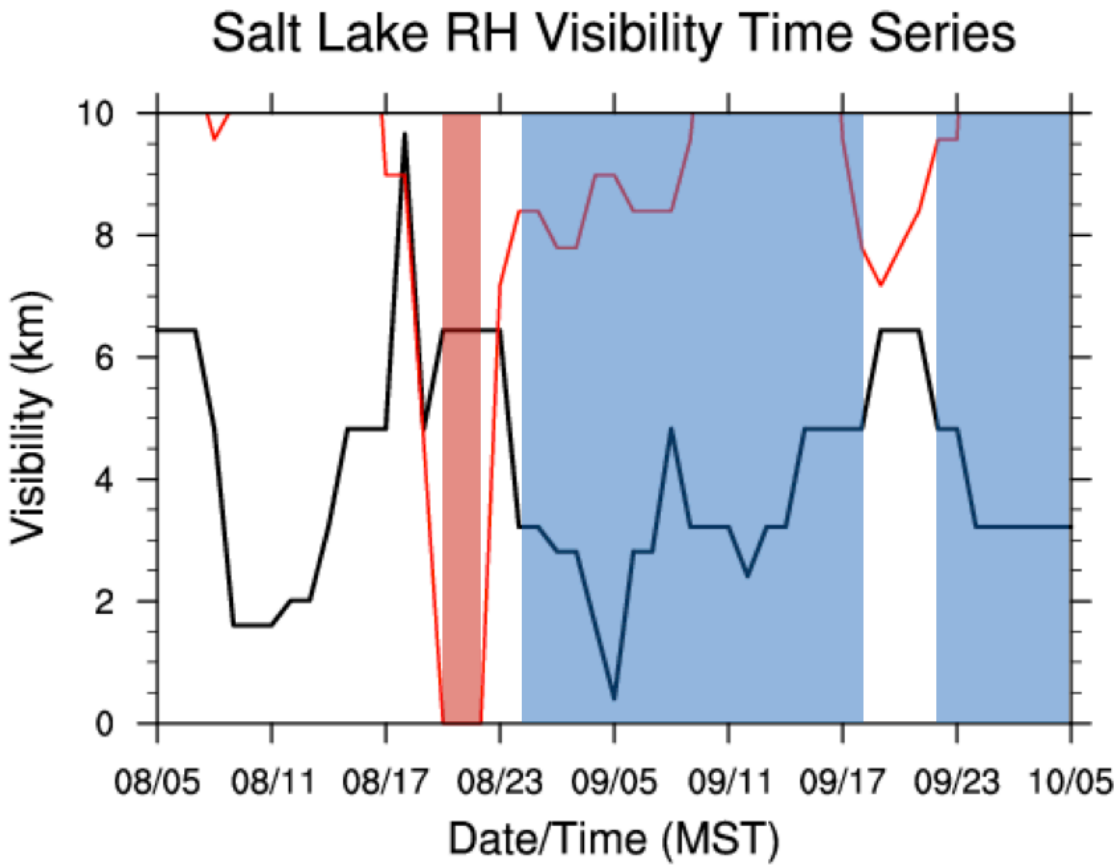


Figure 3.54. Visibility time series comparison calculated with respect to corrected relative humidity for the forced initial albedo simulation. Observed visibility is in black, model solution in red. Blue shading represents observed fog, and red shading represents fog in model solution.

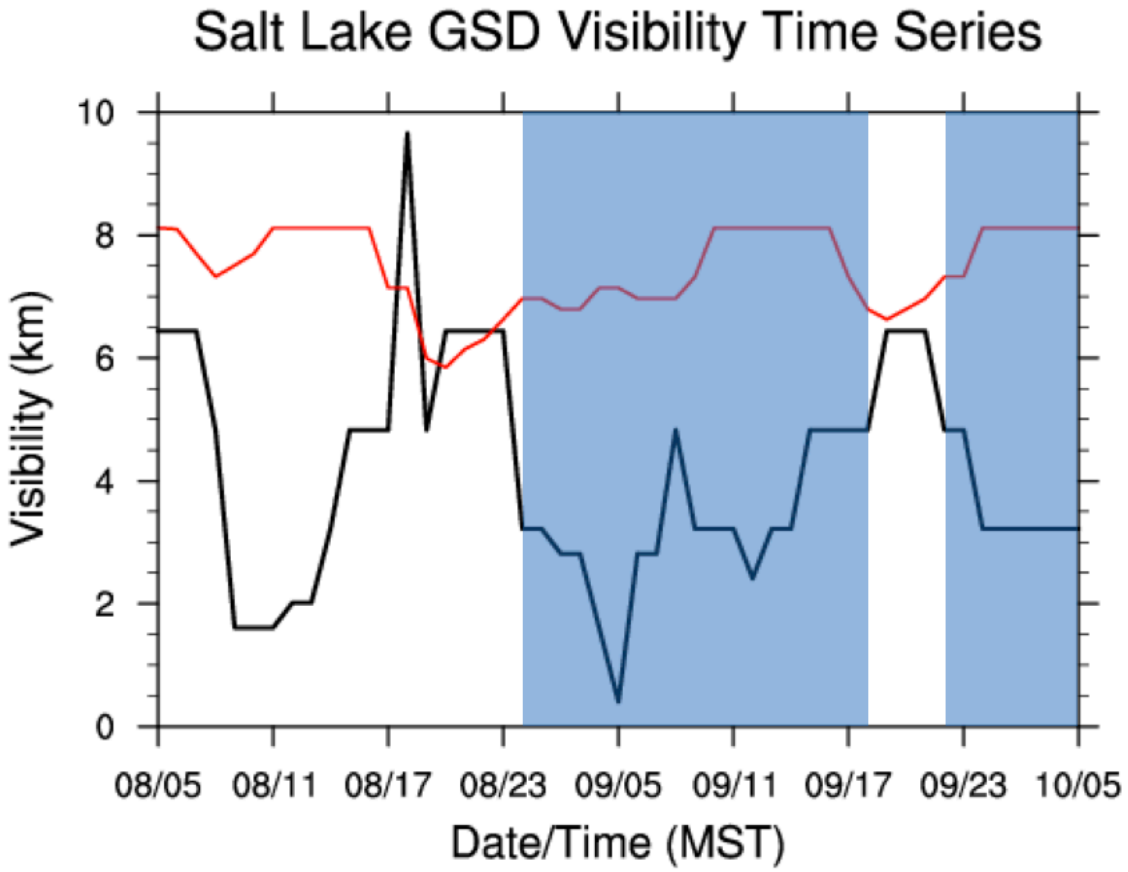


Figure 3.55. Visibility time series comparison calculated with respect to GSD visibility algorithm for the forced initial albedo simulation. Observed visibility is in black, model solution in red. Blue shading represents observed fog, and red shading represents fog in model solution.

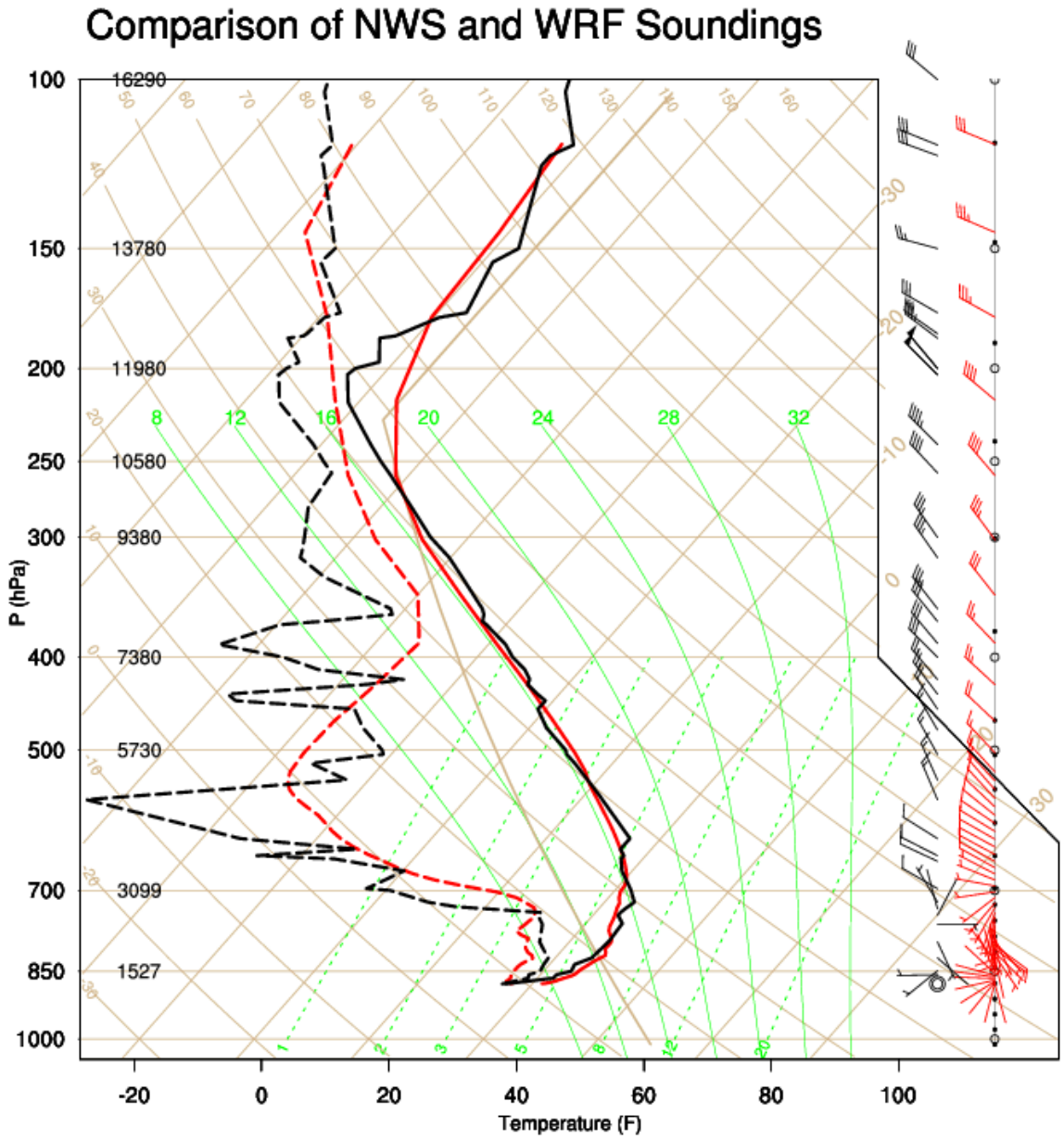


Figure 3.56. Sounding comparison at Salt Lake City International Airport (KSLC) from 1200 UTC 09 January 2015 between observations and sensitivity test run with the Goddard shortwave radiation scheme. Temperature (F) along x-axis and pressure (hPa) along y-axis. Temperature (C) (straight beige lines), dry adiabats (curved beige lines), moist adiabats (curved green lines), saturation mixing ratio lines (dotted straight green lines), and wind barbs (speed in knots) analyzed. Observed temperature for this sounding represented by the solid black line, and observed dew point temperature for this sounding represented the dotted black line. Modeled temperature for this sounding represented by the solid red line, and modeled dew point temperature for this sounding represented by the dotted red line.

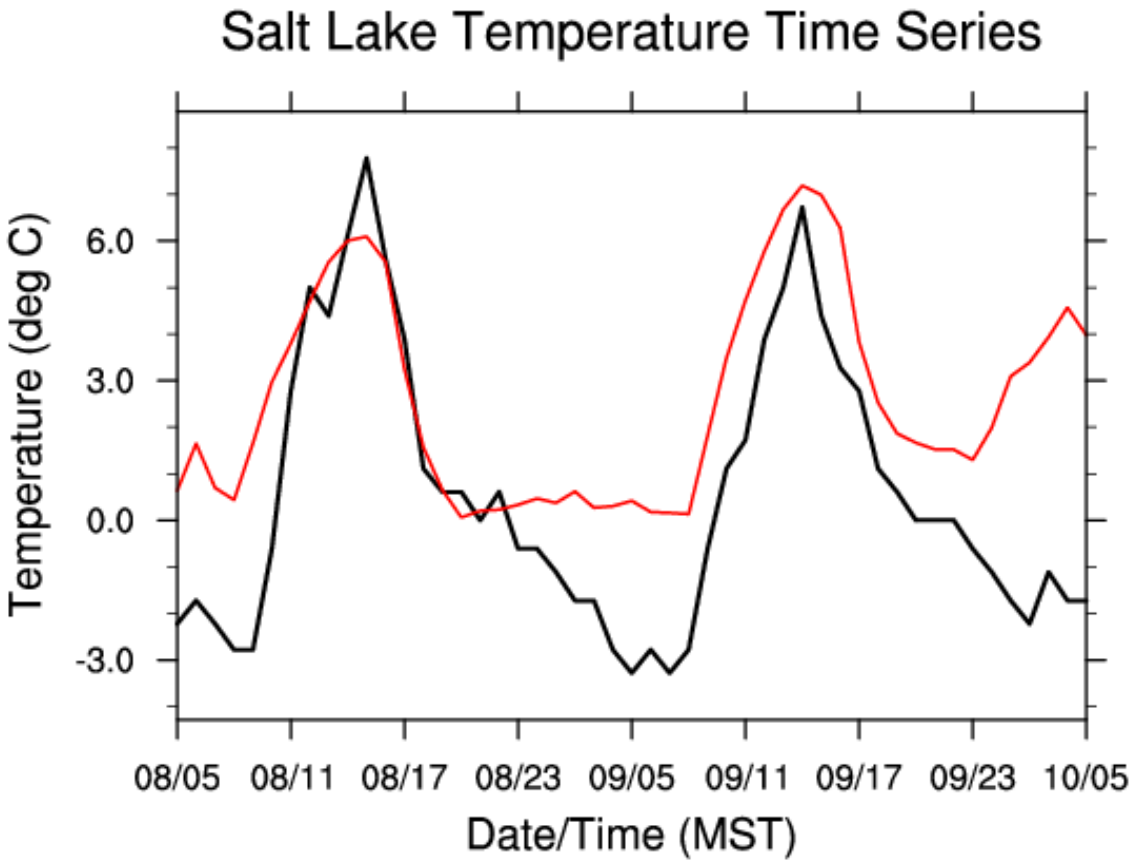


Figure 3.57. Temperature time series comparison for duration of the Goddard shortwave radiation simulation. Observed temperature in black, model solution in red.

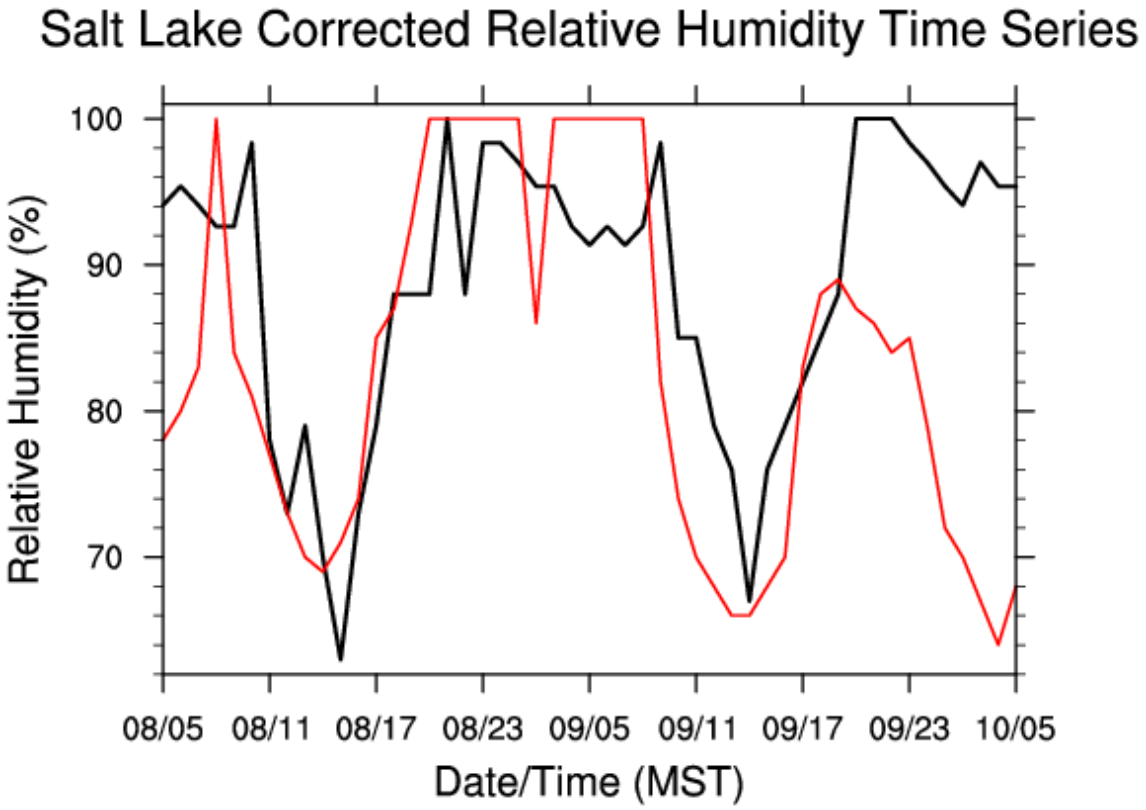


Figure 3.58. Corrected relative humidity time series comparison for duration of Goddard shortwave radiation model simulation. Observed corrected relative humidity in black, model solution in red.

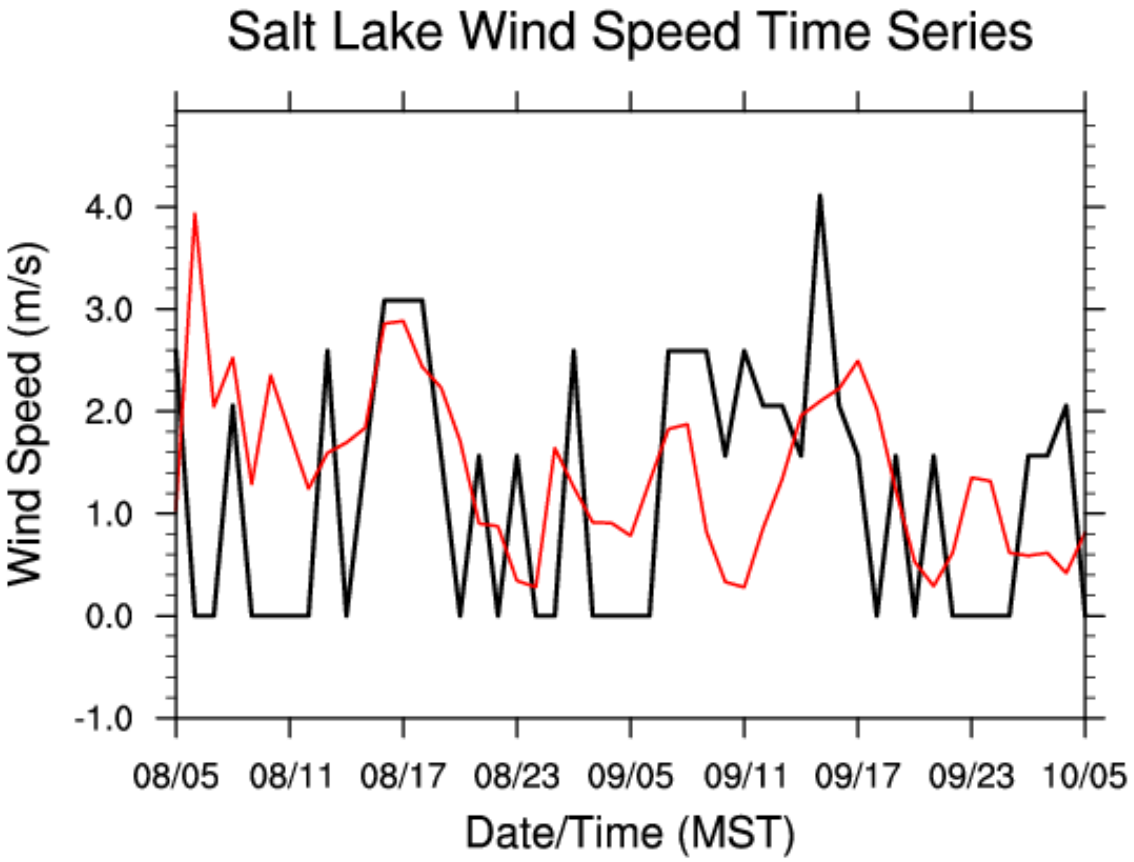


Figure 3.59. Wind speed time series comparison for duration of Goddard shortwave radiation model simulation. Observed corrected relative humidity in black, model solution in red.

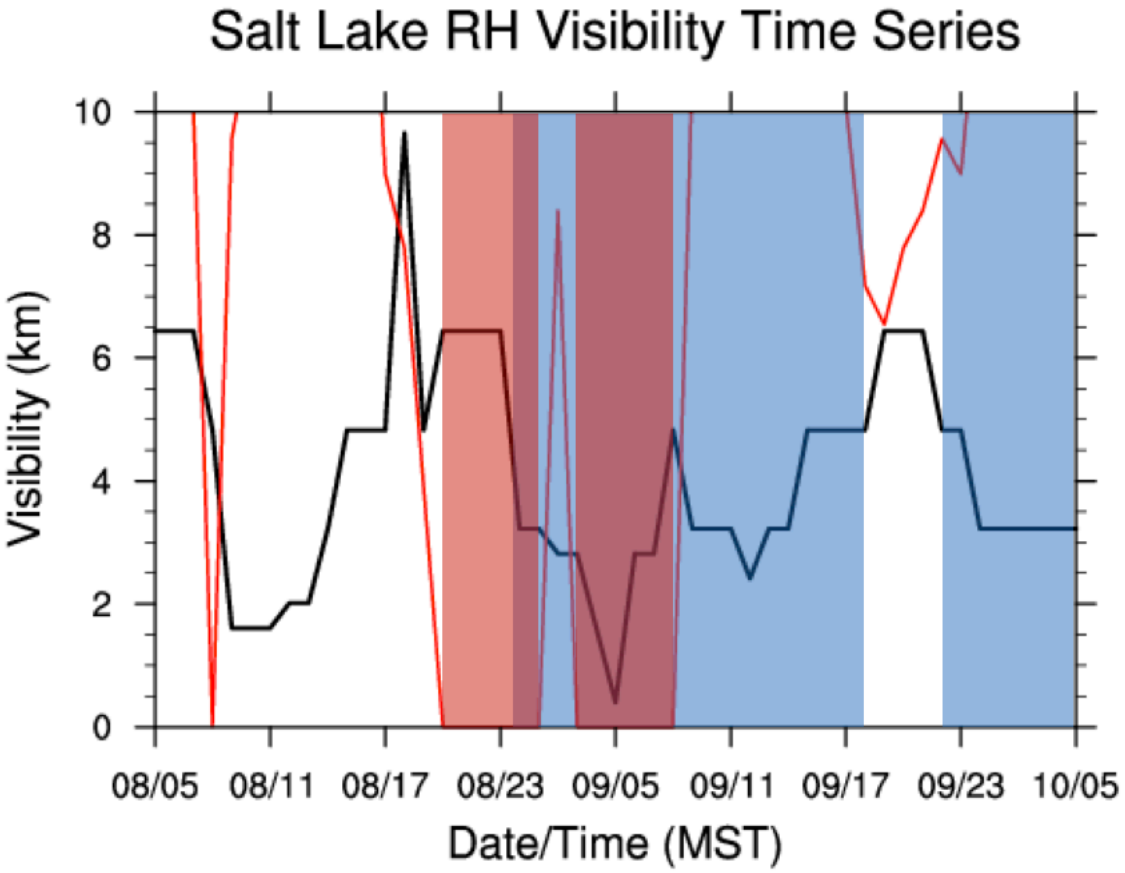


Figure 3.60. Visibility time series comparison calculated with respect to corrected relative humidity for Goddard shortwave radiation simulation. Observed visibility is in black, model solution in red. Blue shading represents observed fog, and red shading represents fog in model solution.

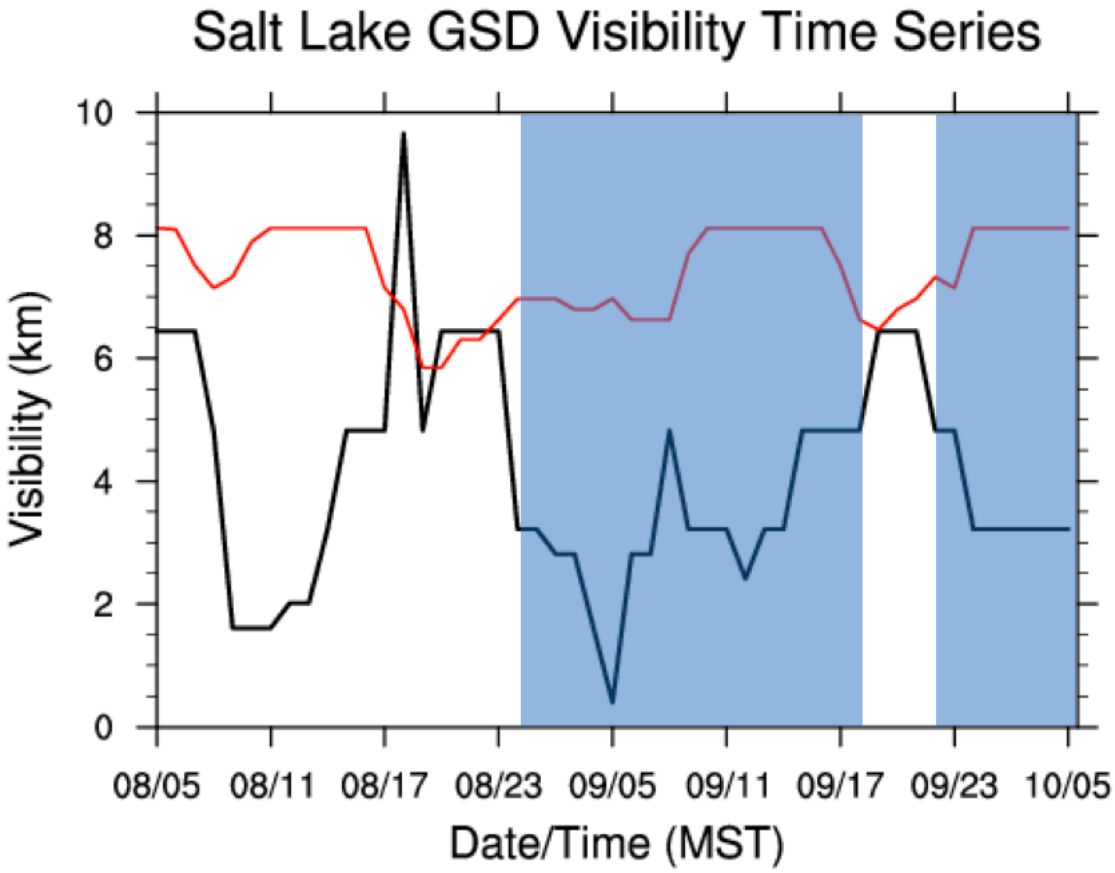


Figure 3.61. Visibility time series comparison calculated with respect to corrected relative humidity for Goddard shortwave radiation simulation. Observed visibility is in black, model solution in red. Blue shading represents observed fog, and red shading represents fog in model solution.

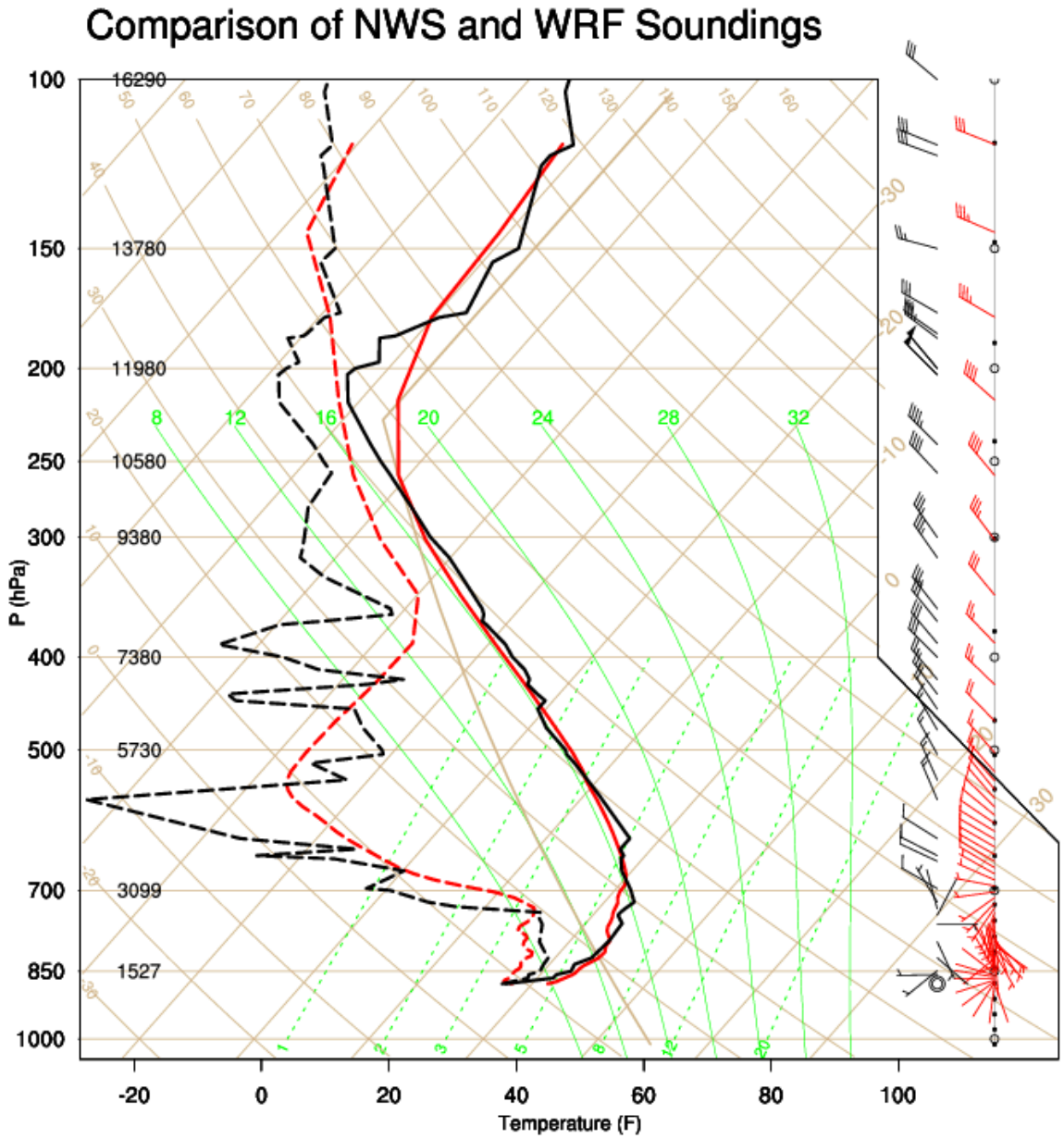


Figure 3.62. Sounding comparison at Salt Lake City International Airport (KSLC) from 1200 UTC 09 January 2015 between observations and sensitivity test run with the Goddard longwave radiation scheme. Temperature (F) along x-axis and pressure (hPa) along y-axis. Temperature (C) (straight beige lines), dry adiabats (curved beige lines), moist adiabats (curved green lines), saturation mixing ratio lines (dotted straight green lines), and wind barbs (speed in knots) analyzed. Observed temperature for this sounding represented by the solid black line, and observed dew point temperature for this sounding represented the dotted black line. Modeled temperature for this sounding represented by the solid red line, and modeled dew point temperature for this sounding represented by the dotted red line.

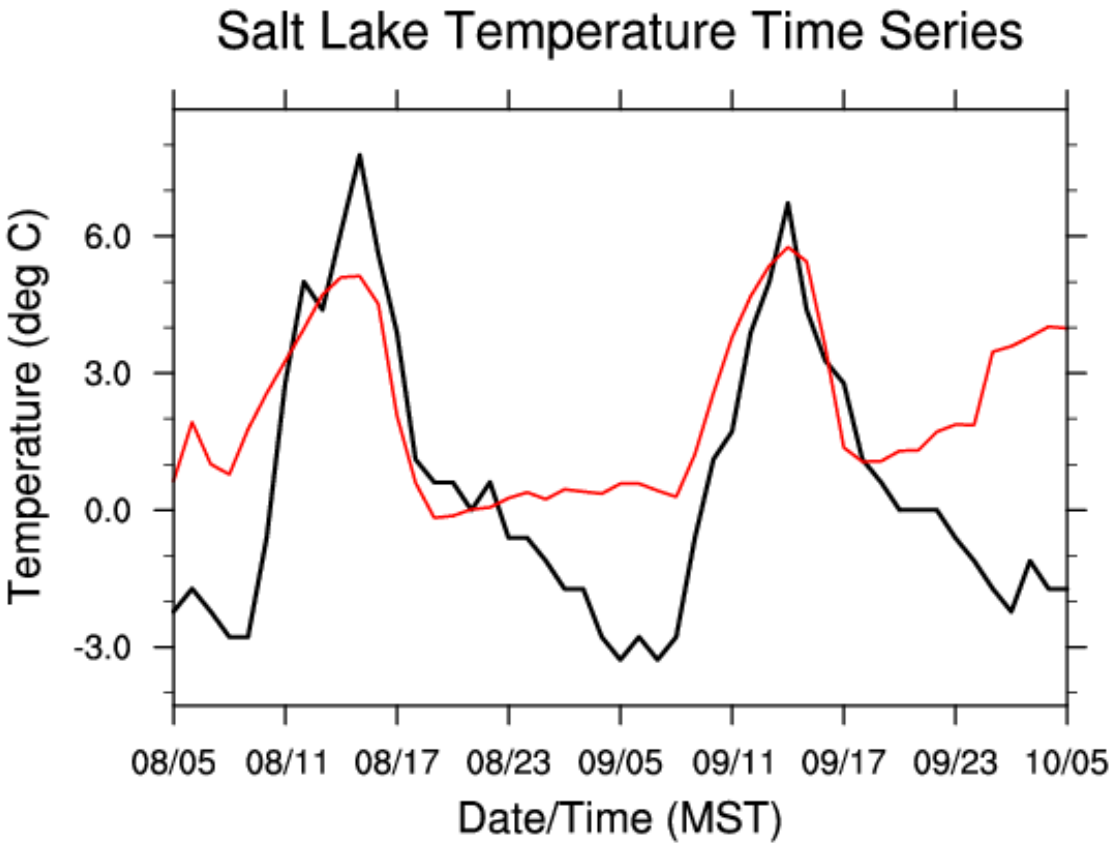


Figure 3.63. Temperature time series comparison for duration of the Goddard longwave radiation simulation. Observed temperature in black, model solution in red.

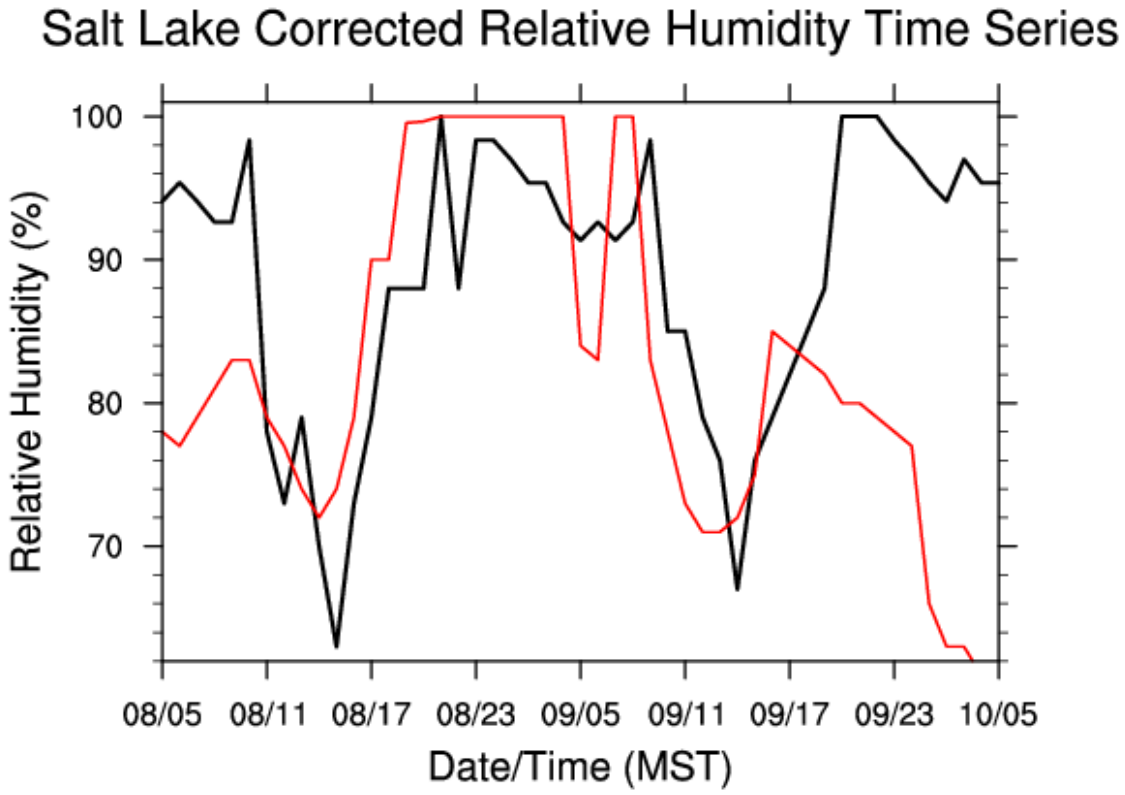


Figure 3.64. Corrected relative humidity time series comparison for duration of Goddard longwave radiation model simulation. Observed corrected relative humidity in black, model solution in red.

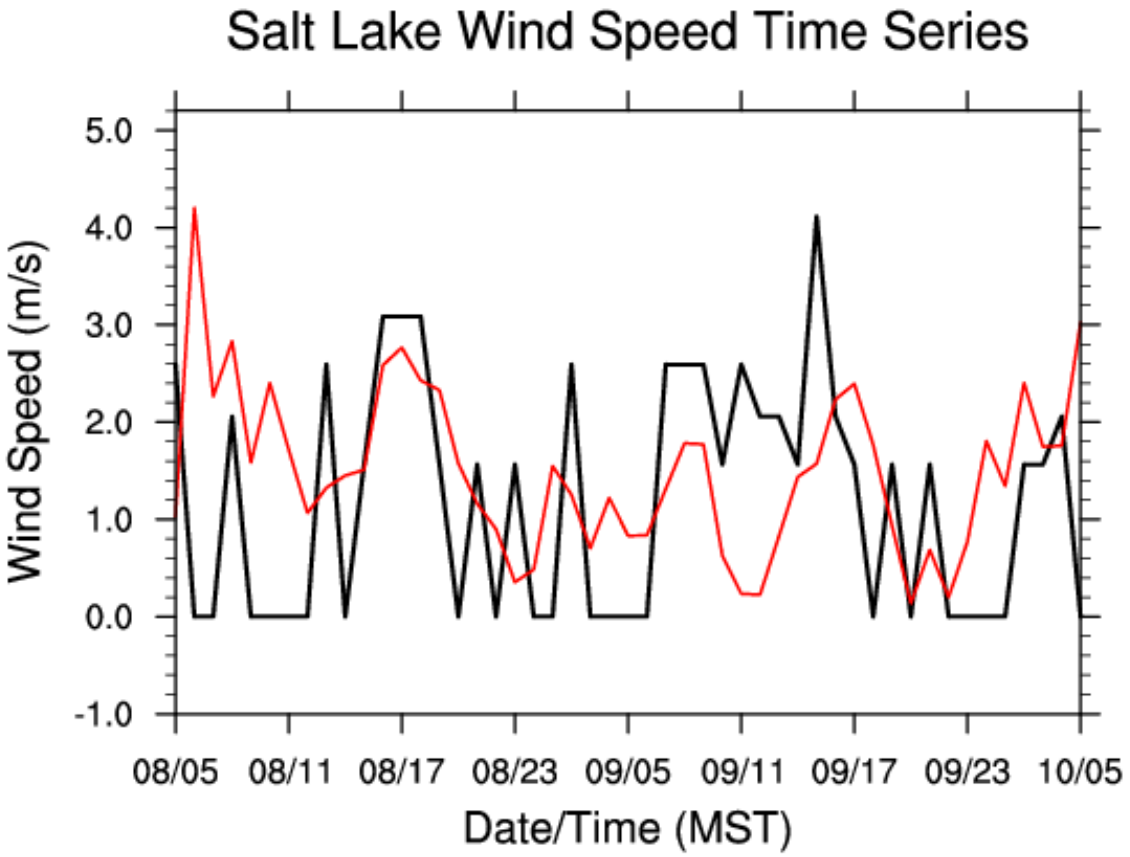


Figure 3.65. Wind speed time series comparison for duration of Goddard longwave radiation model simulation. Observed corrected relative humidity in black, model solution in red.

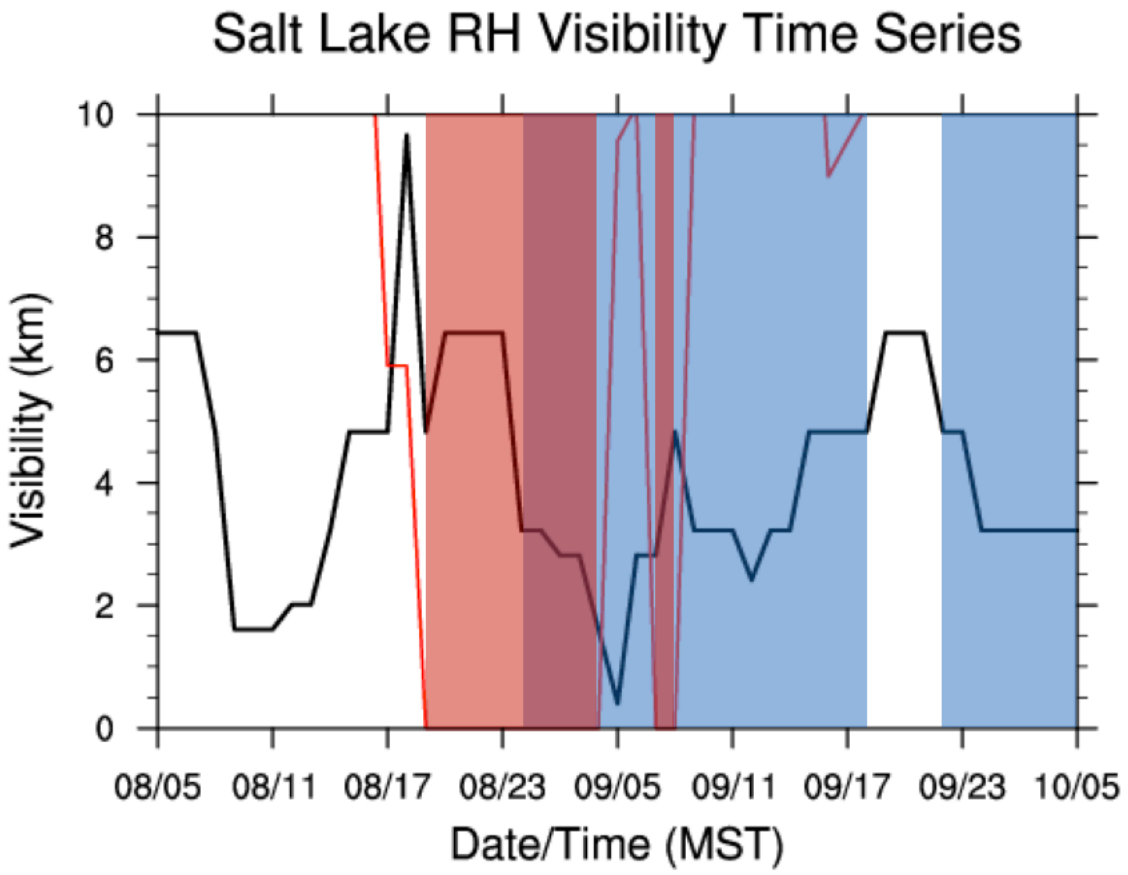


Figure 3.66. Visibility time series comparison calculated with respect to corrected relative humidity for Goddard longwave radiation simulation. Observed visibility is in black, model solution in red. Blue shading represents observed fog, and red shading represents fog in model solution.

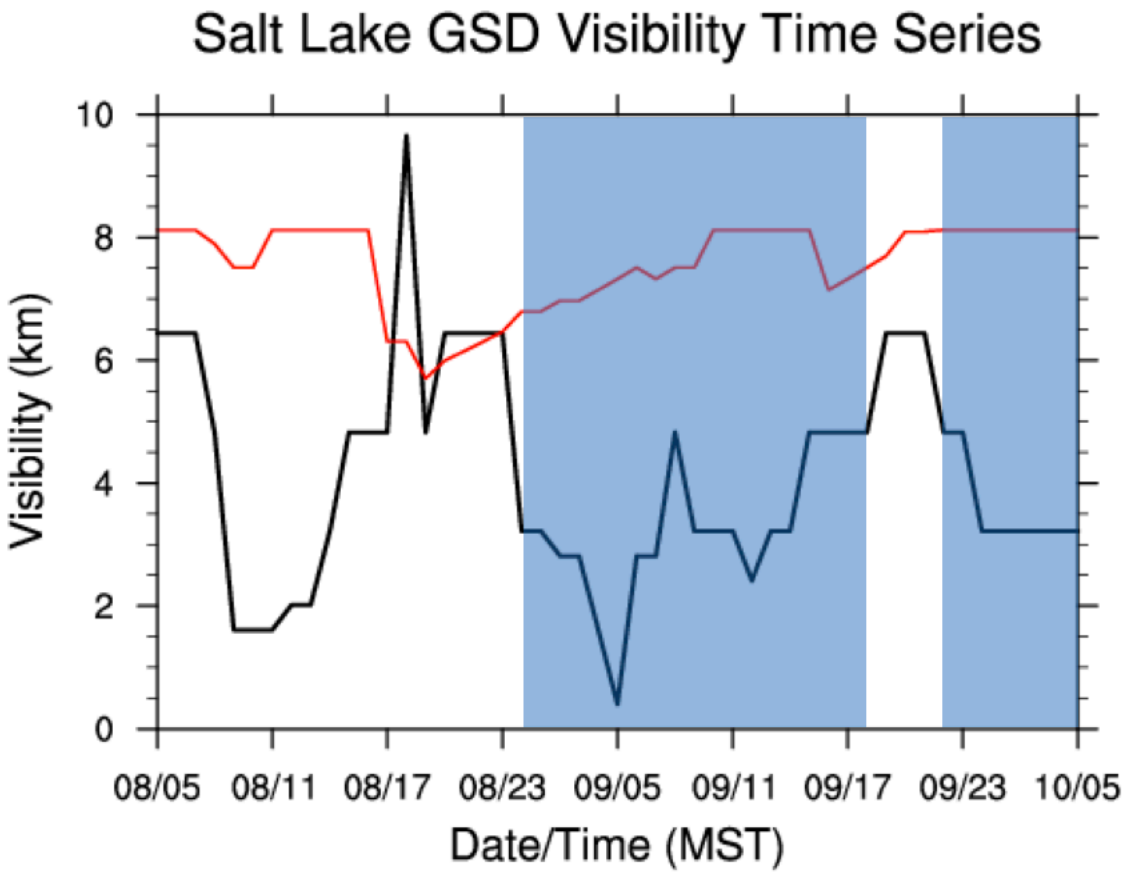


Figure 3.67. Visibility time series comparison calculated with respect to the GSD visibility algorithm for Goddard longwave radiation simulation. Observed visibility is in black, model solution in red. Blue shading represents observed fog, and red shading represents fog in model solution.

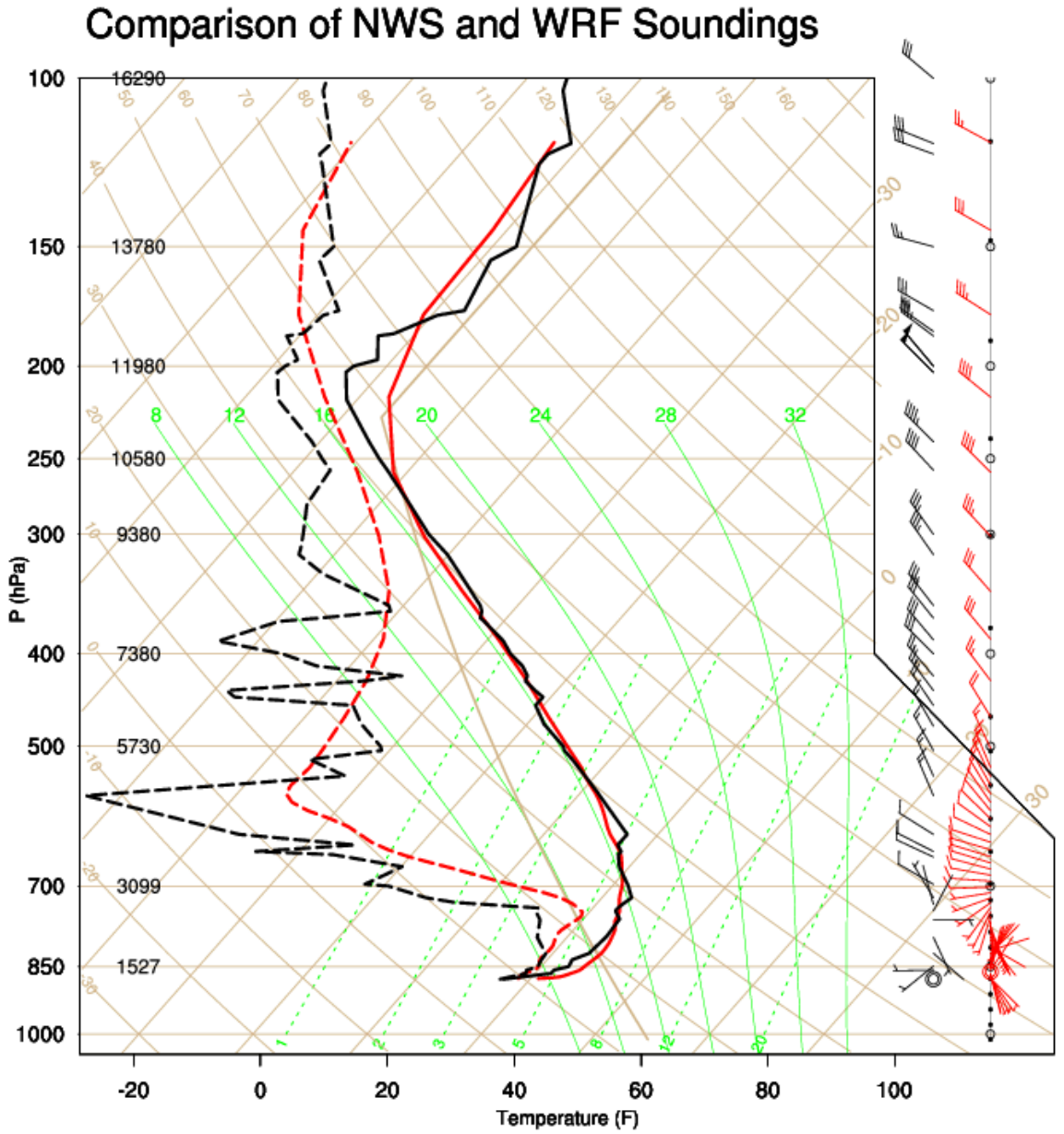


Figure 3.68. Sounding comparison at Salt Lake City International Airport (KSLC) from 1200 UTC 09 January 2015 between observations and sensitivity test run with the control configuration initialized at 0000 UTC 09 January. Temperature (F) along x-axis and pressure (hPa) along y-axis. Temperature (C) (straight beige lines), dry adiabats (curved beige lines), moist adiabats (curved green lines), saturation mixing ratio lines (dotted straight green lines), and wind barbs (speed in knots) analyzed. Observed temperature for this sounding represented by the solid black line, and observed dew point temperature for this sounding represented the dotted black line. Modeled temperature for this sounding represented by the solid red line, and modeled dew point temperature for this sounding represented by the dotted red line.

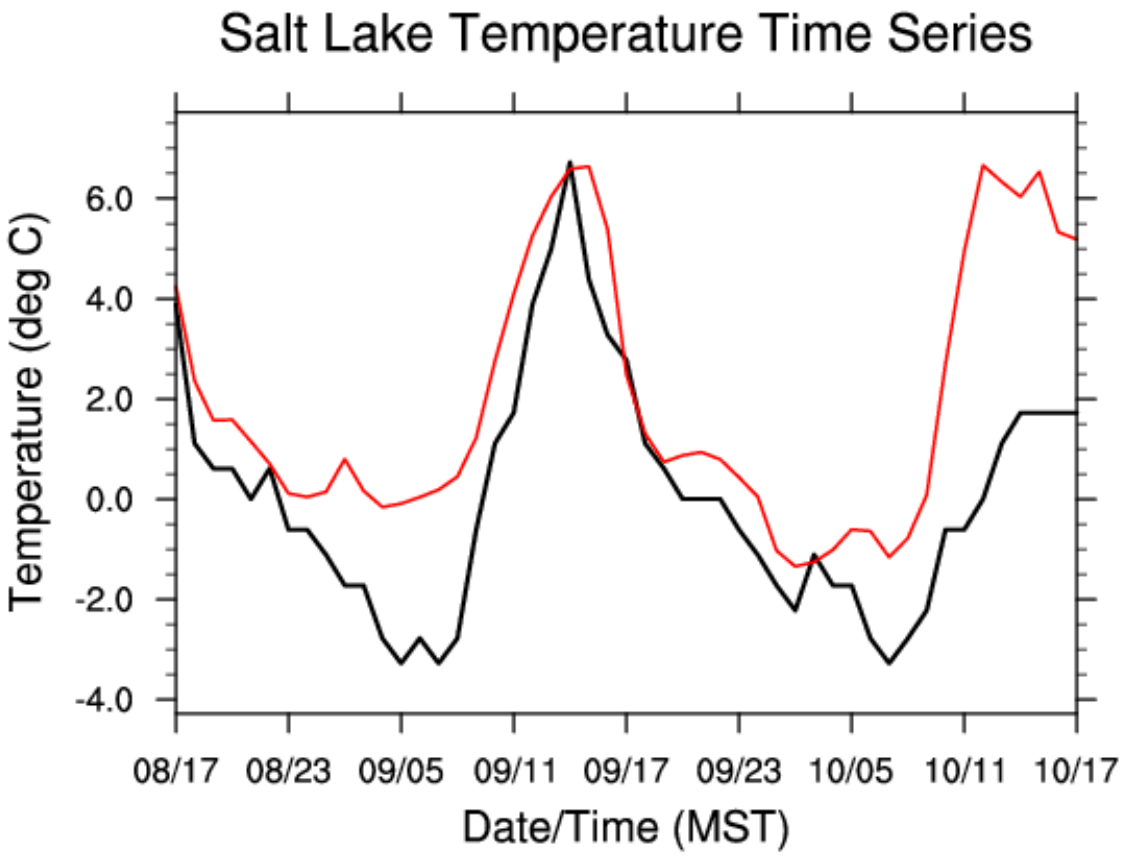


Figure 3.69. Temperature time series comparison for duration of the control simulation initialized at 0000 UTC 09 January. Observed temperature in black, model solution in red.

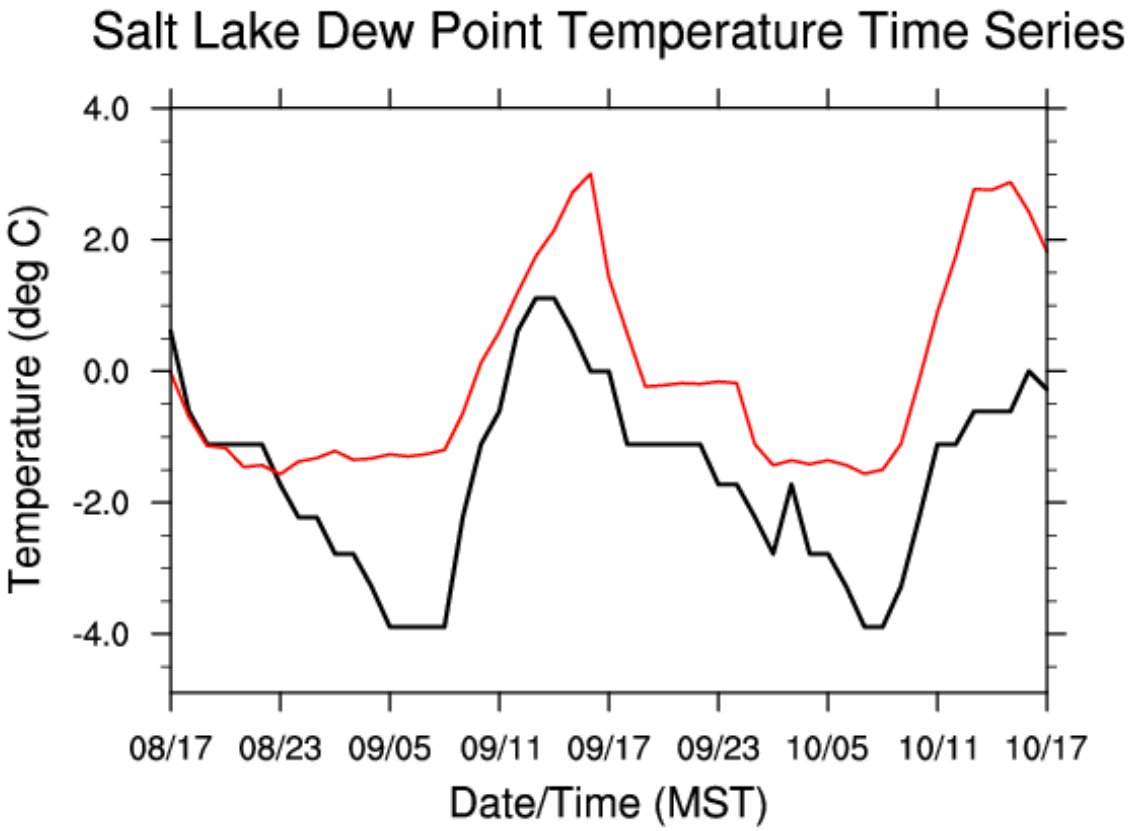


Figure 3.70. Dew point temperature time series comparison for duration of the control simulation initialized at 0000 UTC 09 January. Observed dew point temperature in black, model solution in red.

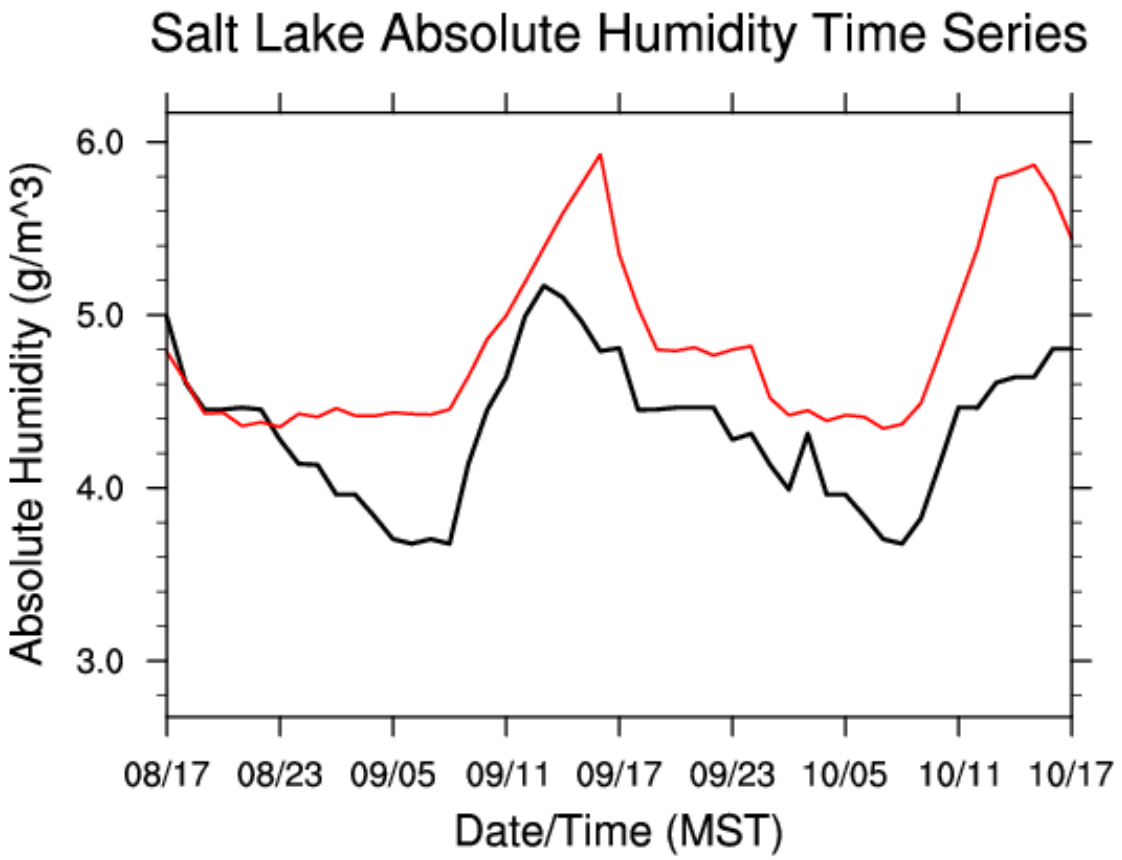


Figure 3.71. Absolute humidity time series comparison for duration of the control simulation initialized at 0000 UTC 09 January. Observed absolute humidity in black, model solution in red.

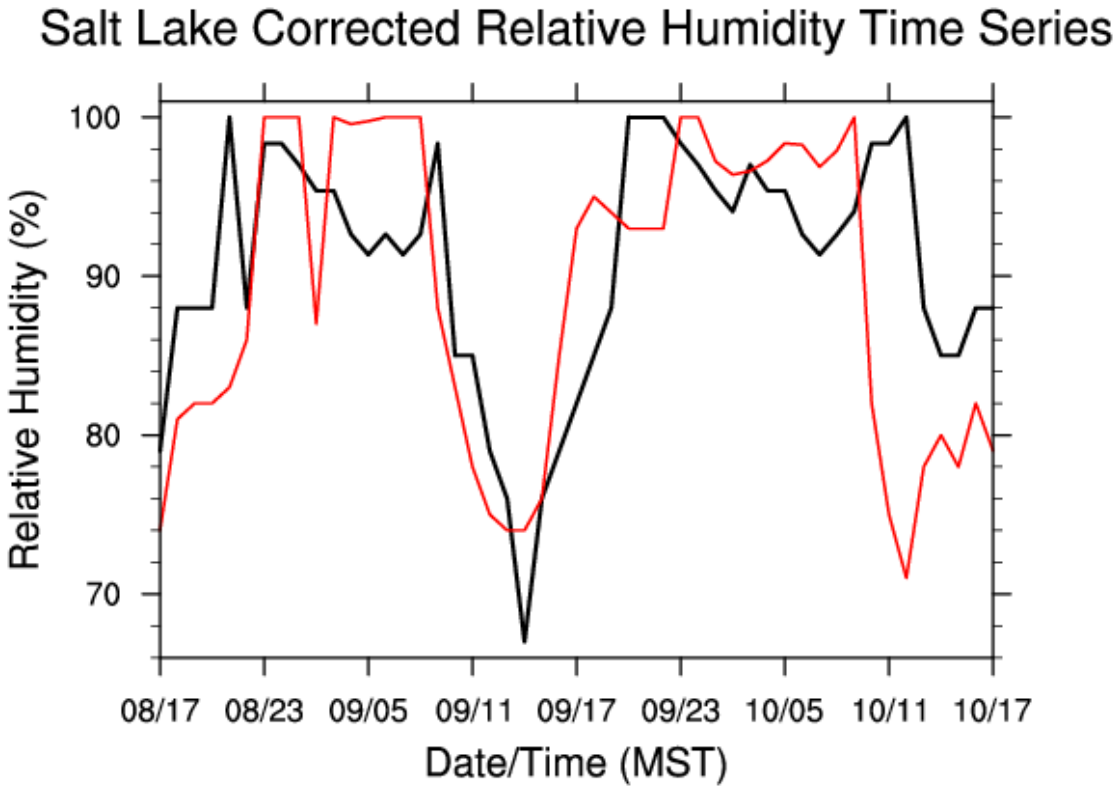


Figure 3.72. Corrected relative humidity time series comparison for duration of the control simulation initialized at 0000 UTC 09 January. Observed corrected relative humidity in black, model solution in red.

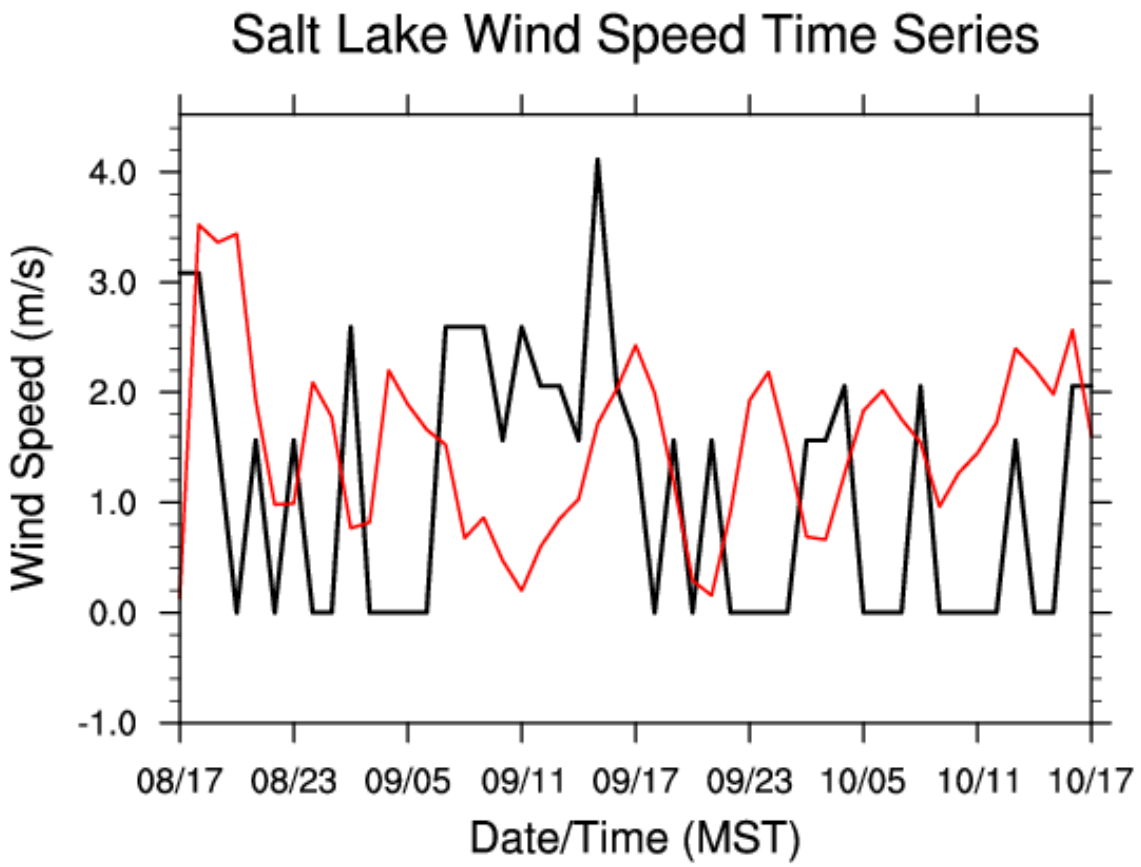


Figure 3.73. Wind speed time series comparison for duration of the control simulation initialized at 0000 UTC 09 January. Observed wind speed in black, model solution in red.

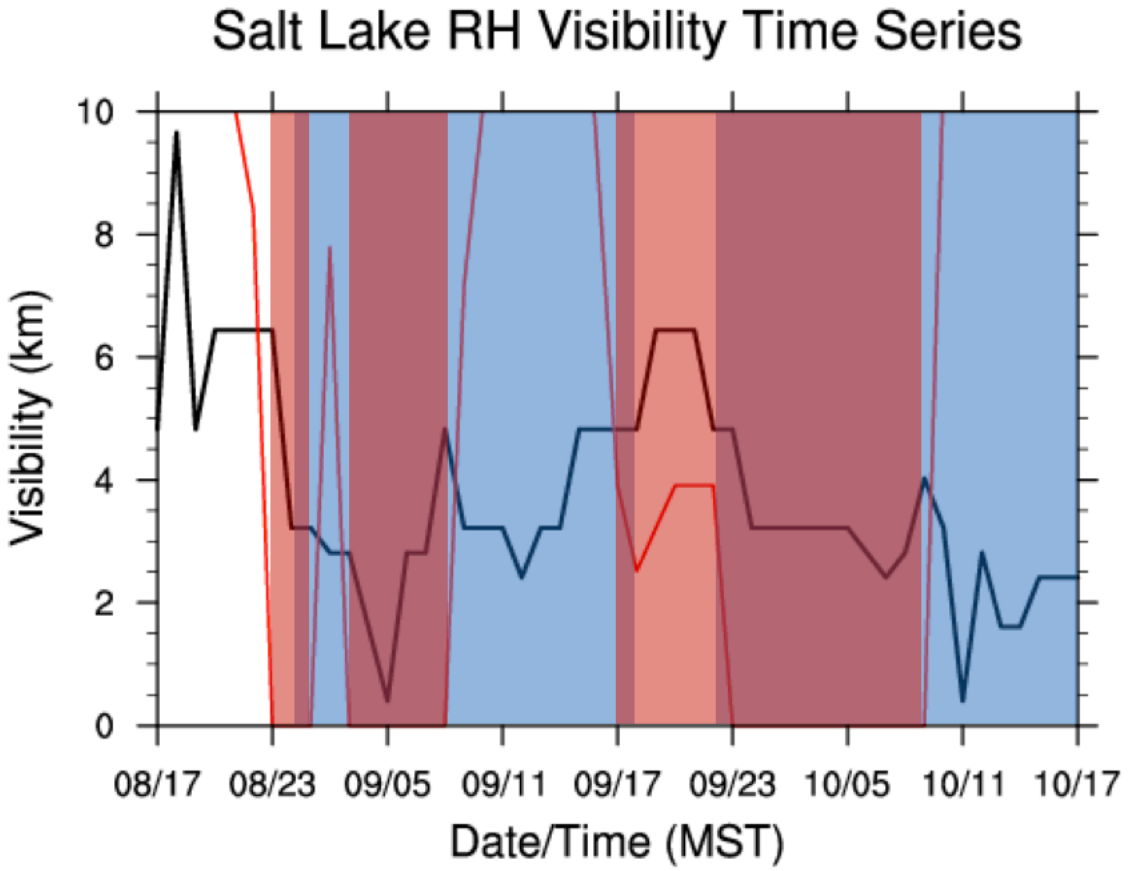


Figure 3.74. Visibility time series comparison calculated with respect to corrected relative humidity for the control simulation initialized at 0000 UTC 09 January. Observed visibility is in black, model solution in red. Blue shading represents observed fog, and red shading represents fog in model solution.

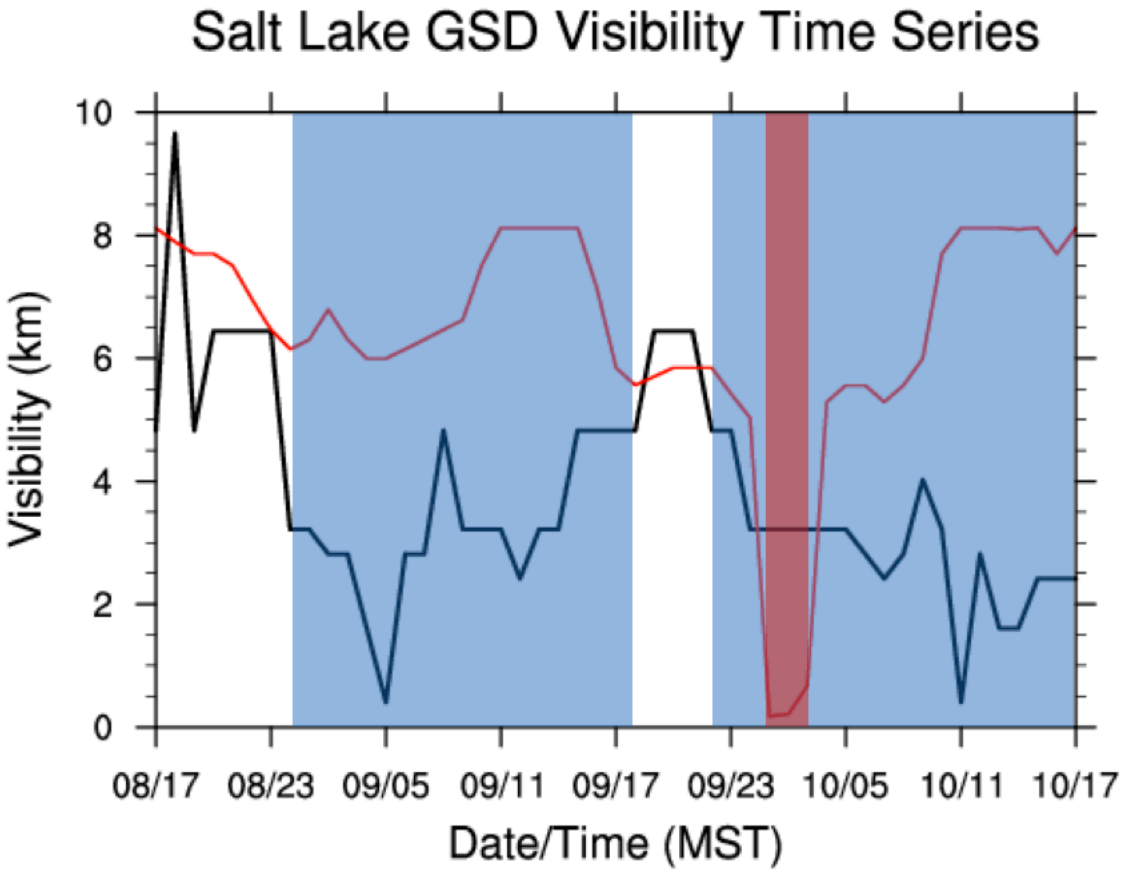


Figure 3.75. Visibility time series comparison calculated with respect to the GSD visibility algorithm for the control simulation initialized at 0000 UTC 09 January. Observed visibility is in black, model solution in red. Blue shading represents observed fog, and red shading represents fog in model solution.

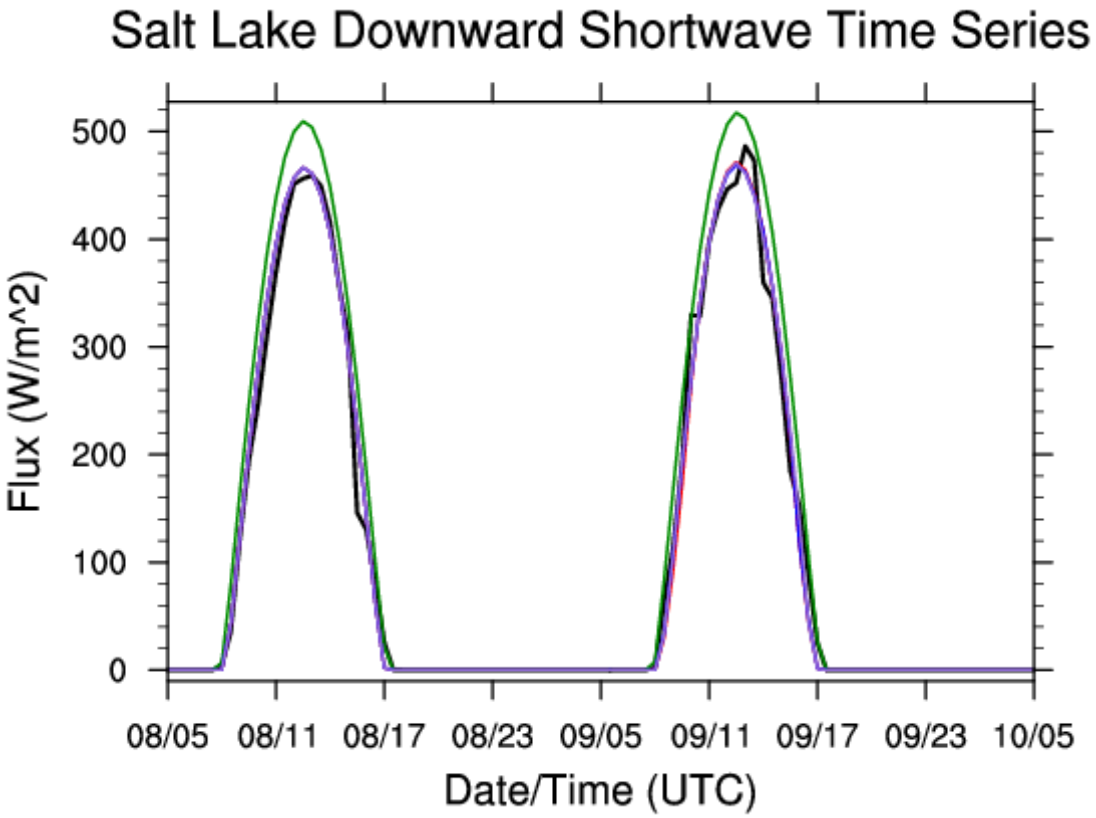


Figure 3.76. Downward shortwave radiation time series comparison between observations (black line) and control (red), Goddard shortwave (green), Goddard longwave (blue), and control with forced initial albedo (purple). In this figure, the values for control, Goddard longwave, and control with forced initial albedo are the same.

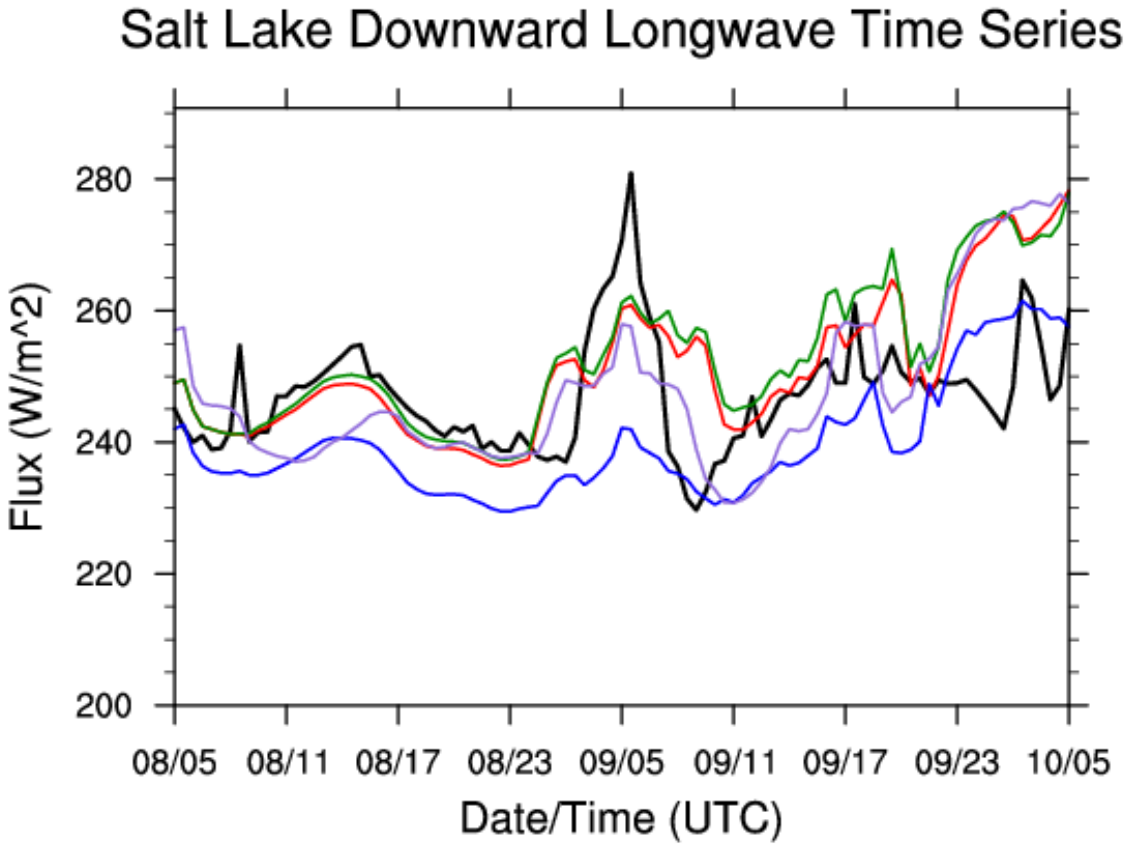


Figure 3.77. Downward longwave radiation time series comparison between observations (black line) and control (red), Goddard shortwave (green), Goddard longwave (blue), and control with forced initial albedo (purple).

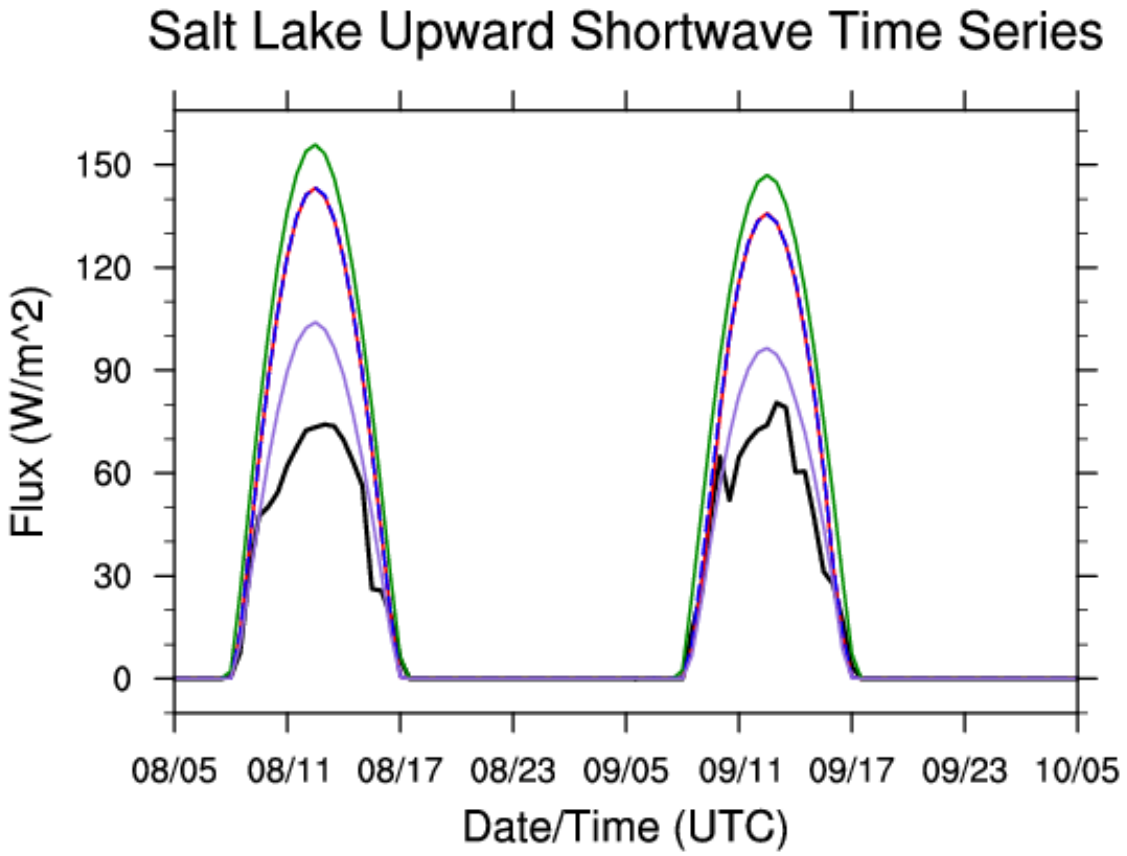


Figure 3.78. Upward shortwave radiation time series comparison between observations (black line) and control (red), Goddard shortwave (green), Goddard longwave (blue), and control with forced initial albedo (purple).

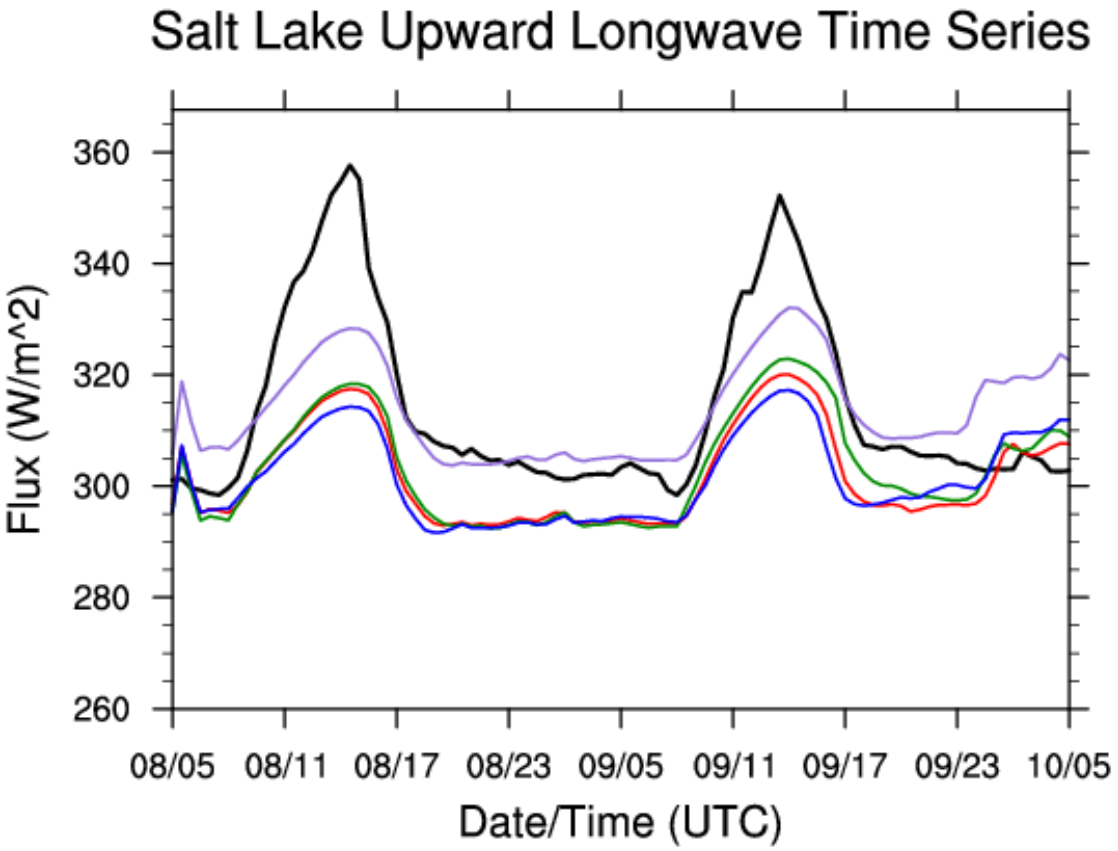


Figure 3.79. Upward longwave radiation time series comparison between observations (black line) and control (red), Goddard shortwave (green), Goddard longwave (blue), and control with forced initial albedo (purple).

Table 3.1. A table detailing the configuration of each of the experiments conducted in this study.

| Experiment | Microphysics | Climatology | PBL | Cumulus | Land Surface | LW Radiation | SW Radiation | Initialization Time |
|---|---|---|---|---|---|---|---|---|
| Control | Thompson | -- | YSU | KF | Noah | RRTM | Dudhia | 0500 MST 8 January |
| Experiment 1 | Thompson AA | True | YSU | KF | Noah | RRTM | Dudhia | 0500 MST 8 January |
| Experiment 2 | Thompson AA | False | YSU | KF | Noah | RRTM | Dudhia | 0500 MST 8 January |
| Experiment 3 | Lin | -- | YSU | KF | Noah | RRTM | Dudhia | 0500 MST 8 January |
| Experiment 4 | Morrison | -- | YSU | KF | Noah | RRTM | Dudhia | 0500 MST 8 January |
| Experiment 5 | Thompson | -- | MYJ | KF | Noah | RRTM | Dudhia | 0500 MST 8 January |
| Experiment 6 | Thompson | -- | YSU | KF | Thermal Diffusion | RRTM | Dudhia | 0500 MST 8 January |
| Experiment 7 | Thompson | -- | YSU | KF | Noah | RRTM | Goddard | 0500 MST 8 January |
| Experiment 8 | Thompson | -- | YSU | KF | Noah | RRTM | RRTMG | 0500 MST 8 January |
| Experiment 9 | Thompson | -- | YSU | KF | Noah | Goddard | Dudhia | 0500 MST 8 January |
| Experiment 10 | Thompson | -- | YSU | KF | Noah | GFDL | Dudhia | 0500 MST 8 January |
| Experiment 11 | Thompson | -- | YSU | KF | Noah | RRTM | Dudhia | 1700 MST 8 January |

# CHAPTER 4

## SUMMARY AND CONCLUDING REMARKS

In this study, a two-fold experiment was performed. First, data from eighteen winters were compiled and analyzed to make the first study of the connection between cold air pools and fog occurrences in a mountain valley. Salt Lake City was chosen as a test site because extensive cold pool and fog studies have been performed in this location (Hill 1988; Laureau et al. 2013; Hodges and Pu 2015). It is found that cold pools are important in the formation of fog events in the Salt Lake valley, as neither is statistically independent from another.

In the second portion of the study, the predictability of an inversion fog event was studied using the WRF model. The results were evaluated against observations taken during MATERHORN-Fog IOP 2, a unique opportunity to have access to extensive fog observation data. This study has formed the following main conclusions:

- The synoptic setup in which fog forms can be accurately captured by numerical simulation.
- Accurate specification of surface and boundary layer variables are vital in correctly predicting fog in a numerical model.
- Fog forecasts are sensitive to planetary boundary layer, radiation, cloud microphysical, and land surface schemes.

- Accurate fog prediction is also sensitive to forecast lead time.

Future works should be conducted for more case studies with comprehensive examination of the role of land surface, boundary layer, cloud microphysical, and radiation processes in fog formation and evolution. The evaluation of the land surface representation such as albedo and surface emissivity should be conducted. Finally, data assimilation at the surface should be investigated as an option to better represent current surface conditions.

REFERENCES


American Meteorological Society, 2012: Glossary of Meteorology. Accessed 1 April 2016. [Available online at http://glossary.ametsoc.org]

Ballard, S., B. Golding, and R. Smith, 1991: Mesoscale model experimental forecasts of the Haar of northeast Scotland. *Mon. Wea. Rev.*, **119**, 2107-2123.

Bergot, T., and D. Guédalia, 1994: Numerical forecasting of radiation fog. Part I: Numerical model and sensitivity tests. *Mon. Wea. Rev.*, **122**, 1218-1230.

Bergot, T., E. Terradellas, J. Cuxart, A. Mira, O. Liechti, M. Mueller, and N. W. Nielsen, 2007: Intercomparison of single-column numerical models for the prediction of radiation fog. *J. Appl. Meteor. Climat.*, **46**, 504-521.

Brown, R., and W. T. Roach, 1976: The physics of radiation fog: II – A numerical study. *Quart. J. Roy. Meteor. Soc.*, **102**, 335-354.

Byers, H. R., 1959: *General Meteorology*. McGraw-Hill, 540 pp.

Chachere, C. N., and Z. Pu, 2016: Connections between cold air pools and mountain valley fog events in Salt Lake City. *Pure Appl. Geophys.* doi:10.1007/s00024-016-1316-x

Chen, F., and J. Dudhia, 2001: Coupling an advanced land surface-hydrology model with the Penn State-NCAR MM5 modeling system. Part I: Model implementation and sensitivity. *Mon. Wea. Rev.*, **129**, 569-585.

Colarco, P., A. da Silva, M. Chin, and T. Diehl, 2010: Online simulations of global aerosol distributions in the NASA GEOS-4 model and comparisons to satellite and ground-based aerosol optical depth. *J. Geophys. Res.*, **115**, D14207, doi:10.1029/2009JD012820.

Duynkerke, P. G., 1990: Radiation fog: A comparison of model simulation with detailed observations. *Mon. Wea. Rev.*, **119**, 324-341.

Fernando, H. J. S., E. R. Pardyjak, S. Di Sabatino, F. K. Chow, S. F. J. De Wekker, S. W. Hoch, J. Hacker, J. C. Pace, T. Pratt, Z. Pu, W. J. Steenburgh, C. D. Whiteman, Y. Wang, D. Zajic, B. Balsley, R. Dimitrova, G. D. Emmitt, C. W. Higgins, J. C. R. Hunt, J. C. Knievel, D. Lawrence, Y. Liu, D. F. Nadeau, E. Kit, B. W. Blomquist, P. Conroy, R. S. Coppersmith, E. Creegan, M. Felton, A. Grachev, N. Gunawardena, C. Hang, C. M. Hocut, G. Huynh, M. E. Jeglum, D. Jensen, V. Kulandaivelu, M. Lehner, L. S. Leo, D. Liberzon, J. D. Massey, K. McEnerney, S. Pal, T. Price, M. Sghiatti, Z. Silver, M. Thompson, H. Zhang, and T. Zsedrovits, 2015: The MATERHORN – Unraveling the intricacies of mountain weather. *Bull. Amer. Meteor. Soc.*, **96**, 1945-1967.

Gultepe, I., and J. Milbrandt, 2007: Microphysical observations and mesoscale model simulation of a warm fog case during FRAM project. *Pure Appl. Geophys.*, **164**, 1161-1178.

Gultepe, I., and Coauthors, 2007: Fog research: A review of past achievements and future perspectives. *Pure Appl. Geophys.*, **164**, 1121-1159.

Gultepe, I., and J. Milbrandt, 2009: Probabilistic parameterizations of visibility using observations of rain precipitation rate, relative humidity, and visibility. *J. Appl. Meteor. Climat.*, **49**, 36-46.

Gultepe, I., T. Kuhm, M. Pavolonis, C. Calvert, J. Gurka, A. J. Heymsield, P. S. K. Liu, B. Zhou, R. Ware, B. Ferrier, J. Milbrandt, and B. Bernstein, 2014: Ice fog in arctic during FRAM-Ice fog project: Aviation and nowcasting applications. *Bull. Amer. Meteor. Soc.*, **95**, 211-226.

Gultepe, I., H. J. S. Fernando, E. Pardyjak, S. Hoch, Z. Silver, E. Creegan, L. Leo, Z. Pu, S. De Wekker, and C. Hang, 2016: Mountain ice fog: Observations and predictability. *Pure Appl. Geophys.*, under review.

Hill, G. E., 1988: Fog effect of the Great Salt Lake. *J. Appl. Meteor.*, **27**, 778-783.

Hodges, D. G., and Z. Pu, 2015: The climatology, frequency, and distribution of cold season fog events in northern Utah. *Pure Appl. Geophys.*, in press.

Holets, S., and R. N. Swanson: High-inversion fog episodes in central California. *J. Appl. Meteor.*, **20**, 890-899.

Holmes, H. A., J. K. Sriramasamudram, E. R. Pardyjak, and C. D. Whiteman, 2015: Turbulent fluxes and pollutant mixing during wintertime air pollution episodes in complex terrain. *Environ. Sci. Technol.*, **49**, 13206-13214.

Horel, J., and coauthors, 2002: MesoWest: Cooperative mesonets in the western United States. *Bull. Amer. Meteor. Soc.*, **83**, 211-225.

Kalverla, P. C., G. Duine, G. Steeneveld, and T. Hedde, 2016: Evaluation of the weather research and forecasting model in the Durance Valley complex terrain during the KASCADE field campaign. *J. Appl. Meteor. Climat.*, **55** (3), 495-519.

Kunkel, B. A., 1984: Parameterization of droplet terminal velocity and extinction coefficient in fog models. *J. Appl. Meteor.*, **23**, 34-41.

Lareau, N. P., E. Crosman, C. D. Whiteman, J. D. Horel, S. W. Hoch, W. O. J. Brown, and T. W. Horst, 2013: The persistent cold-air pool study. *Bull. Amer. Meteor. Soc.*, **94**, 51-63.

Liu, Y. and coauthors, 2008a: The operational mesogamma-scale analysis and forecast system of the U.S. Army test and evaluation command. Part I: Overview of the modeling system, the forecast products, and how the products are used. *J. Appl. Meteor. Climat.*, **47**, 1077-1092.

Liu, Y. and coauthors, 2008b: The operational mesogamma-scale analysis and forecast system of the U.S. Army test and evaluation command. Part II: Interrange comparison of model analyses and forecasts. *J. Appl. Meteor. Climat.*, **47**, 1093-1104.

Machalek, A., 1974: Inversionsuntersuchungen in einem Gebirgstal. *Wetter Leben*, **26**, 157-168.

Massey, J. D., W. J. Steenburgh, S. W. Hoch, and J. C. Knievel, 2014: Sensitivity of near-surface temperature forecasts to soil properties over a sparsely vegetated dryland region. *J. Appl. Meteor. Clim.*, **53**, 1976-1995.

Nakaniski, M., and H. Niino, 2006: An improved Mellow-Yamada level-3 model: Its numerical stability and application to a regional prediction of advection fog. *Bound.-Layer Meteor.*, **119** (2), 397-407.

Neemann, E. M., E. T. Crosman, J. D. Horel, and L. Avey, 2015: Simulations of a cold-air pool associated with elevated wintertime ozone in the Uintah Basin, Utah. *Atmos. Chem. Phys.*, **15**, 135-151.

Pagowski, M., I. Gultepe, and P. King, 2004: Analysis and modeling of an extremely dense fog event in southern Ontario. *J. Appl. Meteor.*, **43**, 3-16.

Price, J. D., S. Vosper, A. Brown, A. Ross, P. Clark, F. Davies, V. Horlacher, B. Claxton, J. R. McGregor, J. S. Hoare, B. Jemmett-Smith, and P. Sheridan, 2011: COLPEX. Field and numerical studies over a region of small hills. *Bull. Amer. Meteor. Soc.*, **92**, 1636-1650.

Pu, Z., C. N. Chachere, S. W. Hoch, E. Pardyjak, and I. Gultepe, 2016: Numerical prediction of cold season fog events over complex terrain: The performance of

the WRF model during MATERHORN-Fog and early evaluation. *Pure and App. Geo.*, submitted.

Roach, W. T., R. Brown, R. Caughey, S. J. Garland, and C. J. Readings, 1976: The physics of radiation fog: I – A field study. *Quart. J. Roy. Meteor. Soc.*, **102**, 361-372.

Skamarock, W. C., J. B. Klemp, J. Dudhia, D. O. Gill, M. Barker, K. G. Duda, X. Huang, Y. Huang, W. Wang, and J. G. Powers, 2008: A description of the advanced research WRF Version 3. NCAR Tech. Note, NCAR/TN-475+STR, 113 pp.

Steeneveld, G. J., R. J. Ronda, and A. A. M. Holtslag, 2014: The challenge of forecasting the onset and development of radiation fog using mesoscale atmospheric models. *Bound.-Layer Meteor.*, **154** (2), 265-289.

Stoelinga, M. T., and T. T. Warner, 1999: Nonhydrostatic, mesobeta-scale model simulations of cloud ceiling and visibility for an east coast winter precipitation event. *J. Appl. Meteor.*, **38**, 385-404.

Tardif, R., 2007: The impact of vertical resolution in the explicit numerical forecasting of radiation fog: A case study. *Pure and Appl. Geo.*, **164**, 1221-1240.

Taylor, G. F., 1941: *Aeronautical Meteorology*. Pitman, 455 pp.

Turton, J. D., and R. Brown, 1987: A comparison of a numerical model of radiation fog at night using channels 3 and 4 on the Advanced Very High Resolution Radiometer (AVHRR). *Meteor. Mag.*, **115**, 285-290.

University of Wyoming, 2015: Atmospheric Soundings. Accessed 30 November 2015. [Available online at http://weather.uwyo.edu/upperair/sounding]

Welch, R. M., and B. A. Wielicki, 1986: The stratocumulus nature of fog. *J. Appl. Meteor.*, **12**, 771-780.

Whiteman, C. D., 1982: Breakup of temperature inversions in deep mountain valleys: Part I. Observations. *J. Appl. Meteor.*, **21**, 270-289.

Whiteman, C. D., X. Bian, and S. Zhong, 1999: Wintertime evolution of the temperature inversion in the Colorado plateau basin. *J. Appl. Meteor.*, **38**, 1103-1117.

Whiteman, C. D., S. Zhong, W. J. Shaw, J. M. Hubbe, X. Bian, and J. Mittelstadt, 2001: Cold pools in the Columbia basin. *Wea. Forecasting*, **16**, 432-447.

Whiteman, C. D., and Coauthors, 2008: METCRAX 2006 meteorological experiments in Arizona's meteor crater. *Bull. Amer. Meteor. Soc.*, **89**, 1665-1680.

Whiteman, C. D., S. W. Hoch, J. D. Horel, and A. Charland, 2014: Relationship between particulate air pollution and meteorological variables in Utah's Salt Lake Valley. *Atmos. Env.*, **94**, 742-753.

Wilks, D. S., 2011: *Statistical Methods in the Atmospheric Sciences*. Oxford, 704 pp.

Wolyn, P. G., and T. B. McKee, 1989: Deep stable layers in the intermountain western United States. *Mon. Wea. Rev.*, **117**, 461-472.

Zängl, G., 2005a: Formation of extreme cold-air pools in elevated sinkholes: an idealized numerical process study. *Mon. Wea. Rev.*, **113**, 925-941.

Zängl, G, 2005b: Wintertime cold-air pools in the Bavarian Danube Valley Basin: Data analysis and idealized numerical simulations. *J. Appl. Meteor.*, **44**, 1950-1971.

Zdunkowski, W. and B. Nielsen, 1969: A preliminary prediction analysis of radiation fog. *Pure Appl. Geophys.*, **19**, 45-66.

Zdunkowski, W. and A. Barr, 1972: A radiative-conductive model for the prediction of radiation fog. *Bound.-Layer Meteor.*, **3**, 152-157.

Zhang, H., Z. Pu, and X. Zhang, 2013: Examination of errors in near-surface temperature and wind form WRF numerical simulations in regions of complex terrain. *Wea. Forecasting*, **28**, 893-914.

Zhou, B., J. Du, I. Gultepe, and G. Dimego, 2012: Forecast of low visibility and fog from NCEP: Current status and efforts. *Pure Appl. Geophys.*, **169**, 895-909.